The Dissertation Committee for Jingfei Ma
certifies that this is the approved version of the following dissertation:

The macro- and micro-instabilities in the pedestal region of the Tokamak

Committee:

Philip Morrison, Supervisor

C. Wendell Horton, Co-Supervisor

Herbert Berk

Richard Fitzpatrick

Gary Hallock

The macro- and micro-instabilities in the pedestal region of the Tokamak

by

Jingfei Ma, B.S.

DISSERTATION

Presented to the Faculty of the Graduate School of
The University of Texas at Austin
in Partial Fulfillment
of the Requirements
for the Degree of

DOCTOR OF PHILOSOPHY

THE UNIVERSITY OF TEXAS AT AUSTIN

May 2015

Dedicated to my lovely wife Xiaoyi.

Acknowledgments

I wish to thank Prof. Wendell Horton for his guidance on my research and his patient instructions on the fundamental plasma physics theory through group meetings and personal discussions. I wish to thank Prof. Philip Morrison for all his interesting and inspiring courses on mathematics and physics, and being my official academic advisor. I also wish to thank Dr. Xueqiao Xu and other BOUT++ group members for mentoring me on my simulation work.

Scientists and students at IFS have helped me a lot. I wish to thank Prof. Herbert Berk, Prof. Richard Fitzpatrick and Prof. Gary Hallock for being my committee members and spending time reviewing my dissertation. I wish to thank Dr. François Waelbroeck and Dr. David Hatch for all the discussions on my research. I particularly want to thank Xiangrong Fu, Dimitry Meyerson, Ehab Hassan and Cynthia Correa for helpful discussion and group study.

I wish to thank my parents for always being supportive and guiding me through the hardship of life. I am deeply grateful to my wife Xiaoyi for taking care of me and bringing so much sunshine to my life. I am really thankful to all my friends in Austin, who together make the past five years not only fruitful, but also colorful.

The macro- and micro-instabilities in the pedestal region of the Tokamak

Publication No. ____________________

Jingfei Ma, Ph.D.
The University of Texas at Austin, 2015

Supervisors: Philip Morrison
C. Wendell Horton

In this paper, we present the theoretical and numerical studies of the linear characteristics and nonlinear transport features of the instabilities driven by the steep profile gradient and edge current in the pedestal region of the tokamak. Two important instabilities, the peeling-ballooning (P-B) modes (macro-instability) and the drift-Alfven modes (micro-instability), are studied using the fluid analysis and the BOUT++ codes. In particular, the edge-localized modes (ELMs), which appear to be the energy burst in the nonlinear stage of the peeling-ballooning mode, are numerically studied and the results are compared with the experimental measurement. In addition, the features of the impurity transport in the edge region of the tokamak are theoretically analyzed.

Firstly, we explore the fundamental characteristics of the P-B modes and the ELM bursts numerically using the three-field reduced MHD model

under the BOUT++ framework, in the shifted-circular geometry, i.e. the limiter tokamak geometry. In the linear simulations, the growth rate and real frequency and the mode structure versus the toroidal mode number (n) are shown. The features of the ELM bursts are shown in the nonlinear simulations, including the time evolution of the relative energy loss (ELM size) and the pedestal profile.

Secondly, two original research projects related to the P-B modes and the ELM burst are described. One is the study of the scaling law between the relative energy loss of ELMs and the edge collisionality. We generate a sequence of shifted-circular equilibria with different edge collisionality varying over four orders of magnitude using EFIT. The simulation results are in good agreement with the multi-tokamak experimental data. Another is the study of the differences of the linear behaviors of the P-B modes between the standard and snowflake divertor configurations. Using DIII-D H-mode ElMing equilibria, we found that the differences are due to the local magnetic shear change at the outboard midplane, which is the result of the realization of the snowflake configuration.

Finally, the micro-instability, the drift-Alfven instability in the pedestal region of the DIII-D tokamak is studied. A modified six-field Landau fluid model under BOUT++ framework is used to study the linear characteristics and transport features of the drift-Alfven modes. Based on the DIII-D H-mode discharge, a sequence of divertor tokamak equilibria with different pedestal height is generated by the 'VARYPED' tool for our studies. Quali-

tative agreement is obtained between theoretical analysis and the simulation results in the linear regime. Moreover, the heat transport induced by the drift-Alfven turbulence is explored and the convection level is estimated for both ions and electrons.

Table of Contents

List of Tables

List of Figures

Chapter 1

Introduction

1.1 The peeling-ballooning modes and the Edge-localized modes

The high performance mode ('H-mode') with edge pressure pedestal in tokamak is currently considered the most promising scenario to achieve magnetic confinement fusion[74, 38]. While turbulent transport models of the core confinement can be very sensitive to the height (P_{ped}) and width (L_{ped}) of the edge pedestal[39], these two parameters have been found to be limited by specific edge instabilities: Theories have shown that the height and width of the pedestal are limited by peeling-ballooning (P-B) and kinetic ballooning mode (KBM) respectively[64, 62]. Moreover, the coupled Peeling-Ballooning (P-B) mode is commonly believed to trigger repetitive edge magnetohydrodynamics instability known as 'Edge Localized Mode (ELM)' in its nonlinear stage[63, 7, 65], which appears to be impulsive heat bursts from the edge region to the scrape-off layer (SOL). ELM bursts cause the loss of a considerable portion of the energy in the edge region, degrading core plasma confinement. Thus, a thorough understanding of P-B modes and ELMs is of particular importance to the performance of future fusion reactors.

Aside from their potential to reduce pedestal height and degrade core confinement as a whole, ELMs also cause direct damage to Plasma Facing Components (PFC) such as divertor plates. The heat load that strikes divertor plates during ELM crash highly exceeds the threshold of PFC, leading to materials erosion and impurities transportation back into the core plasma. Considerable efforts have been devoted to ELMs mitigation and PFC improvements in order to tackle this problem. For example, edge resonant magnetic perturbations (RMPs) has been shown to be capable of suppressing ELMs by introducing chaotic magnetic fields in the edge region[16]. Also, the high-refractory material tungsten has been chosen for divertor materials of ITER instead of the traditional Boron and Carbon[17].

In addition to these solutions, advanced divertor concepts have been proposed in the past decade to reduce heat load by improving magnetic geometry near the null point. These concepts include X-divertor[40], which spreads flux by adding a second null point on divertor plate, super X-divertor[72], which enhances X-divertor by expanding wetted area, and snowflake divertor[57, 59], which reduces the heat load by adding two more strike points in divertor region. Moreover, the snowflake divertor is characterized by the formation of a second order poloidal field null instead of a conventional first-order null, which increases weak poloidal field area and enhances curvature driven convection in divertor region[73]. These divertor configurations have been successfully implemented in many fusion devices, such as NSTX[67], TCV[53] and DIII-D[1], and their ability to dilate ELM heat pulses has been confirmed through both experiments and simulations[58, 71], which provides practical techniques for next-step high-power fusion device. Nevertheless, the implementation of advanced divertor configurations modifies the magnetic topology in the edge region and is therefore expected to impact the edge plasma properties, especially coupled peeling-ballooning instabilities and the subsequent ELM crashes. Evidence has already been shown in reference [53] and [1] that ELM size is dramatically altered after the formation of advanced divertor geometry in TCV and DIII-D. To understand the physics under these nonlinear phenomena, linear behaviors of the P-B mode need to be characterized first. Although linear stability boundaries of the P-B mode for various parameters in TCV with snowflake divertor have been studied in [48], details such as growth rate and mode structure, which is related to the ELM crash scenario, still have not been fully investigated.

In chapter 5, the fundamental characteristics of the peeling-ballooning modes and the ELM bursts are presented in the shifted-circle geometry (limiter tokamak geometry). Then the recent progress on ELM studies is reviewed. Finally, we take the snowflake (plus) divertor in DIII-D as an example to explore the changes in the linear behavior of the peeling-ballooning mode between different geometries. We summarize the results of linear simulations of peeling-ballooning mode in the pedestal region in the DIII-D tokamak with standard single-null (STD) and snowflake (SF) plus divertor configuration. Through the comparisons we found that the different linear behaviors of the ideal P-B mode are mainly governed by local magnetic shear on the outboard midplane. These results are consistent with the theoretical prediction that finite magnetic shear has a stabilizing effect for localized ballooning modes.

1.2 The micro-instabilities in the pedestal region

Having shown the importance of the peeling-ballooning modes in the pedestal region, we have to keep in mind that peeling-ballooning modes are not the only instabilities in the pedestal region, nor are they the only instabilities related to the ELM bursts. As an area with steep pressure profile and large bootstrap current, the pedestal region provides a large source of free energy, which can be held responsible for many micro-instabilities, such as the kinetic ballooning modes (KBM), the trapped electron modes (TEM), the electron temperature gradient modes (ETG) and so on. Type-I ELMs have proved to be one of the greatest threat to ITER operations in the future and many efforts have been devoted to the ELM mitigation studies. Unfortunately, no single method has been tested to be consistently working in mitigating ELMs and maintain high fusion performances. Understanding the physics beneath these methods for ELM control is crucial for us to develop more efficient and robust ones in the future.

However, the ELM cycle itself can not be fully understood in the scope of the macro-scale instability. One argument that has gain more and more supports from both experiments and simulations is that the pedestal micro-turbulence has indispensable impacts on the ELM cycles. For example, the time scale of the ELM burst is roughly Alfvénic, but the recovery period typically takes several tens of milliseconds[94]. During these recovery periods, electromagnetic fluctuations with frequency of roughly 300KHz have been observed on C-mod[10], which lead to the saturation of the pedestal formation. Similar high-frequency edge fluctuations have also been found in a Quiescent H-Mode plasma on DIII-D[92]. Fluctuations in both studies have been identified to be driven by the kinetic-ballooning modes (KBM). A comprehensive report about the pedestal fluctuations studies on DIII-D, NSTX and C-mod can be found in [28]. Another example comes from the experimental results on EAST Tokamak[78], which shows that small-amplitude, low-frequency oscillation appears in the quiescent phase of H-mode, when ELMs are suppressed by lower hybrid current drive and lithium coating. Overall, the pedestal turbulence needs careful investigations for the sake of better ELM control.

Depending on the driving mechanism, the pedestal turbulence can be categorized into two types: the drift-like and the interchange-like turbulence[61]. The interchange-like turbulence is driven by the magnetic curvature and profile gradient, which usually has the ballooning mode structure. One example is the Alfvénic ion temperature gradient mode (AITG), an electromagnetic instability driven by the ion temperature gradient. Many work has been done on the AITG instability using different theoretical or numerical tools and the following just summarizes part of them: Horton *et al*[35] used a fluid-kinetic hybrid model to study the AITG theoretically; Hong *et al*[32] improved Horton's model and used the shooting method to calculate growth rate; Andersson *et al*[2] first used fully toroidal fluid and obtained similar results as kinetic model; Dong et al[12] used a one-dimensional kinetic integral equation. Particularly, Snyder[66] categorized the AITG as one type of the kinetic ballooning mode (KBM) and studied the mode numerically using a flux-tube gyro-fluid code. According to these studies, the AITG can exist below the ideal MHD threshold if the background $\eta_i = L_n/L_{Ti}$ exceeds certain critical value. Moreover, in contrast to the electrostatic ion temperature gradient (ITG), the AITG becomes more unstable as the pedestal pressure(β) increases. The most recent simulation work of the KBM in the pedestal region is Wan *et al*[75], which used the gyro-kinetic code GEM.

The drift-like instabilities also draws free energy from background profile, with a different energy feedback channel than the interchange-type instabilities. The trapped-electron modes (TEM)[8] are one of the most common toroidal drift-instabilities found in the pedestal region, which absorb free energy from background electron pressure gradient and are driven unstable by the trapped electrons in the banana orbits in the bad-curvature (outboard midplane). Recent numerical studies on DIII-D[23] and ASDEX-upgrade[31] have identified that the TEM exists in the pedestal as an universal instability and under certain circumstances, could be the dominant instability, instead of the well-known KBM instability. The most interesting part of the TEM studies in the pedestal region is that the linear poloidal mode structure constantly localizes at unconventional positions, i.e. at poloidal positions other than the outboard midplane. For example, Fulton *et al* found that the collisionless trapped electron modes(CTEM) localize at $\pm\pi/2$ ballooning angle, i.e. at the top and near the X-point of the DIII-D Tokamak, when the background profile gradients are steep enough. The similar poloidal mode structure is also found in Wang *et al*[77] and Hatch *et al*[31]. Novakovskii *et al*[50] used the ballooning analysis and theoretically predicted a new drift-resistive branch in the pedestal region with peaks at $\pm\pi/2$ ballooning angle. Xie *et al*[85] conducted a comprehensive numerical study using the GTC codes and concluded that the toroidal drift-modes could have unconventional poloidal structure with multiple peaks when the background profiles are steep enough.

In chapter 6, we present a new type of drift-modes in the pedestal region of DIII-D tokamak, the drift-Alfven modes, which absorb free energy also from the electron pressure profile and are driven unstable by the coupling with shear Alfven waves. We found that the drift-Alfven modes also have unconventional poloidal mode structure, like the TEMs. Furthermore, the heat transport induced by the drift-Alfven turbulences is numerically studied using BOUT++ nonlinear global simulations.

1.3 The impurity transport in the pedestal region

We mentioned previously that the type-I ELMs could be catastrophic to the H-mode operations in the Tokamaks, as they release a huge amount of pedestal energy to the scrap-off layer and degrade the performance as a whole. One may assume that the fusion will be much easier if we can find a way to prevent any sort of energy lost from the pedestal region. However, the results may remain bad owing to a different problem: the impurities in the edge region. The plasma facing components (PFCs) in the first wall and the divertor plates are usually made by moderate-Z materials (carbon, boron, beryllium) deposited on high-Z tungsten or stainless steal. As the particle (heat) flux traverse through the edge, it may scrape off some of these molecules, which are quickly ionized, for example, B^{+5}. These moderate/high-Z ions are called the 'impurities'. After some time, the impurities will accumulate and form a natural gradient from the vessel wall to the core region. As the gradients of the impurities are opposite to the gradients of the primary ions, the impurities can reach the core region through anomalous radial transport induced by drift-wave turbulence, which will cause the degrade of the whole fusion performance, or even disruption[80].

Therefore, the impurity exhaust mechanism is necessary at the edge region. The ideal candidates are the type-II/type-III ELMs, which appear as high frequency, low amplitude energy bursts[94]. Type-II/Type-III ELMs can still maintain H-mode performance while preventing the accumulation of the impurities in the edge. Moreover, it is also found in experiments that by puffing small amount of high-Z impurities to the edge region, we can effectively radiate almost 90% of the outward heat flux and reach plasma detachment, while maintaining H-mode[29]. Therefore, impurities as the inevitable results of plasma-wall interactions, are closely related to the pedestal physics and thus, the whole fusion performance. Understanding the transport characteristics of the impurities is crucial to ITER performance in the future.

In chapter 4, we will focus on the linear characteristics of the impurity density driven drift-waves. The theoretical study is closely related to the experimental observations of the impurity anomalous transport features, for example, Alcator C-mod[21, 55], TEXT[34] and MST[43]. Besides, the transport of impurities in the stellarator is also studied.

1.4 The BOUT++ framework

Generally speaking, the BOUT++ codes[1][15] are the framework of solving coupled partial differential equations in complicated geometry with flexibility in the boundary conditions. Written in C++ with objected-oriented structure, BOUT++ codes inherent many merits from its predecessor, the BOUT code[86] (name from Boundary plasma Turbulence) written in Fortran, for example, the technique to deal with the X-point in real tokamak geometry, but provides more convenience for computational physicist. For example, for most of the time, only the physics module need to be modified in order to tackle a new problem, while the other modules, such as the mesh and the solver, need little change. These conveniences make BOUT++ codes very easy to be adopted, especially by physicists who want to focus on the physics aspects instead of the coding techniques.

Technically speaking, BOUT++ is a three-dimensional finite-difference grid code used to model collisional edge plasmas in a toroidal geometry. Time evolution is primarily through the implicit New Krylov method. A range of finite difference schemes are used, including central difference, upwinding

[1]For more informations, check the websites: https://bout.llnl.gov/ and https://github.com/boutproject/BOUT-2.0

and WENO. Several different algorithms are implemented for Laplacian inversion, such as tridiagonal solver, a band-solver and the parallel diagonal dominant (PDD) algorithm. BOUT++ codes are highly parallelized in $x - y$ two-dimensional plane, while there is no parallelization in the z direction (periodic direction). The computing efficiency is well scaled with the number of processors[49].

BOUT++ codes have shown excellent agreement with the experiment and other MHD codes in P-B modes and ELM burst simulation regime. Now, many fluid models are developed to expand the capability of BOUT++ codes. For example, the six-field model[84] is used to calculate the heat flux in H-mode discharge; the gyro-landau fluid[91] is developed to simulate the micro-instabilities, such as the kinetic ballooning mode (KBM); the neutral transport model[79] is used to study the SMBI injections.

Chapter 2

BOUT++ codes Verification: Diffusion equations

2.1 2-D diffusion equation in planar geometry

The first straightforward setup for the verification of BOUT++ codes is diffusion equation in two-dimensional planar geometry. The diffusion equation is:

$$\frac{\partial T}{\partial t} = \chi \nabla^2 T = \chi \left(\frac{\partial^2 T}{\partial x^2} + \frac{\partial^2 T}{\partial y^2} \right) \tag{2.1}$$

where T could be temperature, density or pressure, χ is the diffusivity. This equation can be solved analytically by separating the variables. With the Neumann boundary condition ($\frac{\partial T}{\partial x}|_{x=0} = \frac{\partial T}{\partial x}|_{x=L} = 0$, $\frac{\partial T}{\partial y}|_{y=0} = \frac{\partial T}{\partial y}|_{y=L} = 0$), the analytical solution is:

$$T(x,y,t) = A_{0,0} + \sum_{m=1}^{\infty} \sum_{n=1}^{\infty} A_{m,n} \cos\left(\frac{n\pi}{L} x\right) \cos\left(\frac{m\pi}{L} y\right) \exp\left(-\chi \frac{\pi^2 (m^2+n^2)}{L^2} t\right) \tag{2.2}$$

where L is the length of the square domain and $A_{*,*}$ could be any real numbers. The equilibrium for BOUT++ simulation is generated with Python script. The resolution for both directions is 64 and the length $L = 64 * 0.05 = 3.2$. As in figure (2.1). The initial condition is $T(x,y,0) = 1 + \cos(\pi x/L)\cos(2\pi y/L)$

for single mode verification. Besides, the boundary conditions are Neumann and the diffusivity (χ) is set to be unity.

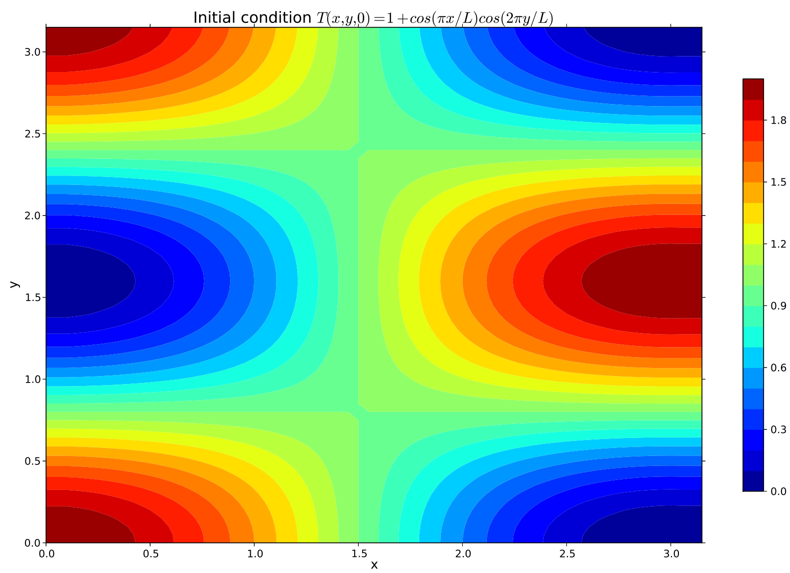

Figure 2.1: Contour plot of the initial condition for the single mode verification of the 2-D diffusion equation in planar geometry. $T(r, \theta, t = 0) = 1 + \cos(\pi x/L)\cos(2\pi y/L), n_x = n_y = 64$.

The verification results are shown in figure (2.2), where the analytical solution and BOUT++ simulation results are compared at four different positions. We can see that excellent agreements are obtained for this case.

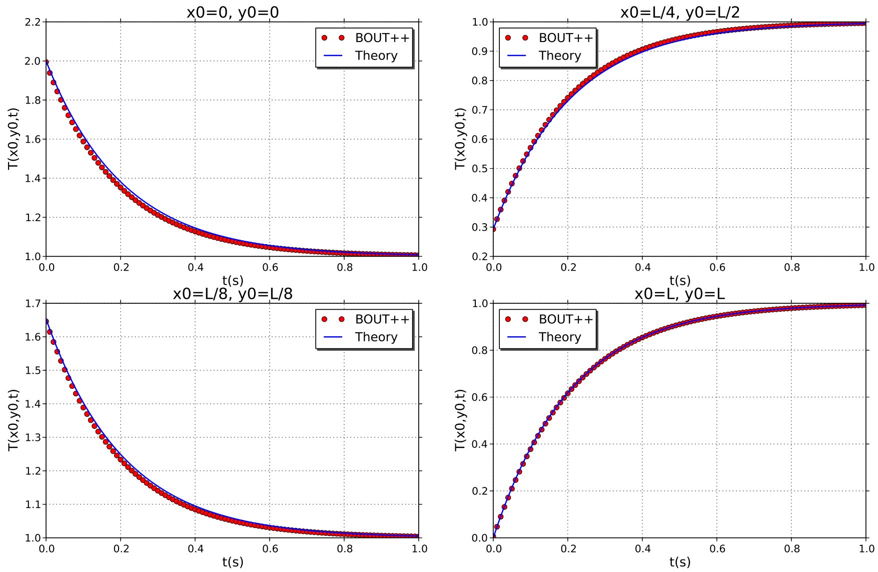

Figure 2.2: The comparison between the analytical solution (Eq. 2.2) of 2-D diffusion equation in planar geometry and the linear simulation results from BOUT++ codes at four different positions.

2.2 2-D diffusion equation in cylindrical geometry

In two-dimensional cylindrical geometry (r, θ), the diffusion equation is:

$$\frac{\partial T}{\partial t} = \chi \left(\frac{\partial^2 T}{\partial r^2} + \frac{1}{r}\frac{\partial T}{\partial r} + \frac{1}{r^2}\frac{\partial^2 T}{\partial \theta^2} \right) \tag{2.3}$$

like the previous analysis, with Neumann boundary condition ($\frac{\partial T}{\partial r}|_{r=r_0} = 0$), the analytical solution is:

$$T(r, \theta, t) = \sum_{m=0}^{\infty}\sum_{k=1}^{\infty} A_{m,k} J_m \left(\frac{B_{m,k}}{r_0} r \right) \cos(m\theta) \exp\left(-\chi \frac{B_{m,k}^2}{r_0^2} t \right) + C \tag{2.4}$$

where C is arbitrary constant and $B_{m,k}$ is the kth zero of the function $J'_m(r)$. The cylindrical equilibrium for BOUT++ simulation is generated with radial resolution $n_r = 32$ and poloidal resolution $n_\theta = 256$. The radial boundary is fixed at $r_0 = 1.8$, where the Neumann boundary condition is applied. Due to the singularity at the center of the circle, a hole with radius $r = 0.05$ is removed from the center of the simulation domain. As the size of the hole is much smaller than the whole radial domain, we expect that the analytical solution of the diffusion equation should still be the same as equation (2.4).

The initial condition for the linear simulation is $T(r, \theta, t = 0) = \cos(2\theta)$, as shown in figure(2.4). In order to calculate the 2-D temperature profile at any given time ($t > 0$) analytically, we first need to decompose the initial temperature profile into harmonics $A_{m,k} J_m \left(\frac{B_{m,k}}{r_0} r\right) \cos(m\theta)$. It is straightforward to find that the only sinusoidal mode number is $m = 2$. Therefore, we only need to compute the coefficients $A_{2,k}$ for each k. Although it is potentially a infinite series, the harmonics become less important as k increases. The coefficients $A_{2,k}$ for $k = 1 \sim 20$ are shown in table 2.1. The calculation is based on the orthogonality of Bessel functions $J_m \left(B_{m,k} \frac{r}{r_0}\right)$ (Appendix A: Bessel Function) in region $[0, r_0]$. The sum of the first 20 Bessel func-

k	1	2	3	4	5	6	7	8	9	10
$A_{2,k}$	2.51	1.02	0.64	0.49	0.39	0.32	0.28	0.24	0.22	0.20
k	11	12	13	14	15	16	17	18	19	20
$A_{2,k}$	0.18	0.16	0.15	0.14	0.13	0.12	0.12	0.11	0.10	0.10

Table 2.1: The first 20 coefficients $A_{2,k}$ for equation $1 = \sum_{k=1}^{\infty} A_{2,k} J_2 \left(\frac{B_{2,k}}{r_0} r\right)$, where J_2 denotes Bessel function of the first kind (J_m) with $m = 2$ and $B_{2,k}$ is the k_{th} zeros of J_2'.

tions $f(r) = \sum_{k=1}^{20} A_{2,k} J_2 \left(B_{2,k} \frac{r}{r_0} \right)$ is shown in figure (2.3). We can see that the agreement between $f(r)$ and constant function $g(r) = 1$ is quite good for $0 < r < 1.8$, with a maximum error $\sim 10\%$. Therefore, the analytical solution with this particular initial condition is:

$$T(r, \theta, t) = \sum_{k=1}^{20} A_{2,k} J_2 \left(B_{2,k} \frac{r}{r_0} \right) \exp \left(-\frac{B_{2,k}^2}{r_0^2} t \right) \tag{2.5}$$

The verification results from linear BOUT++ simulation are shown in figure

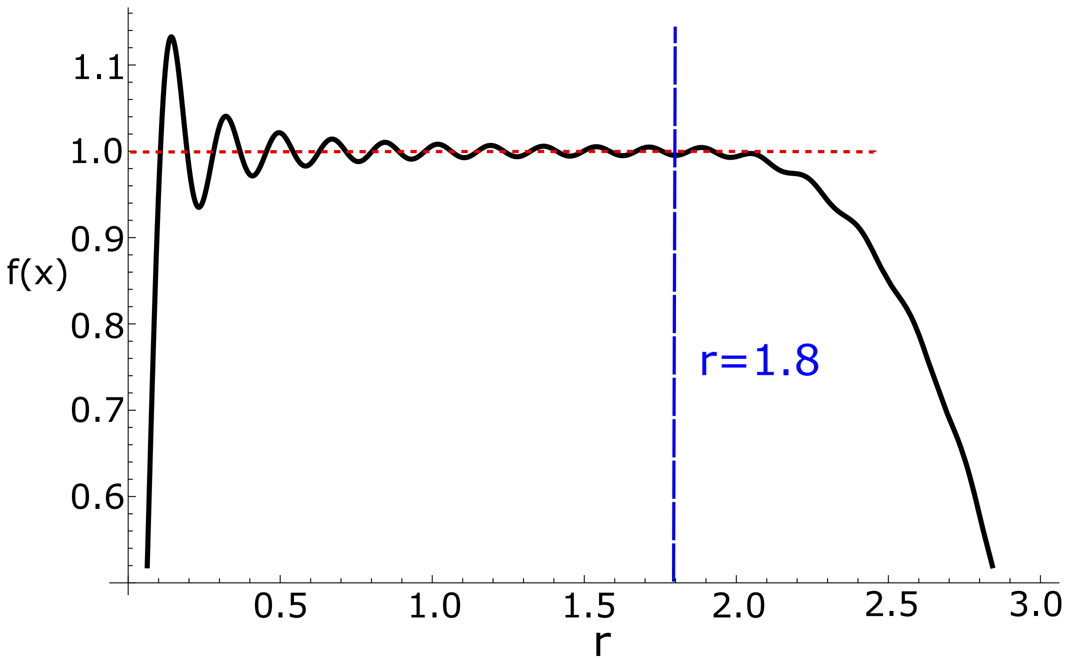

Figure 2.3: The comparison between the sum of the first 20 Bessel functions $f(r) = \sum_{k=1}^{20} A_{2,k} J_2 \left(B_{2,k} \frac{r}{r_0} \right)$ and the constant function $g(r) = 1$ in region $0 < r < 1.8$.

(2.5). The time evolution of the temperature at four positions with different radial and poloidal coordinates are compared with the analytical solution (Eq.

2.5). We can see that the numerical and analytical results are highly consistent. Besides, the time evolution of the total energy in simulation domain ($0.05 < r < 1.8, 0 < \theta < 2\pi$) is shown in figure (2.6). As the Neumann boundary condition in the radial direction implies that the total energy will conserve theoretically, the total energy is supposed to be zero at any time. Figure (2.6) demonstrates that the error of the total energy is only about 1×10^{-7}. This study shows the accuracy of the BOUT++ framework in non-Cartesian grids with self-defined metric tensor.

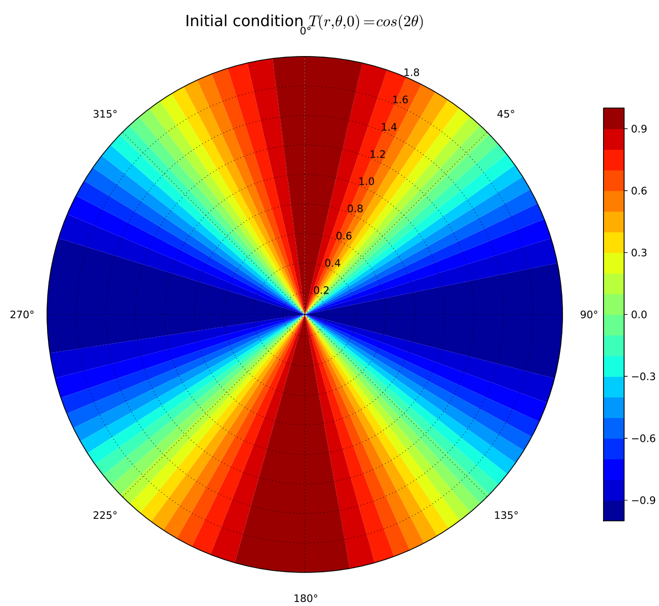

Figure 2.4: Contour plot of the initial condition for the single mode verification of the 2-D diffusion equation in cylindrical geometry. $T(r, \theta, t = 0) = \cos(2\theta), n_r = 32, n_\theta = 256$.

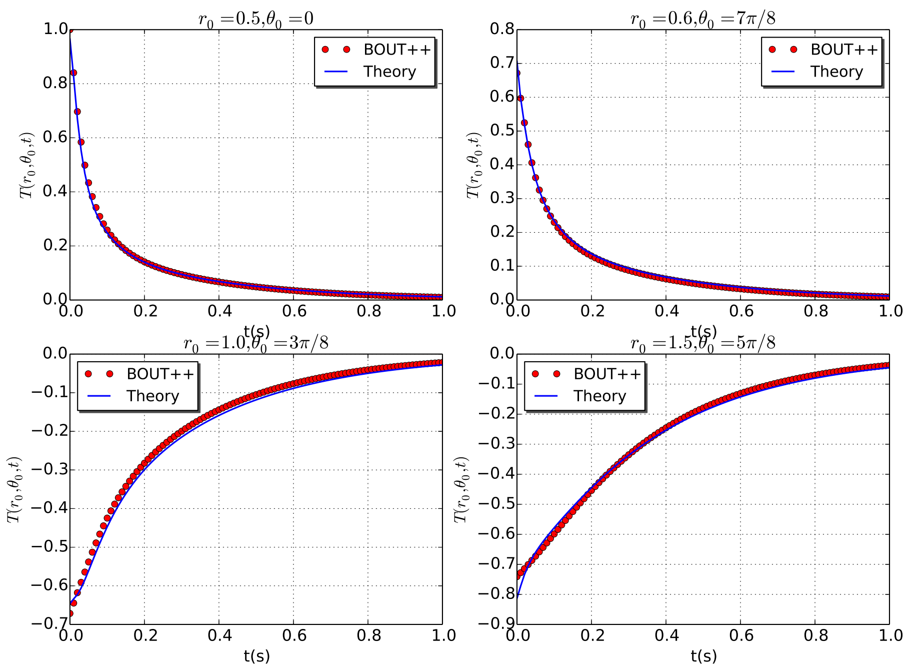

Figure 2.5: The comparison between the analytical solution (Eq. 2.5) of the 2-D diffusion equation in cylindrical geometry and the linear simulation results from BOUT++ codes at four different positions.

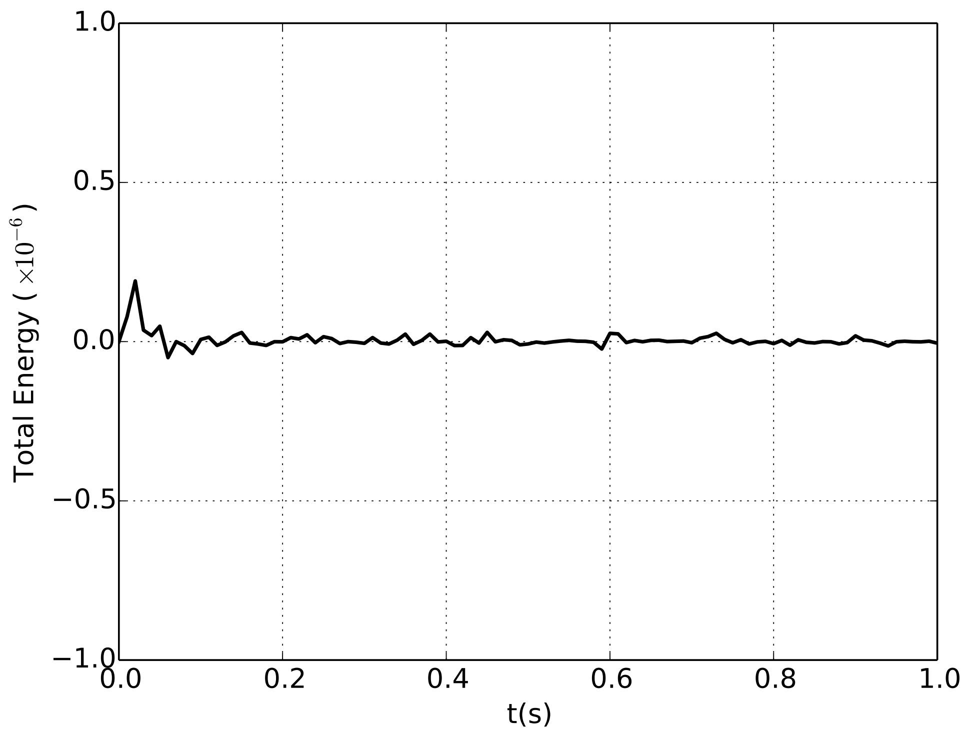

Figure 2.6: The time history of the total energy in the cylindrical domain $(0.05 < r < 1.8, 0 < \theta < 2\pi)$. The total energy at any moment t_a is defined as

$$\sum_{n_r=1}^{32} \sum_{n_\theta=1}^{256} T(n_r, n_\theta, t_a)$$

.

Chapter 3

Firehose Instability

3.1 Background and Motivation

Firehose instability get its name from the actual firehose used by the firemen. When water is turned on, high parallel pressure from the fire hydrate will create an extreme pressure ratio ($p_{\parallel} \gg p_{\perp}$)between parallel and perpendicular direction inside firehose, which causes firehose to swing in perpendicular direction. The swing caused by firehose instability is so powerful that it usually takes several firemen to stabilize.

In ideal MHD regime, one of the most important assumptions is the isotropy of the plasmas. This seems to be natural to our intuitive knowledge, however, there are various cases where isotropy of plasma is significantly violated, especially when magnetic field is presented. For example, in fusion device such as Tokamak, particles are often heated by Electron/Ion Cyclotron Resonance Heating (ECRH/ICRH), which increases kinetic energy of particles mainly in perpendicular direction of magnetic field. Although kinetic energy could be distributed to parellel direction gradually through collisions, in short time scale this will cause $p_{\perp} \gg p_{\parallel}$, which eventually could induce

"Mirror Instability"[33]. Besides fusion reactors, this type of instability is also very common in planetary and cometary magnetosheaths and other high beta environments[68]. One typical example is the electrons in solar flare. In contrast to ECRH/ICRH, particle acceleration mechanisms in solar flares exhibit a preference of energizing particles in parallel direction of magnetic field[52]. Therefore, anisotropy is expected during the impulsive phase of a flare, and "Firehose Instability" will be induced when anisotropy exceed certain level[37, 82]. Another example of firehose instability in anisotropic magnetized plasma is the hose-pipe instability of thin or elongated galaxies. When the long-to-short axis ratio is very large (10 : 1), instabilities occur and greatly reduce the ratio. This instability is probable reponsible for the fact that elliptical galaxies never have axis ratios more extreme than about 3 : 1. The difference between this instability and firehose instability is that firehose instability is driven by magnetic tension and pressure force, which this instability is driven by gravity and centrifugal force.

The following sections of this chapter will be focused on the analytical studies of the firehose instability. A double-adiabatic MHD formulary based on the modifications of the ideal MHD equations is first derived and the linear behaviors are studied analytically. Then, a more realistic model based on anisotropic kinetic theory is constructed and the linear dispersion relation of firehose instability is compared with the first model. Besides, BOUT++ linear simulations are conducted using the double-adiabatic MHD model and excellent agreements are achieved between numerical and theoretical results.

3.2 Double Adiabatic MHD

Magnetohydrodynamics(MHD) describes fluctuations in plasma which changes slowly, comparing to the ion cyclotron frequency (ω_{ci})[33]. The classic set of fluid equations for ideal MHD are:

$$\frac{\partial \rho}{\partial t} + \nabla \cdot (\rho \boldsymbol{v}) = 0 \tag{3.1}$$

$$\rho \left(\frac{\partial \boldsymbol{v}}{\partial t} + (\boldsymbol{v} \cdot \nabla) \boldsymbol{v} \right) = -\nabla p + \frac{1}{\mu_0} (\nabla \times \boldsymbol{B}) \times \boldsymbol{B} \tag{3.2}$$

$$\frac{\partial p}{\partial t} + \gamma p (\nabla \cdot \boldsymbol{v}) + \nabla p \cdot \boldsymbol{v} = 0 \tag{3.3}$$

$$\frac{\partial \boldsymbol{B}}{\partial t} = \nabla \times (\boldsymbol{v} \times \boldsymbol{B}) \tag{3.4}$$

There are several assumptions that need to be made in order to make these equations applicable:

- No resistivity, $\eta \rightarrow 0$.
- Quasi-neutrality, $\delta n_e = \delta n_i$.
- Relative velocity between electron and ion is small, $|\boldsymbol{v_i} - \boldsymbol{v_e}| \ll |\boldsymbol{v_i}|$.
- Adiabatic condition, $p\rho^{-\gamma} = Const.$
- Isotropic plasma, $\overleftrightarrow{\boldsymbol{p}} = p \overleftrightarrow{\boldsymbol{I}}$.

3.2.1 Anisotropic plasma

When the anisotropy of the plasma is taken into consideration, the original set of the MHD equations need to be modified. The straightforward thought is to change isotropic pressure tensor $\overleftrightarrow{\boldsymbol{p}} = p\overleftrightarrow{\boldsymbol{I}}$ to the anisotropic form [42]:

$$\overleftrightarrow{\boldsymbol{p}} = p_{\parallel}\boldsymbol{bb} + p_{\perp}(\overleftrightarrow{\boldsymbol{I}} - \boldsymbol{bb}) \tag{3.5}$$

where $\boldsymbol{b}$ is the unit vector along the magnetic field. If one let $\boldsymbol{b} = \boldsymbol{e_z}$, then the pressure tensor can be written in Cartesian coordinates as:

$$\overleftrightarrow{\boldsymbol{p}} = \begin{pmatrix} p_{\perp} & 0 & 0 \\ 0 & p_{\perp} & 0 \\ 0 & 0 & p_{\parallel} \end{pmatrix}.$$

With this anisotropic pressure tensor, the divergence of the pressure tensor used in the momentum equation can be expressed as:

$$(\nabla \cdot \overleftrightarrow{\boldsymbol{p}})_j = \frac{\partial}{\partial x_i} p_{ij} = \frac{\partial}{\partial x_i}(p_{\parallel} b_i b_j + p_{\perp}(\delta_{ij} - b_i b_j)) \tag{3.6}$$

$$= (\frac{\partial}{\partial x_i}(p_{\parallel} - p_{\perp}))b_i b_j + (p_{\parallel} - p_{\perp})(\frac{\partial b_i}{\partial x_i})b_j \tag{3.7}$$

$$+(p_{\parallel} - p_{\perp})b_i(\frac{\partial b_j}{\partial x_i}) + \frac{\partial p_{\perp}}{\partial x_i}\delta_{ij} \tag{3.8}$$

Hence, In vector form

$$\nabla \cdot \overleftrightarrow{\boldsymbol{p}} = (\boldsymbol{b} \cdot \nabla)(p_{\parallel} - p_{\perp})\boldsymbol{b} + (p_{\parallel} - p_{\perp})(\nabla \cdot \boldsymbol{b})\boldsymbol{b} + (p_{\parallel} - p_{\perp})(\boldsymbol{b} \cdot \nabla \boldsymbol{b}) + \nabla p_{\perp} \tag{3.9}$$

Assume that anisotropic plasma is adiabatic in both parallel and perpendicular direction, which is called the '**double adiabatic condition**'. With this assumption, the pressure equation can be rewritten in the similar form[1] in the parallel and perpendicular direction:

$$\frac{dp_\parallel}{dt} + p_\parallel(\nabla \cdot \boldsymbol{v}) + 2p_\parallel \boldsymbol{b} \cdot (\boldsymbol{b} \cdot \nabla)\boldsymbol{v} = 0 \tag{3.10}$$

$$\frac{dp_\perp}{dt} + 2p_\perp(\nabla \cdot \boldsymbol{v}) - p_\perp \boldsymbol{b} \cdot (\boldsymbol{b} \cdot \nabla)\boldsymbol{v} = 0 \tag{3.11}$$

in which,

$$\frac{d}{dt} = \frac{\partial}{\partial t} + \boldsymbol{v} \cdot \nabla$$

The continuity equation the and magnetic field equation will not be changed:

$$\frac{\partial \rho}{\partial t} + \nabla \cdot (\rho \boldsymbol{v}) = 0 \tag{3.12}$$

$$\frac{\partial \boldsymbol{B}}{\partial t} = \nabla \times (\boldsymbol{v} \times \boldsymbol{B}) \tag{3.13}$$

The momentum equation, as mentioned before, will be in a similar form, but with a much more complicated term for pressure divergence.

$$\rho \left(\frac{\partial \boldsymbol{v}}{\partial t} + (\boldsymbol{v} \cdot \nabla)\boldsymbol{v} \right) = -\nabla \cdot \overleftrightarrow{\boldsymbol{p}} + \frac{1}{\mu_0}(\nabla \times \boldsymbol{B}) \times \boldsymbol{B} \tag{3.14}$$

in which,

$$\nabla \cdot \overleftrightarrow{\boldsymbol{p}} = (\boldsymbol{b} \cdot \nabla)(p_\parallel - p_\perp)\boldsymbol{b} + (p_\parallel - p_\perp)(\nabla \cdot \boldsymbol{b})\boldsymbol{b} + (p_\parallel - p_\perp)(\boldsymbol{b} \cdot \nabla \boldsymbol{b}) + \nabla p_\perp$$

Equations (3.10), (3.11), (3.12), (3.13) and (3.14) compose the complete set of the double-adiabatic MHD model. To be noticed, the number of the variables increases to 9 ($\boldsymbol{B}, \boldsymbol{v}, n, p_\parallel, p_\perp$).

[1]See Appendix for detailed derivations

3.2.2 Equilibrium and Linearization

To study the instabilities linearly, we need to first find the equilibrium of the system and then linearize the equations. The equilibrium could be obtained by setting all the time derivatives to be zeros ($\partial/\partial t = 0$). Because equilirium of this set of equations is not our primary interest, we can just choose the trivial solution, which implies that all the equilibium values are constant in space:

$$\{\rho, \boldsymbol{v}, \boldsymbol{B}, p_{\|}, p_{\perp}\}_{Equilibrium} = \{\rho_0, \boldsymbol{0}, \boldsymbol{B_0}, p_{\|0}, p_{\perp 0}\} \tag{3.15}$$

Then, each variable can be expressed as the equilibrium value plus the perturbed value:

$$\rho = \rho_0 + \rho_1, \boldsymbol{v} = \boldsymbol{v}_1, \boldsymbol{B} = \boldsymbol{B}_0 + \boldsymbol{B}_1, p_{\perp} = p_{\perp 0} + p_{\perp 1}, p_{\|} = p_{\|0} + p_{\|1} \tag{3.16}$$

New parameters are introduced for the simplification:

$$\boldsymbol{b}_0 = \boldsymbol{B}_0/B_0, \boldsymbol{b}_1 = \boldsymbol{B}_1/B_0, \boldsymbol{\xi} = \int^t \boldsymbol{v}_1 dt, v_A = B_0/\sqrt{\mu_0\rho_0} \tag{3.17}$$

We linearize the equations (3.10) to (3.14) and only keep the first order terms, then the continuity equation becomes:

$$\rho_1 = -\rho_0(\nabla \cdot \boldsymbol{\xi}) \tag{3.18}$$

the magnetic field equation:

$$\boldsymbol{b}_1 = (\boldsymbol{b}_0 \cdot \nabla)\boldsymbol{\xi} - \boldsymbol{b}_0(\nabla \cdot \boldsymbol{\xi}) \tag{3.19}$$

the perpendicular pressure equation:

$$p_{\perp 1} = -2p_{\perp 0}(\nabla \cdot \boldsymbol{\xi}) + p_{\perp 0}\boldsymbol{b}_0 \cdot (\boldsymbol{b}_0 \cdot \nabla)\boldsymbol{\xi} \tag{3.20}$$

the parallel pressure equation:

$$p_{\parallel 1} = -p_{\parallel 0}(\nabla \cdot \boldsymbol{\xi}) - 2p_{\parallel 0}\boldsymbol{b}_0 \cdot (\boldsymbol{b}_0 \cdot \nabla)\boldsymbol{\xi} \tag{3.21}$$

and the momentum equation:

$$\frac{\partial^2 \boldsymbol{\xi}}{\partial t^2} = -\frac{1}{\rho_0}\nabla \cdot \overleftrightarrow{\boldsymbol{p}_1} + v_A^2((\boldsymbol{b}_0 \cdot \nabla)\boldsymbol{b}_1 - (\nabla \boldsymbol{b}_{\mathbf{1}}) \cdot \boldsymbol{b}_0) \tag{3.22}$$

where,

$$\begin{aligned}\nabla \cdot \overleftrightarrow{\boldsymbol{p}_1} = \quad & -2p_{\perp 0}\nabla(\nabla \cdot \boldsymbol{\xi}) + p_{\perp 0}(\nabla(\boldsymbol{b}_0 \cdot \nabla)\boldsymbol{\xi}) \cdot \boldsymbol{b}_0 + (p_{\parallel 0} - p_{\perp 0})(\boldsymbol{b}_0 \cdot \nabla)^2\boldsymbol{\xi} \\ & + (p_{\perp 0} - 4p_{\parallel 0})(\boldsymbol{b}_0 \cdot (\boldsymbol{b}_0 \cdot \nabla)^2\boldsymbol{\xi})\boldsymbol{b}_0 + p_{\perp 0}((\boldsymbol{b}_0 \cdot \nabla)(\nabla \cdot \boldsymbol{\xi}))\boldsymbol{b}_0\end{aligned}$$

We assume that the perturbed parts are of the form $\exp(i\boldsymbol{k} \cdot \boldsymbol{r} - i\omega t)$, then derivatives can be replaced by:

$$\frac{\partial}{\partial t} \to -i\omega, \nabla \to i\boldsymbol{k}, \boldsymbol{b}_0 \cdot \nabla \to ik_\parallel \tag{3.23}$$

Applying these relations to equation (3.18) through (3.22), after some complicated algebra[2], we can get the dispersion relation:

$$\omega^4 - A\omega^2 - B = 0 \tag{3.24}$$

in which,

$$\begin{aligned} A &= \left(\frac{2p_{\perp 0}}{\rho_0} + v_A^2\right)k^2 + \frac{1}{\rho_0}(2p_{\parallel 0} - p_{\perp 0})k_\parallel^2 \\ B &= \left(\frac{p_{\perp 0}^2}{\rho_0^2} - 3\frac{p_{\parallel 0}}{\rho_0}\left(2\frac{p_{\perp 0}}{\rho_0} + v_A^2\right)\right)k^2 k_\parallel^2 + \frac{1}{\rho_0^2}(3p_{\parallel 0}^2 + p_{\perp 0}(3p_{\parallel 0} - p_{\perp 0}))k_\parallel^4 \end{aligned}$$

[2]see Appendix for detail

3.2.3 Dispersion relation of the firehose instability

Equation (3.24) describes the dispersion relation of waves that can propagate along arbitrary directions. Without the loss of generality, we assume that the waves only propagate along the magnetic field, i.e. $\boldsymbol{k} = k_\parallel \boldsymbol{b}_0$. Then the dispersion relation becomes:

$$\omega^4 - \left(\frac{p_{\perp 0}}{\rho_0} + \frac{2p_{\parallel 0}}{\rho_0} + v_A^2\right) k_\parallel^2 \omega^2 - \frac{3p_{\parallel 0}}{\rho_0}\left(\frac{p_{\parallel 0}}{\rho_0} - v_A^2 - \frac{p_{\perp 0}}{\rho_0}\right) k_\parallel^4 = 0 \qquad (3.25)$$

This is a quadratic equation for ω^2, and it is quite straightforward to verify[3] that $\Delta = A^2 + 4B \geq 0$. Therefore, the roots (ω^2) are always real. Then there are two possible cases:

- $\omega^2 > 0 \Rightarrow \omega \in \mathfrak{R} \Rightarrow$ perturbed parts $\propto \exp(-i\omega t)$
- $\omega^2 < 0 \Rightarrow \omega = \pm i\gamma \in \mathfrak{J} \Rightarrow$ perturbed parts $\propto \exp(\pm\gamma t)$

In the first case, we will just get a purely oscillating mode. However, in the second case, the wave evolves as a superposition of a decaying mode and a growing mode. The decaying mode will soon disappear, but growing mode will make wave amplitude larger and larger, and eventually cause nonlinear structure. Then the criteria of this type of instabilities is $\omega^2 < 0$. Plug into equation (3.25), we find:

$$\frac{p_{\parallel 0}}{\rho_0} - \frac{p_{\perp 0}}{\rho_0} > v_A^2 \qquad (3.26)$$

[3]see Appendix for proof

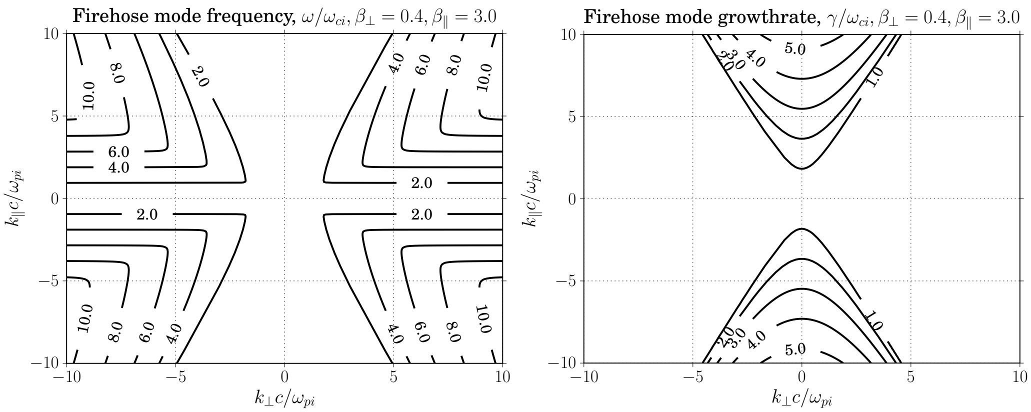

Figure 3.1: The contour plot of the real frequency and growth rate of the firehose instability in the parallel and perpendicular wave number plane. The parallel and perpendicular normalized pressure are $\beta_\parallel = 3.0$ and $\beta_\perp = 0.4$. The label on the contour lines represent the normalized growth rate and real frequency.

This means that in the anisotropic plasma, when parallel pressure exceeds perpendicular pressure by certain level, wave propagating along magnetic field will become unstable and this is what is called "**Firehose Instability**". This criteria can also be expressed as following:

$$\beta_\parallel - \beta_\perp > 2 \tag{3.27}$$

,in which $\beta_\parallel = \dfrac{2\mu_0 p_{\parallel 0}}{B_0^2}, \beta_\perp = \dfrac{2\mu_0 p_{\perp 0}}{B_0^2}$ are ratios between plasma pressure and magnetic pressure in parallel and perpendicular directions. If the perpendicular wave number is not zero, the results become a little complicated. Figure (3.1) shows the contour of the real frequency and growth rate in wavenumber space. Although the background pressure ratio exceeds the firehose criteria ($\beta_\parallel - \beta_\perp > 2.0$) and the mode should exponentially decay if ($k_\perp$=0), the real frequency appears if ($k_\perp > 2.0$). Also, if the perpendicular wavenumber is significantly larger than the parallel wavenumber ($k_\perp/k_\parallel > 2$), the growth rate becomes zero and the mode becomes stable.

3.2.4 BOUT++ linear simulation results

The analytical results, including the dispersion relation (3.25) and firehose instability criteria (3.26), are compared with the linear simulation using BOUT++ codes in this section. The planar grid is used with the resolution $nx = 32, ny = 128, nz = 3, dx = dy = 0.05$, where background magnetic field is in y-direction. The equations used are (3.18) to (3.22) with normalization:

$$\tilde{t} = t\frac{v_A}{a}, \tilde{x} = x/a, \tilde{p_\perp} = p_\perp/p_{\perp 0}, \tilde{p_\parallel} = p_\parallel/p_{\perp 0}, \tilde{\rho} = \rho/\rho_0, \tilde{\boldsymbol{B}} = \boldsymbol{B}/B_0 \tag{3.28}$$

Without the loss of generality, we fix the background perpendicular pressure that $\beta_\perp = 2.0$. Under such normalization, background values are

$$\tilde{\rho_0} = 1.0, \tilde{p_{\perp 0}} = 1.0, \tilde{B_0} = 1.0, \tilde{v_0} = 0 \tag{3.29}$$

and the initial pertubation is set to be $\delta\boldsymbol{B}(\boldsymbol{r}) = 0.01\boldsymbol{e_x}\sin(2\pi my/L_y)$ (Figure 3.2), which implies that $k_\perp = 0$. Background values $p_{\parallel 0}$ and mode number m can be adjusted to simulate different situations. The initial condition and the typical exponential growing mode are shown in figure (3.2). Two different set of parameters are used to compared with the analytical results of both the purely oscillating mode ($\beta_\parallel - \beta_\perp = 1.0$) and the exponentially growing mode ($\beta_\parallel - \beta_\perp = 4.0$). First, we assume that $\beta_\parallel - \beta_\perp = 4.0$, and vary mode number m from 6.0 to 12.0. Then change the beta value to $\beta_\parallel - \beta_\perp = 1.0$. Comparison with theoretical results for both cases yield good agreement (Figure 3.3).

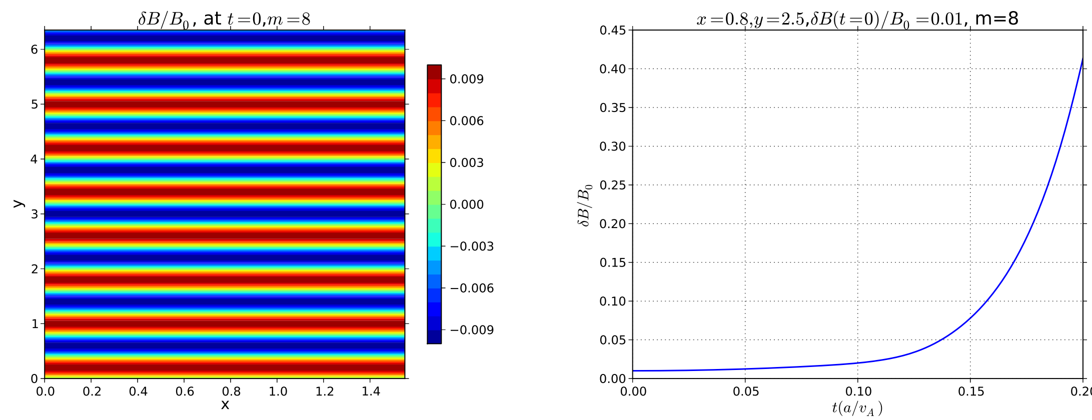

Figure 3.2: The left figure shows the contour plot of the initial condition and the right figure shows an example of exponential growing mode under certain circumstances.

Original data for growth rate in Figure 3.3 ($\beta_\| - \beta_\perp = 4.0$):

m	6	7	8	9	10	11	12
$k_\|$	5.89	6.87	7.85	8.84	9.82	10.80	11.78
γ	5.91	6.85	7.78	9.20	9.88	10.82	11.70

Original data for frequency in Figure 3.3 ($\beta_\| - \beta_\perp = 1.0$):

m	6	7	8	9	10	11	12
$k_\|/\sqrt{2}$	4.17	4.86	5.55	6.25	6.94	7.64	8.33
ω	4.16	4.84	5.52	6.15	6.90	7.60	8.16

Another verfication fixed mode number $m = 8.0$ and varied difference of beta values ($\beta_\| - \beta_\perp$)from 3.0 to 8.0 (Figure 3.4), which also indicates good agreement.

Original data of Figure 3.4 is ($m = 8, k_\| = 7.85$):

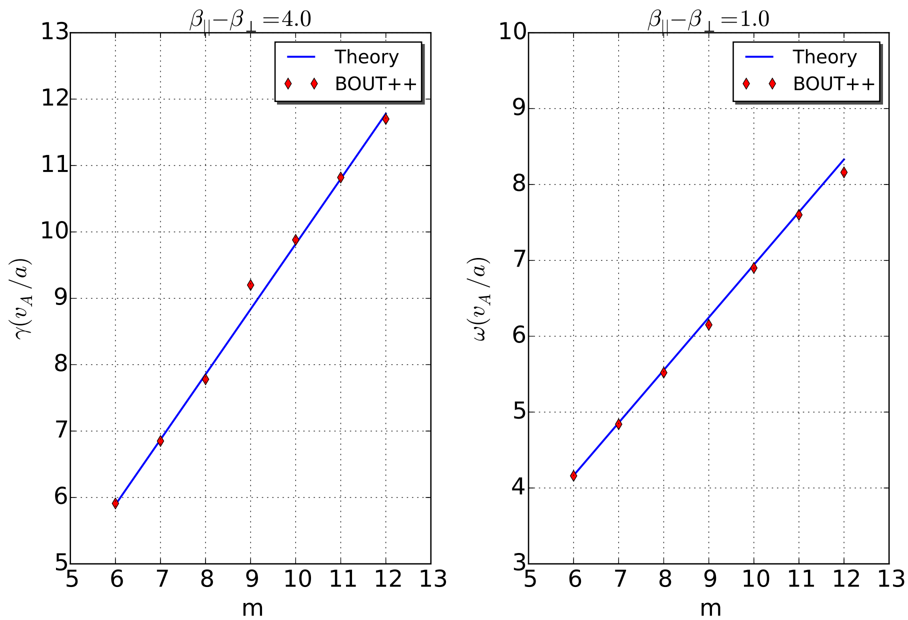

Figure 3.3: Figure on the left shows comparison of firehose growth rate, the analytical function of blue line is $\gamma = k_{\|} = 2\pi m/L_y$; Figure on the right shwos comparison of frequency, the analytical function is $\omega = k_{\|}/\sqrt{2} = \sqrt{2}\pi m/L_y$

$\beta_{\|} - \beta_{\perp}$	3	4	5	6	7	8
γ_{the}	5.55	7.85	9.62	11.11	12.42	13.60
γ_{sim}	5.64	7.78	9.69	11.18	12.49	13.68

3.3 Kinetic Theory

Although double adiabatic MHD equations give a complete and comprehensive analysis on firehose instability induced by extreme anisotropy between parallel and perpendicular direction of magnetic field, those equations have yet a limited valid area. On the one hand, because of the quasi-neutrality

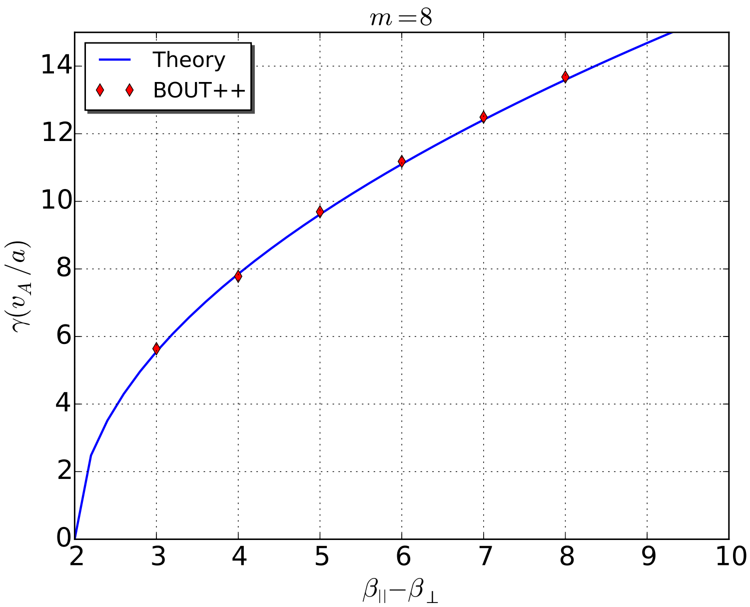

Figure 3.4: Analytical function for blue line is $\gamma = k_{\|}\sqrt{1-(\beta_{\|}-\beta_{\perp})/2}$

assumption made by original ideal MHD, double adiabatic MHD equations only work for slow fluctuations in plasmas. In other regions, where the fluctuation is so fast that electrons and ions have complete different behaviors for their large mass difference, we have to treat these species separately. For example, during impulsive solar flare, electrons are magnetized and can be accelerated along magnetic field by reconnections[13], while ions are too heavy to respond in short time scale that they need to be treated unmagnetized[4]. On the other hand, some kinetic effects, which didn't appear in MHD fluid

[4]Actually, solar flare is a quite complicated and not fully understood topic. Whether ions are accelerated during impulsive solar flare is questionable, but we will only consider electron fluctuations in the following.

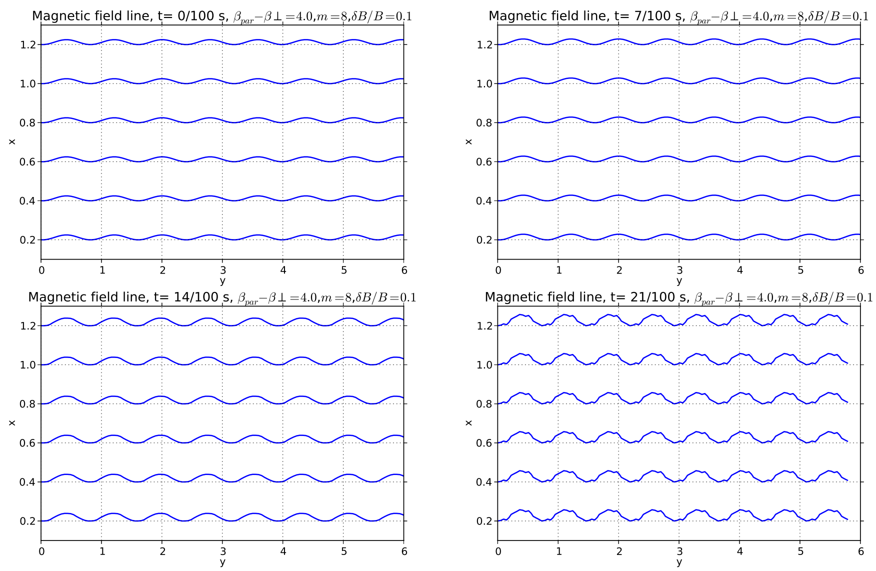

Figure 3.5: This figure shows the evolution of magnetic field through firehose instability in only linear stage. At initial moment, the perturbation is very small. Then the pressure anisotropy excites this mode to increase its ampilitude

equations, have a significant influences on waves in plasma, such as Landau Damping. To explore how these effects instabilities in plasmas, we have to go back to vlasov equations and study kinetic theory.

3.3.1 Linear derivation of firehose instaility dispersion

Starting from the famous Vlasov equation for electrons:

$$\frac{\partial f}{\partial t} + \boldsymbol{v} \cdot \nabla f + q\frac{\boldsymbol{E} + \boldsymbol{v} \times \boldsymbol{B}}{m} \cdot \nabla_{\boldsymbol{v}} f = 0 \tag{3.30}$$

In order to compare the final results, here we use the same equilibrium as (3.15), for linear part:

$$\boldsymbol{B} = \boldsymbol{B}_0 + \delta\boldsymbol{B},\ \boldsymbol{E} = \delta\boldsymbol{E},\ f(\boldsymbol{x}, \boldsymbol{v}, t) = F(\boldsymbol{v}) + \delta f(\boldsymbol{x}, \boldsymbol{v}, t). \tag{3.31}$$

where $F(\boldsymbol{v})$ is equilibrium distribution function, which later is assumed as binormal function. Apply this relation to equation (3.30) and only keep the first order term, we get linearized vlasov equation:

$$\left(\frac{\partial}{\partial t} + \boldsymbol{v} \cdot \nabla + \frac{q}{m}\boldsymbol{v} \times \boldsymbol{B}_0 \cdot \frac{\partial}{\partial \boldsymbol{v}}\right) \delta f(\boldsymbol{x}, \boldsymbol{v}, t) = -\frac{q}{m}(\delta\boldsymbol{E} + \boldsymbol{v} \times \delta\boldsymbol{B}) \cdot \frac{\partial F(\boldsymbol{v})}{\partial \boldsymbol{v}} \tag{3.32}$$

To study firehose instability, we let the fluctuating fields wary as $\exp(ik_\parallel z' - i\omega t')$, using green theorem:

$$\begin{aligned}\delta f(\boldsymbol{x}, \boldsymbol{v}, t) &= -\frac{q}{m\omega}\delta\boldsymbol{E} \cdot \int_{-\infty}^{t} dt' \exp(ik_\parallel z' - i\omega t') \left[\boldsymbol{I}(\omega - \boldsymbol{v'} \cdot \boldsymbol{k}) + \boldsymbol{v'}\boldsymbol{k}\right] \cdot \frac{\partial F(\boldsymbol{v'})}{\partial \boldsymbol{v'}} \\ &= -\frac{q}{m\omega}\int_{-\infty}^{t} dt' \exp(ik_\parallel z' - i\omega t') \left[(\omega - v'_z k_\parallel)\delta\boldsymbol{E} \cdot \frac{\partial F(\boldsymbol{v'})}{\partial \boldsymbol{v'}} + (\boldsymbol{v'} \cdot \delta\boldsymbol{E})k_\parallel \frac{\partial F(\boldsymbol{v'})}{\partial v'_z}\right].\end{aligned}$$

Assume that $\delta \boldsymbol{E} \perp \boldsymbol{z}$, we can simplify equation using identity $\dfrac{\partial}{\partial v'_x} = \dfrac{v'_x}{v_\perp}\dfrac{\partial}{\partial v_\perp}$:

$$\begin{aligned}
&(\omega - v'_z k_\parallel)\delta \boldsymbol{E} \cdot \frac{\partial F(\boldsymbol{v'})}{\partial \boldsymbol{v'}} + (\boldsymbol{v'} \cdot \delta \boldsymbol{E}) k_\parallel \frac{\partial F(\boldsymbol{v'})}{\partial v'_z} \\
&= (\omega - v'_z k_\parallel)(\delta E_x \frac{\partial F}{\partial v'_x} + \delta E_y \frac{\partial F}{\partial v'_y}) + (v'_x \delta E_x + V'_y \delta E_y) k_\parallel \frac{\partial F}{\partial v'_z} \\
&= (\delta E_x v'_x + \delta E_y v'_y)\left[(\omega - v'_z k_\parallel)\frac{1}{v_\perp}\frac{\partial F}{\partial v_\perp} + k_\parallel \frac{\partial F}{\partial v'_z}\right] \\
&= (\delta E_x v'_x + \delta E_y v'_y)\frac{1}{v_\perp}\widehat{D}_k F
\end{aligned} \tag{3.33}$$

The unperturbed gyro-orbits identities we need are:

$$\tau = t - t' \tag{3.34}$$

$$v_x = v_\perp \cos\phi \tag{3.35}$$

$$v_y = v_\perp \sin\phi \tag{3.36}$$

$$v'_x = v_\perp \cos(\phi + \Omega\tau) \tag{3.37}$$

$$v'_y = v_\perp \sin(\phi + \Omega\tau) \tag{3.38}$$

$$v'_z = v_\parallel \tag{3.39}$$

$$z' = z - v_\parallel \tau. \tag{3.40}$$

According to (3.34), $k_\parallel z' - \omega t' = k_\parallel z - \omega t + (\omega - k_\parallel v_z)\tau$, therefore, we get final expression for $\delta f(\boldsymbol{x}, \boldsymbol{v}, t)$:

$$\delta f(\boldsymbol{x}, \boldsymbol{v}, t) = -\frac{q}{m\omega}\int_0^{+\infty} d\tau e^{i(\omega - k_\parallel v_z)\tau}(\delta E_x v'_x + \delta E_y v'_y)\frac{1}{v_\perp}\widehat{D}_k F \tag{3.41}$$

Now, we need to calculate the fluctuating plasma current $(\delta \boldsymbol{j_x}, \delta \boldsymbol{j_y})$perpendicular to magnetic field. For the simplicity, we assume that ions are cold and immobile $(v_\parallel = v_z)$

$$\begin{aligned}
&\delta j_x = q \int d^3 v v_x \delta f(\boldsymbol{x}, \boldsymbol{v}, t) \\
&= -\frac{q^2}{m\omega} \int_0^{+\infty} \int_{-\infty}^{+\infty} \int_0^{2\pi} v_\perp dv_\perp dv_\parallel d\phi \int_0^{+\infty} d\tau e^{i(\omega - k_\parallel v_\parallel)\tau} v_\perp \cos\phi \\
&\times \widehat{D}_k F \left[\delta E_x \cos(\phi + \Omega\tau) + \delta E_y \sin(\phi + \Omega\tau)\right]
\end{aligned} \tag{3.42}$$

Recall the identities: $\cos\phi\cos(\phi + \Omega\tau) = \frac{1}{2}\cos(2\phi + \Omega\tau) + \frac{1}{2}\cos\Omega\tau$ and $\cos\phi\sin(\phi + \Omega\tau) = \frac{1}{2}\sin(2\phi + \Omega\tau) + \frac{1}{2}\sin\Omega\tau$, we can first solve the integrals of $d\phi$ and $d\tau$:

$$\begin{aligned}
&\int_0^{+\infty} \int_0^{2\pi} d\phi d\tau e^{i(\omega - k_\parallel v_\parallel)\tau} \left[\delta E_x \cos\phi\cos(\phi + \Omega\tau) + \delta E_y \cos\phi\sin(\phi + \Omega\tau)\right] \\
&= \frac{\pi}{2} \int_0^{+\infty} d\tau e^{i(\omega - k_\parallel v_\parallel)\tau} \left[\delta E_x (e^{i\Omega\tau} + e^{-i\Omega\tau}) - i\delta E_y (e^{i\Omega\tau} - e^{-i\Omega\tau})\right]
\end{aligned} \tag{3.43}$$

One important integral identity we need to know about this question is: $\int_0^{+\infty} e^{ikx} dx = \frac{i}{k}$, if $\Im[k] > 0$. Assume that all the fluctuations go unstable, we get the expression of δj_x:

$$\delta j_x = -\frac{q^2}{m\omega}\frac{\pi}{2} \int_0^{+\infty} \int_{-\infty}^{+\infty} v_\perp^2 dv_\perp dv_\parallel \sum_{n=\pm 1} \frac{\widehat{D}_k F}{\omega - k_\parallel v_\parallel + n\Omega} (i\delta E_x + n\delta E_y) \tag{3.44}$$

By similar calculation:

$$\delta j_y = -\frac{q^2}{m\omega}\frac{\pi}{2} \int_0^{+\infty} \int_{-\infty}^{+\infty} v_\perp^2 dv_\perp dv_\parallel \sum_{n=\pm 1} \frac{\widehat{D}_k F}{\omega - k_\parallel v_\parallel + n\Omega} (-n\delta E_x + i\delta E_y) \tag{3.45}$$

Ohm's Law shows that $\boldsymbol{j} = \boldsymbol{\Sigma} \cdot \boldsymbol{E}$, from δj_x and δj_y we calculated above, the electric conductivity:

$$\boldsymbol{\Sigma} = -\frac{q^2}{m\omega}\frac{\pi}{2}\int_0^{+\infty}\int_{-\infty}^{+\infty} v_\perp^2 dv_\perp dv_\parallel \sum_{n=\pm 1}\frac{\widehat{D}_k F}{\omega - k_\parallel v_\parallel + n\Omega}$$
$$\times \begin{pmatrix} i & n \\ -n & i \end{pmatrix}. \tag{3.46}$$

Notice that the sum over $n = \pm 1$ means that parallel propagating electromagnetic waves can be separated into right-hand ($n = 1$) and left-hand ($n = -1$) circularly polarized waves. We will only focus on right-hand circularly polarized wave in this question. According to section 11.2, the requirements for self-consistent fields are:

$$\left[\left(k^2 - \frac{\omega^2}{c^2}\right)\boldsymbol{I} - \boldsymbol{kk} - i\omega\mu_0\boldsymbol{\Sigma}\right] \cdot \boldsymbol{E} = 0 \tag{3.47}$$

Plug in electric conductivity $\boldsymbol{\Sigma}$ above, we get the expression for dispersion relation:

$$D(\boldsymbol{k}, \omega) = \det\begin{pmatrix} {k_\parallel}^2 - \frac{\omega^2}{c^2} - i\omega\mu_0\Sigma_{xx} & -i\omega\mu_0\Sigma_{xy} \\ -i\omega\mu_0\Sigma_{yx} & {k_\parallel}^2 - \frac{\omega^2}{c^2} - i\omega\mu_0\Sigma_{yy} \end{pmatrix} = 0 \tag{3.48}$$

Now, in order to calculate dispersion relation explicitly, we need to work on $\boldsymbol{\Sigma}$ part. As $\Sigma_{xx} = \Sigma_{yy} = i\Sigma_{xy} = -i\Sigma_{yx}$, we only need to solve for one component of $\boldsymbol{\Sigma}$. Given the distribution function of anisotropic plasma: $F\left(v_\perp, v_\parallel\right) = \frac{1}{2\pi^{\frac{3}{2}}}\frac{1}{v_{T\parallel}}\frac{1}{v_{T\perp}^2}\exp\left(-\frac{v_\perp^2}{2v_{T\perp}^2}\right)\exp\left(-\frac{v_\parallel^2}{2v_{T\parallel}^2}\right)$, in which $v_{T\parallel} = \sqrt{T_\parallel/m}$ and $v_{T\perp} = \sqrt{T_\perp/m}$. we can get expression for $\widehat{D_k}F$:

$$\widehat{D}_k F = k_z v_\perp \frac{\partial F}{\partial v_z} + (\omega - k_z v_z)\frac{\partial F}{\partial v_\perp} \tag{3.49}$$

$$\frac{\partial F}{\partial v_z} = \frac{1}{2\pi^{\frac{3}{2}}} \frac{1}{v_{T\|}} \frac{1}{v_{T\perp}^2} \frac{-v_z}{v_{T\|}^2} \exp\left(-\frac{v_\perp^2}{2v_{T\perp}^2}\right) \exp\left(-\frac{v_\|^2}{2v_{T\|}^2}\right) \tag{3.50}$$

$$\frac{\partial F}{\partial v_\perp} = \frac{1}{2\pi^{\frac{3}{2}}} \frac{1}{v_{T\|}} \frac{1}{v_{T\perp}^2} \frac{-v_\perp}{v_{T\perp}^2} \exp\left(-\frac{v_\perp^2}{2v_{T\perp}^2}\right) \exp\left(-\frac{v_\|^2}{2v_{T\|}^2}\right). \tag{3.51}$$

Recall the plasma dispersion function:$Z(\zeta) = \frac{1}{\sqrt{\pi}} \int_{-\infty}^{+\infty} \frac{dt \exp(-t^2)}{t - \zeta}$, the integration over all parallel velocities of the response function gives $\left(\alpha = (\omega + \Omega)/k_\| \sqrt{\frac{2T_\|}{m}}\right)$

$$\begin{aligned} &\frac{1}{\sqrt{2\pi}} \int dv_\| \frac{k_\| v_\|}{\omega - k_\| v_\| + n\Omega} \frac{1}{v_{T\|}} \frac{1}{v_{T\|}^2} \exp -\frac{v_\|^2}{2v_{T\|}^2} \\ &= -\frac{1}{v_{T\|}^2} (1 + \alpha Z(\alpha)) \end{aligned} \tag{3.52}$$

$$\begin{aligned} &\frac{1}{\sqrt{2\pi}} \int dv_\| \frac{\omega - k_\| v_\|}{\omega - k_\| v_\| + n\Omega} \frac{1}{v_{T\|}} \exp -\frac{v_\|^2}{2v_{T\|}^2} \\ &= 1 + \frac{n\Omega}{\sqrt{2} k_\| v_{T\|}} Z(\alpha) \end{aligned} \tag{3.53}$$

Now, we can calculated the component of electric conductivity Σ_{xy}

$$\begin{aligned} \Sigma_{xy} &= -\frac{q^2}{m\omega} \frac{\pi}{2} \int_0^{+\infty} \int_{-\infty}^{+\infty} v_\perp^2 dv_\perp dv_\| \frac{\widehat{D}_k F}{\omega - k_\| v_\| + \Omega} \\ &= -\frac{q^2}{2m\omega} \frac{v_{T\perp}^2}{v_{T\|}^2} (1 + \alpha Z(\alpha)) + \frac{q^2}{2m\omega} (1 + \frac{\Omega}{k\| \sqrt{\frac{2T_\|}{m}}} Z(\alpha)) \\ &= \frac{q^2}{2m\omega} \left[\left(1 - \frac{T_\perp}{T_\|}\right) (1 + \alpha Z(\alpha)) - \frac{\omega}{k_\| \sqrt{\frac{2T_\|}{m}}} Z(\alpha) \right] \end{aligned} \tag{3.54}$$

Finally, according to (3.48), we get the dispersion relation for right-hand circularly polarized electromagnetic waves along magnetic field in anisotropic plasma

$$\frac{k_\parallel^2 c^2}{\omega^2} = 1 - \frac{2c^2\mu_0\Sigma_{xy}}{\omega}$$
$$= 1 - \frac{\omega_{pe}^2}{\omega^2}\left[\left(1 - \frac{T_\perp}{T_\parallel}\right)(1+\alpha Z(\alpha)) - \frac{\omega}{k_\parallel\sqrt{\frac{2T_\parallel}{m}}} Z(\alpha)\right] \tag{3.55}$$

, in which $\alpha = (\omega + \Omega)/k_\parallel\sqrt{\dfrac{2T_\parallel}{m}}$

3.3.2 Analysis and comparison

Lots of works has been done in analyzing dispersion relation (3.55)[82] in detail. Here crude calculation will be used to show reasonable results. We assume that electron temperature is relatively low, so that $\alpha \gg 1$. We can also assume that the frequency of fluctuation is not so high that $\omega \ll \Omega$. $Z(\alpha)$ can be expanded as:

$$Z(\alpha) \approx -\frac{1}{\alpha} - \frac{1}{2\alpha^3} \tag{3.56}$$

Apply this to dispersion equation:

$$\omega^2 = k_\parallel^2 c^2 - \frac{\omega_{pe}^2}{2\alpha^2}\left(1 - \frac{T_\perp}{T_\parallel}\right) \tag{3.57}$$

Through the similar calculation as we did before, the criterion for firehose instability is $\omega^2 < 0$, that is

$$T_\parallel - T_\perp > \frac{2\alpha^2 k_\parallel^2 c^2}{\omega_{pe}^2} T_\parallel \tag{3.58}$$

which is consistent with the one we got from MHD ($\dfrac{p_{\parallel 0}}{\rho_0} - \dfrac{p_{\perp 0}}{\rho_0} > v_A^2$).

Chapter 4

Impurity Transport

The transport of the impurities induced by the gradient driven drift-wave turbulences has been started as early as 1970s, where when Cohen *et al* compared the experimental and numerical results of the transport of Aluminum[6]. Later, the experiment observations in many fusion devices confirmed that the impurities at the core region are harmful to the confinement[55, 34, 43, 93, 22]. The earlier investigations show that these inward impurity flux can not be fully understood in the neoclassic regime, for the diffusivity predicted by the neoclassic analysis are at least one order of magnitude smaller than the experimental measurements[21]. Therefore, more and more efforts have been devoted to the anomalous transport induced by the turbulence, especially the drift-wave turbulence, such as ITG and TEM. Numerous studies have been conducted on many fusion devices using various physical models, for example, the gyrokinetic analysis[43, 44, 81, 3] and the fluid analysis[14, 26, 25, 24].

In this chapter, we present the linear theoretical studies of the density gradient driven drift-waves (Hasegawa-Wakatani model) with the presence of active impurities. The convective diffusivity is calculated for tokamak, reversed-field pinch (Madison Symmetric Torus) and stellarator (Large Helical Device) and the results are compared with the gyrokinetic studies in reference[44].

4.1 Hasegawa-Wakatani drift model with impurities

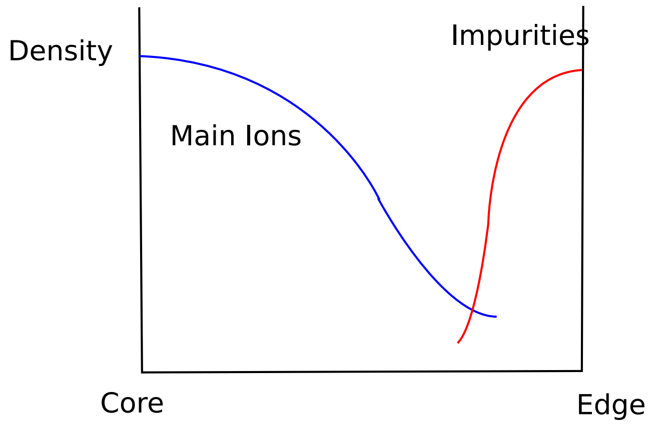

Figure 4.1: Density gradient direction of main ions and impurities in fusion reactor are opposite in most cases. As impurities are scraped off from vessel, their density gradient are larger than main ion's.

As main ions in fusion reactor usually localize at core while impurities concentrate near the edge, their density gradient are opposite. Drift waves driven by impurity and ion gradient will result in turbulent transport ($E \times B$). We use Hasegawa-Wakatani drift model, and consider impurities as the second ion with charge Z and mass A. Parameters of ion, impurity and electron are represented by subscript i, z,and e. In order to simplify the calculation, some approximations without loss of generality are made. First, Quasi-neutrality is satisfied by ion, impurity and electrons. This statement includes both the equilibrium background, where $\frac{n_{i0}}{L_{n_i}} + Z\frac{n_{z0}}{L_{n_z}} = \frac{n_{e0}}{L_{n_e}}$, and the fluctuation part, $Z\delta n_z + \delta n_i = \delta n_e$. Secondly, ion temperature gradient effects will not be considered in this calculation, they will be treated as seperate work in the future. Therefore, T_i, T_e, T_z are constants. Finally, Quasi-linear approach is used in calculation. From ion momentum equation, we get

$$\frac{\partial \delta n_i}{\partial t} + \nabla_\perp \cdot (n_i(\boldsymbol{v_E} + \boldsymbol{v_{di}} + \boldsymbol{v_{\pi i}} + \boldsymbol{v_{pi}})) = 0 \tag{4.1}$$

where,

$$\boldsymbol{v_E} = \frac{\boldsymbol{b} \times \nabla \phi}{B} \tag{4.2}$$

$$\boldsymbol{v_{di}} = \frac{\boldsymbol{b} \times \nabla P_i}{e n_i B} \tag{4.3}$$

$$\boldsymbol{v_{\pi i}} = \frac{\boldsymbol{b} \times \nabla \cdot \boldsymbol{\pi_i}}{e n_i B} \tag{4.4}$$

$$\boldsymbol{v_{pi}} = \frac{m_i}{eB} \boldsymbol{b} \times \frac{d\boldsymbol{v_i}}{dt} \tag{4.5}$$

Pressure tensor π_i need to be treated with extra care. Commonly we assume that it includes three parts,

$$\boldsymbol{\pi_i} = \boldsymbol{\pi_{FLR}} + \boldsymbol{\pi_{shear}} + \boldsymbol{\pi_{comp}} \tag{4.6}$$

where the first term represents Finite Larmor Radius (FLR) effects, which is collisionless term. The famous FLR cancellation shows that $m_i n_i \frac{d\boldsymbol{v_{di}}}{dt} + \nabla \cdot \boldsymbol{\pi_{FLR}} = \nabla \chi$. The second term represents shear force, and can be easily written as $\boldsymbol{\pi_{shear}} = -\eta_i \nabla \boldsymbol{v}$, $\eta_i = \frac{3 n_i T_i}{10 \omega_{ci}^2 \tau_i}$. The last term is usually ignored in isotropic plasma. Similar treatment is applied to impurity equations. However, for electrons, parallel motion need to be taken into account.

$$0 \approx -\nabla_\parallel P_e + e n_e \nabla_\parallel \phi - m_e n_e \nu_{ei} v_\parallel \tag{4.7}$$

and electron continuity equation is:

$$\frac{\partial \delta n_e}{\partial t} + \nabla_\perp \cdot (n_e(\boldsymbol{v_E} + \boldsymbol{v_{di}})) + \nabla_\parallel (n_e v_\parallel) = 0 \tag{4.8}$$

Normalization parameters are:

$$\tilde{t} = t\omega_{ci}, \tilde{l} = l/\rho_s, \tilde{n_s} = \delta n_s/n_{s0}, \tilde{\phi} = e\phi/T_e, \rho_s = c_s/\omega_{ci}, c_s = \sqrt{T_e/m_i} \tag{4.9}$$

4.1.1 Slab Geometry

First, simply slab geometry is considered. In slab geometry, $\boldsymbol{b} = \boldsymbol{e_z}$, no magnetic gradient and curvature effects are included. Density gradient is along x direction. Then,

$$\nabla \cdot \boldsymbol{v_E} \approx 0, \nabla \cdot (n_i \boldsymbol{v_{di}}) \approx 0 \tag{4.10}$$

Then the quasi-linear fluid equations are (from now, n_s represents fluctuation part instead of δn_s):

$$\frac{\partial n_i}{\partial t} + \frac{\rho_s}{L_{ni}} \frac{\partial \phi}{\partial y} + [\phi, n_i] - \frac{d}{dt} \nabla_\perp^2 \phi + \mu_i \nabla_\perp^4 \phi = 0 \tag{4.11}$$

$$\frac{\partial n_z}{\partial t} + \frac{\rho_s}{L_{nz}} \frac{\partial \phi}{\partial y} + [\phi, n_z] - \frac{A}{Z} \frac{d}{dt} \nabla_\perp^2 \phi + \frac{A}{Z} \mu_z \nabla_\perp^4 \phi = 0 \tag{4.12}$$

$$\frac{\partial n_e}{\partial t} + \frac{\rho_s}{L_{ne}} \frac{\partial \phi}{\partial y} + [\phi, n_e] + \frac{m_i}{m_e} \frac{\omega_{ci}}{\nu_{ei}} \nabla_\parallel^2 (\phi - n_e) = 0 \tag{4.13}$$

As $\rho_s/L_n \ll 1$ in drift order, another normalization need to be made to balance equations.

$$\bar{t} = \tilde{t} \frac{\rho_s}{L_{ne}}, \{\bar{\phi}, \bar{n_s}\, \bar{\nabla}_\parallel\} = \{\tilde{\phi}, \tilde{n_s}, \tilde{\nabla}_\parallel\} \frac{L_{ne}}{\rho_s} \tag{4.14}$$

With this new normalization, we can get the dispersion relation.(unfinished)

4.1.2 Tokamak Geometry

Toroidal orthogonal coordinates and field-aligned coordinates are two most commonly used coordinate systems to study Tokamak magnetic field. Basically, field-aligned coordinates are more accurate and widely used in fluid and gyro-kinetic simulations. However, as field-aligned coordinates are non-orthogonal, it is very difficult to be used in linear analysis. We will use toroidal orthogonal coordinates in this section.

Toroidal orthogonal coordinates treat poloidal cross section as a circle, which is not the case in most Tokamak. However, when aspect ratio $a/R \ll 1$, the shape of poloidal cross section is less important. The properties of toroidal orthogonal coordinates $(r, \theta, \varphi)$are (x, y, z are cartesian coordinates):

$$x = (R + r\cos\theta)\cos\varphi$$

$$y = -(R + r\cos\theta)\sin\varphi$$

$$z = r\sin\theta$$

in which, R and a are the major radius and minor radius. For orthogonal coordinate system, we can calculate Lame coffecients,

$$h_r = 1, h_\theta = r, h_\varphi = R + r\cos\theta \tag{4.15}$$

The magnetic field can be written in this coordinate system as

$$\boldsymbol{B} = B_t\boldsymbol{e_\varphi} + B_p\boldsymbol{e_\theta} \approx \frac{B_0}{1+\varepsilon\cos\theta}\boldsymbol{e_\varphi} + \frac{B_0\varepsilon}{q}\boldsymbol{e_\theta} \tag{4.16}$$

where B_0 is magnititude of magnetic axis, $\varepsilon = r/R$, and $q = rB_t/RB_p$ is safety factor. Then the properties of magnetic field is:

$$B \approx \alpha B_0, \boldsymbol{b} = \frac{1}{\alpha}\left(\boldsymbol{e_\varphi} + \frac{\varepsilon}{q}\boldsymbol{e_\theta}\right), \nabla \times \boldsymbol{B} = B_0 \frac{2 - \alpha\widehat{s}}{Rq}\boldsymbol{e_\varphi} \tag{4.17}$$

in which magnetic shear is defined as:

$$\widehat{s} = \frac{r}{q\alpha}\frac{dq}{dr}, \ \ \alpha = \sqrt{1 + \frac{r^2}{q^2R^2}} \tag{4.18}$$

Therefore, equations (4.10) under slab approximation are not vaild in Tokamak geometry. Several terms in continuity equation (4.1) need to be modified (y and z are arc length in poloidal and toroidal direction, $dy = rd\theta$, $dz = (R + r\cos\theta)d\varphi$):

$$\begin{aligned} \boldsymbol{v_E} \cdot \nabla n_{i0} \quad &= \left(\frac{1}{B\alpha}\left(\boldsymbol{e_\varphi} + \frac{\varepsilon}{q}\boldsymbol{e_\theta}\right) \times \nabla\phi\right) \cdot \frac{dn_{i0}}{dr}\boldsymbol{e_r} \\ &= -\frac{1}{B\alpha}\frac{dn_{i0}}{dr}\left(\frac{\partial\phi}{\partial y} + \frac{\varepsilon}{q}\frac{\partial\phi}{\partial z}\right) \end{aligned} \tag{4.19}$$

$$\begin{aligned} \nabla \cdot \boldsymbol{v_E} \quad &= \nabla\left(\frac{1}{B^2}\right) \cdot (\boldsymbol{B} \times \nabla\phi) + \frac{1}{B^2}\nabla \cdot (\boldsymbol{B} \times \nabla\phi) \\ &= -2\frac{\nabla B}{B^3} \cdot (\boldsymbol{B} \times \nabla\phi) + \frac{1}{B^2}\nabla\phi \cdot (\nabla \times \boldsymbol{B}) \\ &= -\frac{2}{\alpha B}\frac{d\alpha}{dr}\left(-\frac{\partial\phi}{\partial y} + \frac{\varepsilon}{q}\frac{\partial\phi}{\partial z}\right) + \frac{1}{B^2}\frac{\partial\phi}{\partial z}\frac{B_0}{qR}(2 - \alpha\widehat{s}) \end{aligned} \tag{4.20}$$

$$\begin{aligned} \nabla \cdot (n\boldsymbol{v_{di}}) \quad &= -2\frac{\nabla B}{eB^3} \cdot (\boldsymbol{B} \times \nabla P_i) + \frac{1}{eB^2}\nabla P_i \cdot (\nabla \times \boldsymbol{B}) \\ &= -2\frac{T_iB_0}{eB^2}\frac{d\alpha}{dr}\left(-\frac{\partial n_i}{\partial y} + \frac{\varepsilon}{q}\frac{\partial n_i}{\partial z}\right) + \frac{T_i}{eB^2}\frac{\partial n_i}{\partial z}\frac{B_0}{qR}(2 - \alpha\widehat{s}) \end{aligned} \tag{4.21}$$

in which, ideal gas assumption is made, $P_i = n_i T_i$. Put these terms into ion continuity equation (4.1), we get the normalized ((4.9) and (4.14), excluding $\nabla_\parallel$) linear equation

$$\begin{aligned}&\frac{\partial n_i}{\partial t}+\frac{L_{ei}}{\alpha}\left(\frac{\partial\phi}{\partial y}-\frac{\varepsilon}{q}\frac{\partial\phi}{\partial z}\right)-\frac{L_{ne}}{L_B}2\frac{\partial\phi}{\partial y}+Q\frac{\partial\phi}{\partial z}\\&-\frac{2}{\tau_i}\frac{L_{ne}}{L_B}\frac{\partial n_i}{\partial y}+\frac{Q}{\tau_i}\frac{\partial n_i}{\partial z}-\frac{\partial}{\partial t}\nabla_\perp^2\phi+\mu_i\nabla_\perp^4\phi=0\end{aligned}\tag{4.22}$$

similarly, we can get linear equations for impurities and electrons

$$\begin{aligned}&\frac{\partial n_z}{\partial t}+\frac{L_{ez}}{\alpha}\left(\frac{\partial\phi}{\partial y}-\frac{\varepsilon}{q}\frac{\partial\phi}{\partial z}\right)-\frac{L_{ne}}{L_B}2\frac{\partial\phi}{\partial y}+Q\frac{\partial\phi}{\partial z}\\&-\frac{2}{Z\tau_z}\frac{L_{ne}}{L_B}\frac{\partial n_z}{\partial y}+\frac{Q}{Z\tau_z}\frac{\partial n_z}{\partial z}-\frac{A}{Z}\frac{\partial}{\partial t}\nabla_\perp^2\phi+\frac{A}{Z}\mu_z\nabla_\perp^4\phi=0\end{aligned}\tag{4.23}$$

$$\begin{aligned}&\frac{\partial n_e}{\partial t}+\frac{1}{\alpha}\left(\frac{\partial\phi}{\partial y}-\frac{\varepsilon}{q}\frac{\partial\phi}{\partial z}\right)-\frac{L_{ne}}{L_B}2\frac{\partial\phi}{\partial y}+Q\frac{\partial\phi}{\partial z}\\&+2\frac{L_{ne}}{L_B}\frac{\partial n_e}{\partial y}-Q\frac{\partial n_e}{\partial z}+\nu\nabla_\parallel^2(\phi-n_e)=0\end{aligned}\tag{4.24}$$

and the quasi-neutrality equation is

$$(1-f_z)n_i+f_z n_z-n_e=0\tag{4.25}$$

The parameters used in these equations are

$$\begin{aligned}&L_n=-n_0/\left(\frac{dn_0}{dr}\right),L_B=-B_0/\left(\frac{dB_0}{dr}\right)=-\alpha/\left(\frac{d\alpha}{dr}\right)\\&\frac{L_{ne}}{L_B}=\frac{\varepsilon_n}{\varepsilon_B},\varepsilon_n=\frac{L_{ne}}{R},\varepsilon_B=\frac{L_B}{R}\\&L_{ei}=\frac{L_{ne}}{L_{ni}},L_{ez}=\frac{L_{ne}}{L_{nz}},L_{ei}=\frac{1-f_zL_{ez}}{1-f_z},\tau_i=\frac{T_e}{T_i},\tau_z=\frac{T_e}{T_z},f_z=\frac{Zn_{z0}}{n_{e0}}\\&Q=\frac{2-\alpha\widehat{s}}{\alpha q}\varepsilon_n+\frac{2\varepsilon}{q}\frac{L_{ne}}{L_B},\nu=\frac{m_i}{m_e}\frac{\omega_{ci}}{\nu_{ei}}\frac{L_{ne}}{\rho_s},\mu_i=\frac{0.3}{\tau_i}\frac{L_{ne}\nu_{ii}}{c_s},\mu_z=\frac{0.3A}{\tau_z}\frac{L_{ne}\nu_{zi}}{c_s}\end{aligned}\tag{4.26}$$

Assume that $\{n_i, n_z, n_e, \phi\} \propto \exp -i\omega t + ik_\theta y + ik_\varphi z$, we can write equations (4.23) to (4.25) in matrix form,

$$\boldsymbol{A} \cdot \boldsymbol{\Phi} = 0, \boldsymbol{A} = \{a_{ij}\}, \boldsymbol{\Phi} = (n_i, n_z, n_e, \phi)^T \tag{4.27}$$

where the non-zero components a_{ij} are

$$\begin{aligned}
a_{11} &= -i\omega - \frac{2}{\tau_i}\frac{\varepsilon_n}{\varepsilon_B} ik_\theta + \frac{Q}{\tau_i} ik_\varphi \\
a_{14} &= \frac{L_{ei}}{\alpha}\left(ik_\theta - \frac{\varepsilon}{q} ik_\varphi\right) - 2\frac{\varepsilon_n}{\varepsilon_B} ik_\theta + iQk_\varphi - i\omega k_\perp^2 \\
a_{22} &= -i\omega - \frac{2}{Z\tau_z}\frac{\varepsilon_n}{\varepsilon_B} ik_\theta + \frac{Q}{Z\tau_z} ik_\varphi \\
a_{24} &= \frac{L_{ez}}{\alpha}\left(ik_\theta - \frac{\varepsilon}{q} ik_\varphi\right) - 2\frac{\varepsilon_n}{\varepsilon_B} ik_\theta + iQk_\varphi - \frac{A}{Z} i\omega k_\perp^2 \\
a_{33} &= -i\omega + 2\frac{\varepsilon_n}{\varepsilon_B} ik_\theta - iQk_\varphi + \nu k_\parallel^2 \\
a_{34} &= \frac{1}{\alpha}\left(ik_\theta - \frac{\varepsilon}{q} ik_\varphi\right) - 2\frac{\varepsilon_n}{\varepsilon_B} ik_\theta + iQk_\varphi - \nu k_\parallel^2 \\
a_{41} &= 1 - f_z, a_{42} = f_z, a_{43} = -1.0
\end{aligned} \tag{4.28}$$

where,

$$k_\parallel = \boldsymbol{k} \cdot \boldsymbol{b} = \frac{1}{\alpha}\left(k_\varphi + \frac{\varepsilon}{q} k_\theta\right), k_\perp^2 = \frac{1}{\alpha^2}\left(k_\theta^2 + \left(\frac{\varepsilon}{q}\right)^2 k_\varphi^2\right) \tag{4.29}$$

Therefore, dispersion relation can be obtained by calculate $\mathbf{det}(\boldsymbol{A}) = 0$, let $\omega = \omega_r + i\gamma$. Here we take the Madison Symmetric Torus(MST), a reversed-field pinch as an example to illustrate growth rate and frequency dependences on different parameters. MST is a type of Tokamak with reversed toroidal magnetic field close to the edge, therefore, safety factor q reverses its sign along r direction[4, 9]. Also, in contrast to other Tokamaks, the magnitude of poloidal and toroidal magnetic field is comparable, which leads to $q \ll 1$ at core. Typical parameters[44] of the MST are $q = 0.15, \widehat{s} = -1.0, \tau_i = \tau_z = 1.33, k_\theta = 0.447, \varepsilon = 0.2, \varepsilon_n = 0.15, \varepsilon_B = 0.6, f_z = 0.1, L_{ez} = -10$, unless otherwise stated. Impurity ions Li+3, B+5, C+6, O+8 and Ni+18 are considered. First, L_{ez} effects are explored. The growing mode decreases as L_{ez} increases from nergative value (Figure 4.2), which agrees with linear kinetic model. However, two discrepancies have been shown in the plot. The first one is that the growth rate calculated by fluid model is nearly one order larger than kinetic theory, which is due to the lack of Landau damping. The second one is that the growing mode is not stabilized until $L_{ez} > 0$, while it is stabilized at $L_{nz} \approx -3.5$ in kinetic model. One possible reason is that in kinetic model, all the toroidal mode number (k_φ) are taken into account, while only single toroidal mode are considered in fluid model. If this single toroidal mode is not close to the fastest growing mode, the result should be different.

From quasi-linear turbulent transport theory, particle flux in radial due to drift waves is expressed as

$$\Gamma_i = < \delta n_i v_{Ei} > = \Re\left[\sum_k \frac{ik_y\phi_k}{B}\delta n_i\right] = -\sum_k k_y\rho_s c_s n_i \left|\frac{e\phi_k}{T_e}\right|^2 \Im[X_1] \tag{4.30}$$

$$\Gamma_z = < \delta n_z v_{Ez} > = \Re\left[\sum_k \frac{ik_y\phi_k}{B}\delta n_z\right] = -\sum_k k_y\rho_s c_s n_z \left|\frac{e\phi_k}{T_e}\right|^2 \Im[X_2] \tag{4.31}$$

in which subscripts 'i' and 'z' represent ion and impurity flux respectively. Also, in terms of equation (4.29)

$$X_1 = (\frac{\delta n_i}{n_i})/(\frac{e\phi}{T_e}) = -a_{14}/a_{11}, X_2 = (\frac{\delta n_z}{n_i})/(\frac{e\phi}{T_e}) = -a_{24}/a_{22} \tag{4.32}$$

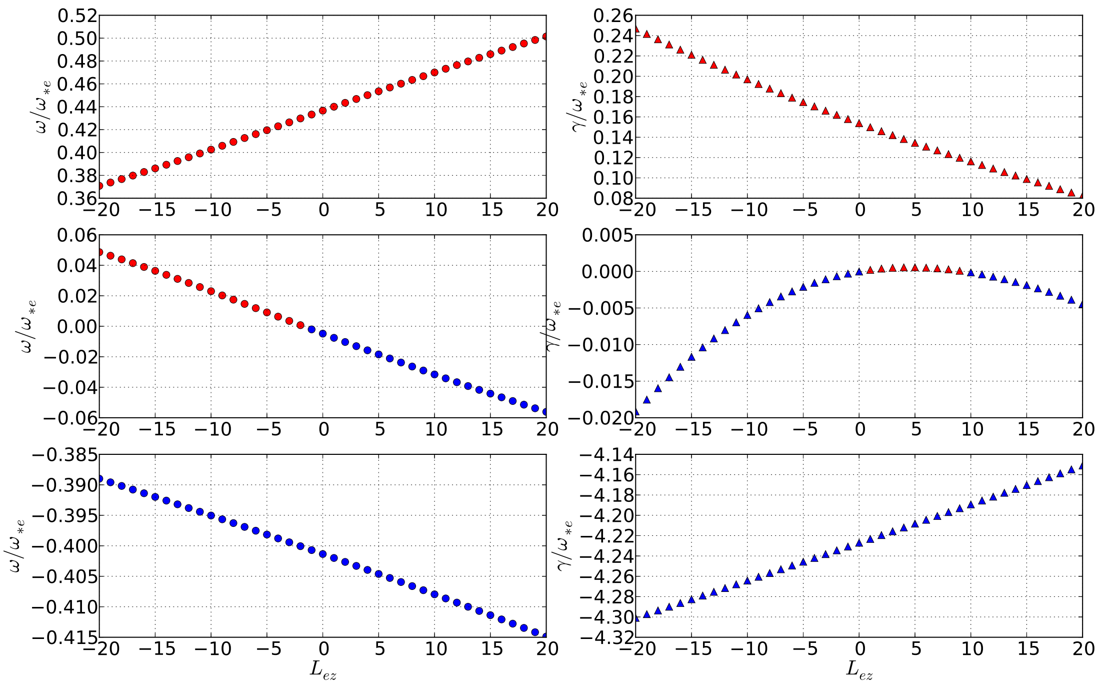

Figure 4.2: This plot shows frequency and growth rate of three modes. Fully ionized Boron B+5 is used as an example. $A = 11, B = 5, \nu = 1.0, k_\varphi = 0.0134$, where A and B represent the number of nuclei and lost electrons respectively.

Through some complicated yet straightforward algebra, we can get

$$\Im[X_2] = \Im[-\frac{a_{24}}{a_{22}}] = -\frac{\dfrac{L_{ez}}{\alpha}\gamma\left(k_\theta - \dfrac{\varepsilon}{q}k_\varphi\right) + \left(\dfrac{A}{Z^2\tau_z}k_\perp^2 - 1\right)\left(2\dfrac{\varepsilon_n}{\varepsilon_B}k_\theta - Qk_\varphi\right)}{\gamma^2 + (\omega_r + \dfrac{2\varepsilon_n}{Z\tau_z\varepsilon_B}k_\theta - \dfrac{Q}{Z\tau_z}k_\varphi)^2} \tag{4.33}$$

where $\omega = \omega_r + i\gamma$, ω_r and γ are the growing branch solution in dispersion relation (4.27). A phenomenological model for particle flux is usually expressed

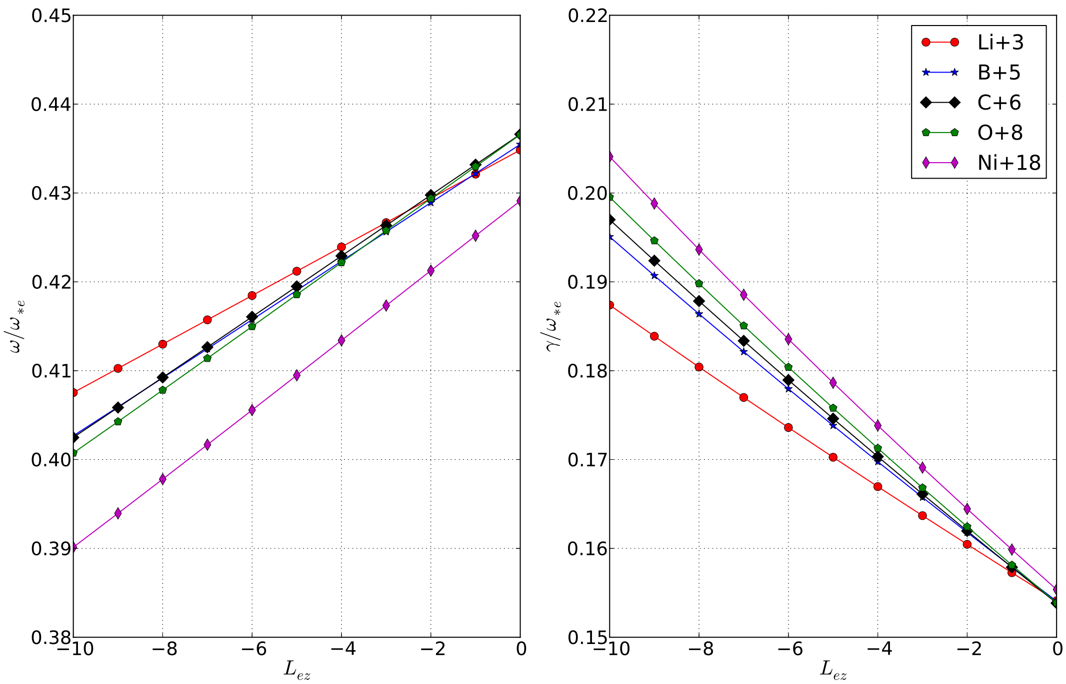

Figure 4.3: Growth rate and frequency of the growing mode, where fully ionized lithium,boron,carbon,oxygen and nickel with 18 ion charge numbers are considerd as impurity ions. Other parameters are the same as used in figure 4.2

as

$$\Gamma_z = -D_z \frac{\partial n_z}{\partial x} + V_z n_z \tag{4.34}$$

or

$$\Gamma_z / n_z = D_z / L_{nz} + V_z \tag{4.35}$$

in which D_z and V_z are the cofficients of diffusive and convective term.n_z is the background impurity density. Solving D_z and V_z from experimental or computational fluctuation results is considered as inverse problem and handful of algorithm have been developed to tackle this problem. However, for quasi-linear analysis in this paper, diffusive and convective term can be easily separated by checking the inclusion of density scale length L_{nz}. Based on this principle, the cofficients are

$$D_z = \sum_k k_y \rho_s c_s \frac{\frac{L_{ne}}{\alpha}\gamma\left(k_\theta - \frac{\varepsilon}{q}k_\varphi\right)}{\gamma^2 + (\omega_r + \frac{2\varepsilon_n}{Z\tau_z\varepsilon_B}k_\theta - \frac{Q}{Z\tau_z}k_\varphi)^2}\left|\frac{e\phi_k}{T_e}\right|^2 \tag{4.36}$$

$$V_z = \sum_k k_y \rho_s c_s \frac{\left(\frac{A}{Z^2\tau_z}k_\perp^2 - 1\right)\left(2\frac{\varepsilon_n}{\varepsilon_B}k_\theta - Qk_\varphi\right)}{\gamma^2 + (\omega_r + \frac{2\varepsilon_n}{Z\tau_z\varepsilon_B}k_\theta - \frac{Q}{Z\tau_z}k_\varphi)^2}\left|\frac{e\phi_k}{T_e}\right|^2 \tag{4.37}$$

Radial profile of D_z and V_z needs to be calculated and graphed.

4.1.3 Large Helical Device (Stellerator)

Different from the axisymmetric toroidal fusion device (Tokamak), the stellerator(LHD, Japan and Wendelstein 7-X, Germany)[36] is another promising design to reach magnetic confinement fusion. The most distinctive characteristic of the stellerator is that the nested magnetic surfaces inside separatrix can be realized solely by external coils. In other words, plasma current is not necessary as in Tokamak, which makes it possible to eliminate many types of instabilities induced by the toroidal plasma current, such as the sawtooth modes. However, the transport features of the impurities remain unclear. For example, promising outward convections of the impurities induced by the ion temperature gradient(ITG) turbulence are observed when the carbon impurities are injected to the core region[93]. The experimental measurements show that the core impurity density can be reduced to only 0.3% of the original density. This study again contradicts the neoclassic prediction in both transport direction and the amplitude. The numerical studies have been conducted on this topic on LHD and many important results have been obtained[81, 20].

As another side of the coin, the requirement that all the currents are produced by external coils yields a complex helical configuration, which make the theoretical study and simulations much more difficult than for Tokamaks, by advancing from 2-D to 3-D. Because of the non-axisymmetric properties, aspect ratio a/R varies in the toroidal direction and the analytical model seems inaccurate. The strange shape of magnetic surfaces make it difficult to implement field aligned coordinates theoretically. However, if aspect ratio $a/R \ll 1$ globally, poloidal cross section can still be treated as circular and crude orthogonal coordinates (ϕ, θ, φ) are appropriate to the first order of a/R.

As our main focus in this section, the aspect ratio of Large Helical Device (LHD) is $a/R = 0.11$, which satisfies the $a/R \ll 1$ criteria. A theoretical model for magnetic field in LHD is in [81]:

$$B = B_0 \left\{ 1 - \varepsilon_{00} - \varepsilon_t \cos\theta - \sum_{l=L-1}^{L+1} \varepsilon_l \cos[(l - Mq_0)\theta - M\alpha] \right\} \tag{4.38}$$

in which

$$L = 2, M = 2, \alpha = 0, q_0 = 1.9, \varepsilon_{00} = 0, \varepsilon_t = 0.087 \tag{4.39}$$

$$(\varepsilon_{L-1}, \varepsilon_L, \varepsilon_{L+1}) = \varepsilon_t(-0.28, 0.91, 0)$$

Other typical parameters for LHD are $\widehat{s} = -0.85, \eta_i = L_{ni}/L_{Ti} = 3, R/L_n = 3.33, \varepsilon = a/R = 0.11, T_i/T_e = 1.0$. As safety factor $q = rB_t/RB_p = 1.9$, then the toroidal magnetic field is much larger than poloidal field $B_t/B_p \approx 20$, then the magnetic field in orthogonal coordinates are

$$\boldsymbol{B} = B_p \boldsymbol{e_\theta} + B_t \boldsymbol{e_\varphi} \tag{4.40}$$

$$B_p \approx 0 \tag{4.41}$$

$$B_t = B_0(1 - \varepsilon_t \cos\theta) - B_0(\varepsilon_1 \cos(1 - Mq_0)\theta + \varepsilon_2 \cos(2 - Mq_0)\theta) \tag{4.42}$$

In spite of the slight difference between $\varepsilon_t = 0.087$ and aspect ratio $\varepsilon = 0.11$, equation (4.42) can still be interpreted as the sum of first order approximation of Tokamak and non-axisymmetric corrective term related to geometric parameters. Therefore, the influence of helical magnetic geometry on drift wave will depend on the corrective term. In two-fluid drift wave model, curvature terms ∇B and $\nabla \times \boldsymbol{B}$ will appear as we deal with terms like $\nabla \cdot \boldsymbol{v_E}$ and will need careful calculation using the stellerator magnetic field geometry. The gradient of magnetic field is

$$\nabla B = \boldsymbol{e_r}\frac{\partial B}{\partial r} + \boldsymbol{e_\theta}\frac{\partial B}{r\partial\theta} \tag{4.43}$$

in which

$$\frac{\partial B}{\partial r} = -\frac{B_0}{R} - \frac{B_0}{R} rM\frac{dq}{dr}[\varepsilon_1\theta\sin(1 - Mq)\theta + \varepsilon_2\theta\sin(2 - Mq)\theta] \tag{4.44}$$

Besides the usual curvature term $-B_0/R$, equation (4.44) contains terms varying fast with poloidal angle θ. As we are only intersted in turbulent transport in radial direction, we can average quantities over poloidal direction and retain only total influence. Some useful formulas are

$$< \sin(A\theta) >=< \cos(A\theta) >= 0 \tag{4.45}$$

$$< \theta \sin(A\theta) >= -1/A, < \theta \cos(A\theta) >= 1/A$$

in which, $<>$ is the average operator and $< f >= (1/2\pi) \int_0^{2\pi} f d\theta$. Apply this operator on equation (4.44), we get

$$< \frac{\partial B}{\partial r} >= -\frac{B_0}{R}\left(1 + qM\widehat{s}\left[\frac{\varepsilon_1}{Mq-1} + \frac{\varepsilon_2}{Mq-2}\right]\right) = -\frac{B_0}{R}(1+\lambda) \tag{4.46}$$

Plug in the value of these parameters and calculate $\lambda \approx -0.61$. Using the same strategy on other curvature terms, we can have

$$< \frac{\partial B}{\partial \theta} >= 0 \tag{4.47}$$

$$< \nabla \times \boldsymbol{B} >=< -\frac{\boldsymbol{e_\theta}}{h_r h_\varphi}\frac{\partial}{\partial r}(h_\varphi B_\varphi) >= \frac{B_0}{R}\lambda \boldsymbol{e_\theta} \tag{4.48}$$

Then the curvature terms in two-fluid equations are expressed as

$$\nabla \cdot \boldsymbol{v_E} = \frac{1}{RB}(-2-\lambda)\frac{\partial \phi}{\partial y} \tag{4.49}$$

$$\nabla \cdot (n\boldsymbol{v_d}) = \frac{1}{RB}(-2-\lambda)\frac{T}{qn}\frac{\partial n}{\partial y} \tag{4.50}$$

Taking advantage of these expressions and using the same normalization principle, the set of linear two fluid equations including magnetic curvature effects in stellerator is

$$\frac{\partial n_i}{\partial t} + \left[\frac{L_{ne}}{L_{ni}} - \frac{L_{ne}}{R}(2+\lambda)\right]\frac{\partial \phi}{\partial y} + \frac{T_i}{T_e}\frac{L_{ne}}{R}(-2-\lambda)\frac{\partial n_i}{\partial y} - \frac{\partial}{\partial t}\nabla_\perp^2 \phi = 0 \tag{4.51}$$

$$\frac{\partial n_z}{\partial t} + \left[\frac{L_{ne}}{L_{nz}} - \frac{L_{ne}}{R}(2+\lambda)\right]\frac{\partial \phi}{\partial y} + \frac{T_z}{ZT_e}\frac{L_{ne}}{R}(-2-\lambda)\frac{\partial n_z}{\partial y} - \frac{A}{Z}\frac{\partial}{\partial t}\nabla_\perp^2 \phi = 0 \tag{4.52}$$

$$\frac{\partial n_e}{\partial t} + \left[1 - \frac{L_{ne}}{R}(2+\lambda)\right]\frac{\partial \phi}{\partial y} - \frac{L_{ne}}{R}(-2-\lambda)\frac{\partial n_e}{\partial y} + \nu\nabla_{\parallel}^2(\phi - n_e) = 0 \quad (4.53)$$

$$f_z n_z + (1-f_z)n_i = n_e \quad (4.54)$$

where the definition of these parameters can be found in Eq.(4.27). Therefore, according to equation (4.31), radial impurity flux is

$$\Gamma_z = \sum_k k_y \rho_s c_s n_z \frac{\gamma k_y \left[\frac{L_{ne}}{L_{nz}} - \frac{L_{ne}}{R}(2+\lambda) + \frac{A}{Z}\frac{T_z}{ZT_e}\frac{L_{ne}}{R}(2+\lambda)\right]}{\gamma^2 + \left[\omega_r + \frac{T_z}{ZT_e}\frac{L_{ne}}{R}(2+\lambda)k_y\right]^2}\left|\frac{e\phi_k}{T_e}\right|^2 \quad (4.55)$$

Chapter 5

The macro-instabilities in the pedestal region: The peeling-ballooning modes and the Edge-Localized modes(ELMs)

In this chapter, we will first show the fundamental linear characteristics of the peeling-ballooning(P-B) modes and the nonlinear features of the ELM crashes using the shifted-circular geometry (or limiter tokamak). Then two interesting studies related to P-B modes and ELM bursts will be presented. One is the attempted explanations[90] of the famous scaling law between the ELM size and the edge collisionality in Loarte *et al*[45] using the shifted-circular geometry. Another is the studies of the linear P-B modes behaviors between the standard and snowflake divertor geometry, using the DIII-D H-mode discharge equilibrium profiles[47]. In addition, the three-field reduced MHD model under the BOUT++ framework is described in the beginning of this chapter.

5.1 Three-field reduced MHD model

We use a two-fluid three-field reduced MHD model to simulate the coupled peeling-ballooning modes and the ELM crashes[88]. The three coupled fields that evolve with time are vorticity $\tilde{\varpi}$, pressure $\tilde{p}$ and parallel vector potential $\tilde{A}_{\parallel}$. The set of equations (5.1) to (5.5) is derived by neglecting electron inertia ($m_e \approx 0$), ion acoustic waves ($v_{\parallel} \approx 0$) and the Hall effect ($\boldsymbol{v_e} \approx \boldsymbol{v_i}$).

$$\frac{d\tilde{\varpi}}{dt}+\frac{1}{B_0}[\tilde{\phi},\tilde{\varpi}] = B_0\nabla_{\parallel 0}\tilde{J}_{\parallel}+B_0\tilde{\boldsymbol{b}}\cdot\nabla J_{\parallel 0}+[\tilde{J}_{\parallel},\tilde{A}_{\parallel}]+2\boldsymbol{b_0}\times\boldsymbol{\kappa_0}\cdot\nabla\tilde{p}+\mu_{i,\parallel}\partial^2_{\parallel 0}\tilde{\varpi}+\mu_{i,\perp}\nabla^2_{\perp}\tilde{\varpi} \tag{5.1}$$

$$\frac{d\tilde{p}}{dt} + \boldsymbol{V_{E1}} \cdot \nabla P_0 + \frac{1}{B_0}[\tilde{\phi},\tilde{p}] = \chi_{\parallel}\partial^2_{\parallel 0}\tilde{p} \tag{5.2}$$

$$\frac{d\tilde{A}_{\parallel}}{dt} = -\nabla_{\parallel 0}\tilde{\phi} - [\tilde{\phi},\tilde{A}_{\parallel}] + \frac{\eta}{\mu_0}\nabla^2_{\perp}\tilde{A}_{\parallel} - \frac{\eta_H}{\mu_0}\nabla^4_{\perp}\tilde{A}_{\parallel} \tag{5.3}$$

$$\varpi = \frac{n_0 M_i}{B_0}\left(\nabla^2_{\perp}\tilde{\phi} + \frac{1}{n_0 Z_i e}\nabla^2_{\perp}\tilde{p}_i\right) \tag{5.4}$$

$$J_{\parallel} = J_{\parallel 0} + \tilde{J}_{\parallel}, \tilde{J}_{\parallel} = -\frac{1}{\mu_0}\nabla^2_{\perp}\tilde{A}_{\parallel}, \boldsymbol{V_{E1}} = \frac{1}{B_0}(\boldsymbol{b_0} \times \nabla_{\perp}\tilde{\phi}) \tag{5.5}$$

where $d/dt = \partial/\partial t + \boldsymbol{V_{E0}} \cdot \nabla$, $\boldsymbol{V_{E0}} = (\boldsymbol{b_0} \times \nabla_{\perp}\Phi_0)/B_0$, $\nabla_{\parallel}F = B\partial_{\parallel}(F/B)$, $\partial_{\parallel} = \partial_{\parallel 0} + \tilde{\boldsymbol{b}} \cdot \nabla$ and $\tilde{\boldsymbol{b}} = \tilde{\boldsymbol{B}}/B_0 = \nabla\tilde{A}_{\parallel} \times \boldsymbol{b_0}/B$. In addition, curvature term $\boldsymbol{\kappa}_0 = \boldsymbol{b_0} \cdot \nabla\boldsymbol{b_0}$ and pressure fluctuation $\tilde{p}_i = \tilde{p}_e = \tilde{p}/2$. The parameters with subscript '0' represent equilibrium parts while the ones with tilde on top represent fluctuating parts. Nonlinear terms are expressed by Poisson brackets, $[f, g] = \boldsymbol{b_0} \cdot (\nabla f \times \nabla g)$. The transport coefficients, such as resistivity (η), hyper-resistivity (η_H), perpendicular viscosity ($\mu_{i,\perp}$) and thermal diffusivity ($\chi_\parallel$), are assumed zero unless specified, and their effects on the P-B modes are described throughly in [88]. Ion parallel viscosity $\mu_{i,\parallel} = 0.1\omega_A R^2$ is retained in all simulations for numerical convergence.

To investigate the effects of ion diamagnetic drift on the P-B mode, an extra term is included in vorticity expression (5.4) as $(1/n_0 Z_i e)\nabla_\perp^2 \tilde{p}_i$. Meanwhile, background electric potential Φ_0 was set correspondingly to keep the total background flow zero. That is:

$$\boldsymbol{V_0} = \boldsymbol{V_{di}} + \boldsymbol{V_E} = \frac{1}{eZ_i n_{i0}} \frac{\boldsymbol{b_0} \times \nabla P_{i0}}{B} + \frac{\boldsymbol{b_0} \times \nabla \Phi_0}{B} = 0 \tag{5.6}$$

where $P_{i0} = P_0/2$. In other words, background electric potential is set $\Phi_0 = -P_{i0}/eZ_i n_{i0}$. In ideal P-B model, $\Phi_0 = 0$ and $\tilde{\varpi} = (n_0 M_i/B_0)\nabla_\perp^2 \tilde{\phi}$ are applied.

Equations (5.1)-(5.5) are solved using a non-orthogonal field-aligned coordinate system with shifted radial derivatives, where (x, y, z) labels magnetic surface, distance along magnetic field line and toroidal angle. In addition, orthogonal coordinates (Ψ, θ, ζ) are also used in this paper to label radial, poloidal and toroidal positions in some qualitative analysis. Sundials CVODE package is used to solve time evolution matrices implicitly. Radial boundary conditions are set as $\tilde{\varpi} = 0, \nabla_\perp^2 \tilde{A}_\parallel = 0, \partial\tilde{p}/\partial\psi = 0$ and $\partial\tilde{\phi}/\partial\psi = 0$ on the inner radial boundary, and $\tilde{\varpi} = 0, \nabla_\perp^2 \tilde{A}_\parallel = 0, \tilde{p} = 0$ and $\tilde{\phi} = 0$ on outer radial boundary. The domain is periodic in the parallel coordinates y with a twisted-shift condition to simulate the continuous field lines. Periodic boundary condition is also applied in z (toroidal) direction and Fast-Fourier

Transformation (FFT) scheme is used in this direction. Moreover, we use insulating divertor plate boundary conditions for tokamak geometries, i.e. we set all fluctuating variables to zero on divertor plates.

5.2 Fundamental features of the P-B modes and ELM crash

In this section, we will demonstrate some of the fundamental features of the P-B modes and the ELM crash using reduced MHD model and shifted-circular geometry. The shifted-circular toroidal equilibria, cbm18_dens8, is generated by the TOQ equlibrium code[5] with an aspect ratio of 2.9. The pressure and current profiles are shown in figure (5.1). This equilibrium is far from the marginal P-B instability threshold with a pedestal pressure $\beta_{top} = 1.941 \times 10^{-2}$ and a normalized pedestal width $W_{ped}/a = 0.0486$. We can see that the peak pressure gradient radial position is about $\Psi_{nor} = 0.85$ and the 'separatrix' of the limiter tokamak geometry is denoted by $\Psi_{nor} = 1.0$.

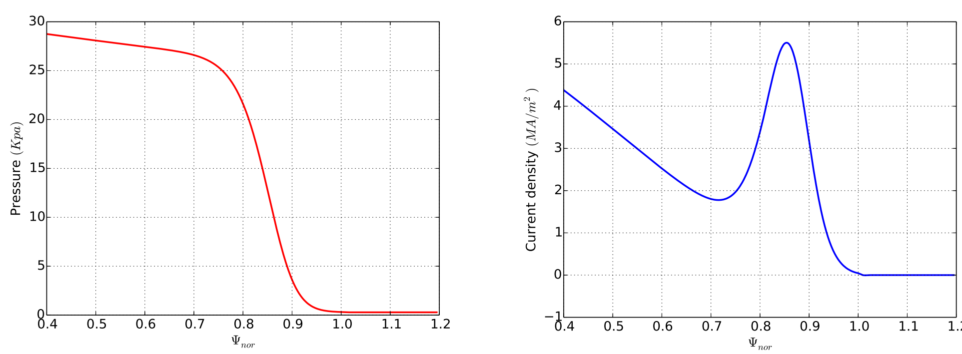

Figure 5.1: The pressure (left) and current density (right) profiles of the cbm18_dens8 equilibrium versus the normalized poloidal flux (Ψ_{nor}).

5.2.1 Linear P-B modes

The linear spectrum of the P-B modes are shown in figure (5.2). In ideal case, the real frequency of P-B modes are zeros and the growth rate increases with toroidal mode number (n) and saturates at high n. With the ion diamagnetic drifts, the modes get stabilized at high n ($n > 30$). In addition, the modes start to propagate to the ion diamagnetic direction and the frequency is proportional to n. The radial and poloidal mode structure of the P-B modes at $n = 15$ are shown in the left and right figure of figure (5.3). The linear P-B modes radially localize around the peak pressure gradient local position and poloidally localize at the outboard midplane, i.e. the bad-curvature region of the tokamak. These mode structure features are consistent with the mode nature: the Rayleigh-Taylor instability driven by the pressure gradient and fictiticous gravitational force (curvature).

5.2.2 ELM crash

Having shown the linear characteristics of the P-B modes, we now present the simulation results of the ELM crashes. The mechanism of the ELM crash in the nonlinear stage of the P-B modes is described in Xu *el al*[87] as the formation of the stochastic field lines in the pedestal region due to the magnetic reconnections. The stochastic field lines serve as the channel for the energy and particle transport during the ELM crashes. Therefore, the resistivity and hyper-resistivity is needed for the reconnection. In ELM study, we use the nonlinear reduced MHD model with the normalized resis-

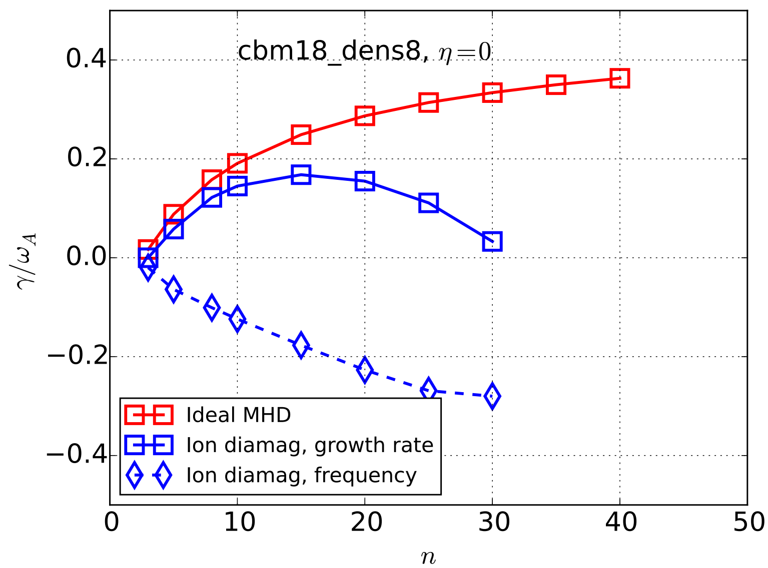

Figure 5.2: The linear growth rate and real frequency of the P-B modes as a function of the toroidal mode number. The red line represent the growth rate of the P-B modes in ideal case, while the blue lines represent the growth rate and real frequency with ion diamagnetic drifts. Resistivity is set to zero.

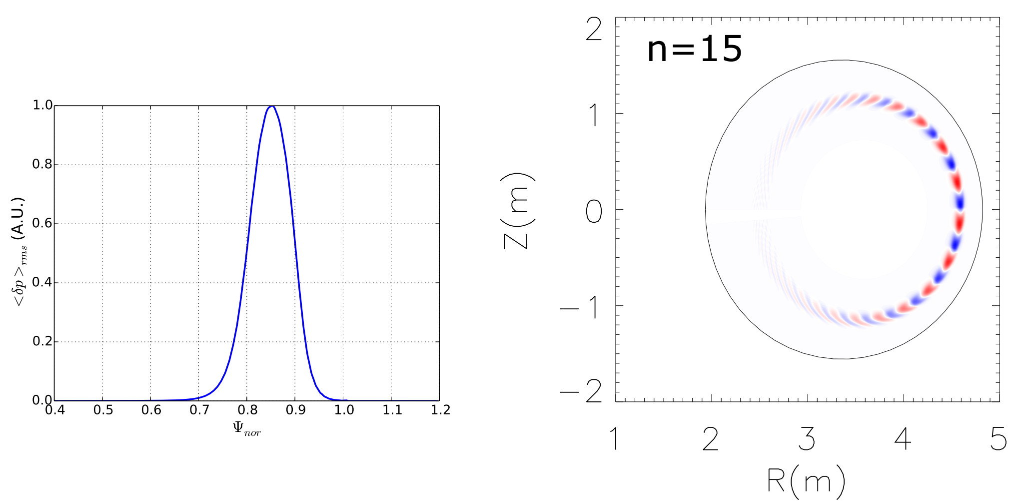

Figure 5.3: The linear radial (left) and poloidal (right) structure of the P-B mode at $n = 15$.

tivity $\eta/\omega_A R^2\mu_0 = 1\times10^{-8}$ and hyper-resistivity ($\eta_H/\omega_A R^2\mu_0 = 1\times10^{-13}$), where ω_A and R are Alfven frequency and major radius. The equlibrium is still the cbm18_dens8.

Figure (5.4) shows the time evolution of the root-mean-square(rms) amplitude of the pressure perturbation (left) and the change of the pedestal pressure profiles. From the left figure, we can see clearly that the ELM crash occurs at $t = 80t_A$ when the exponential linear growing stops and the initial crash happens. After the initial crash, the amplitude decreases by a certain amount and saturates at a lower level. The decrease of the amplitude implies that there are energy bursts from the pedestal to the scrape-off layer, i.e. the ELM bursts. The crash process of the pedestal is shown in the right figure, where we can see a void appears inside the peak pressure gradient radial position and a blob appears outside. The blob represents the energy comes out of the edge during the ELM crash. After the initial crash, the size of the blob almost keeps the same with very small increase, which means that the majority of the energy bursts occur at the very short initial crash phase and very little energy bursts after that, i.e. the spreading phase[46]. It is more straightforward to see the initial crash and spreading phase during an ELM crash in figure (5.5), where the time evolution of the ELM size is shown. The ELM size is defined as $s = \Delta W_{ped}/W_{ped}$ and represents the ratio of the ELM energy loss $\Delta W_{ped} = \int_{R_{in}}^{R_{out}} dR \int d\theta (P_0 - \langle P\rangle_\zeta)$ to the pedestal stored energy $W_{ped} = \int_{Rin}^{R_{out}} dR \int d\theta P_0$. After the initial crash at $t = 80t_A$, the spreading phase start at $t = 100t_A$ and the ELM size saturates at approximately 2%.

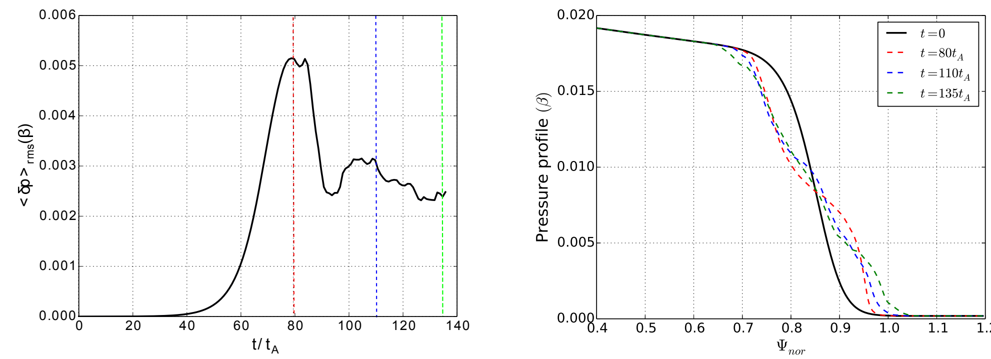

Figure 5.4: *Left figure*: the time evolution of the pressure perturbation amplitude through an ELM crash process. *Right figure*: the change of the pedestal pressure profile during the ELM crash process. The dashed lines in the left figure corresponds to the time denoted in the right figure with the same color.

During the ELM crash phase, the inverse cascade occurs and the energy trans-

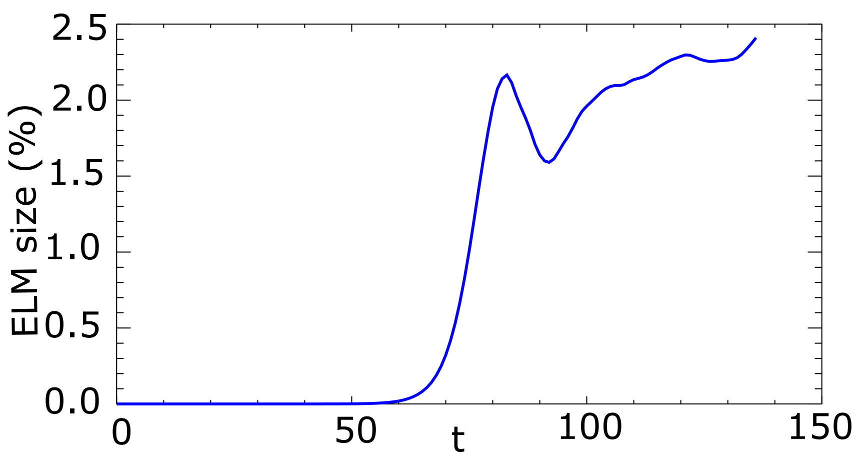

Figure 5.5: The time evolution of the ELM size during the ELM crash process.

fers to the low-n modes. As shown in figure (5.6), the different harmonics have randomly different amplitude at the initial moment and $n = 20$ toroidal mode becomes the dominant mode in the linear phase. After the ELM crash occurs, the inverse cascade appears and the energy transfers to the toroidal mode with lower n ($n = 10$), which is the dominant mode during the spreading phase. A qualitative picture of the inverse cascade is shown in figure (5.7) using the poloidal cross-section plot of the pressure perturbation.

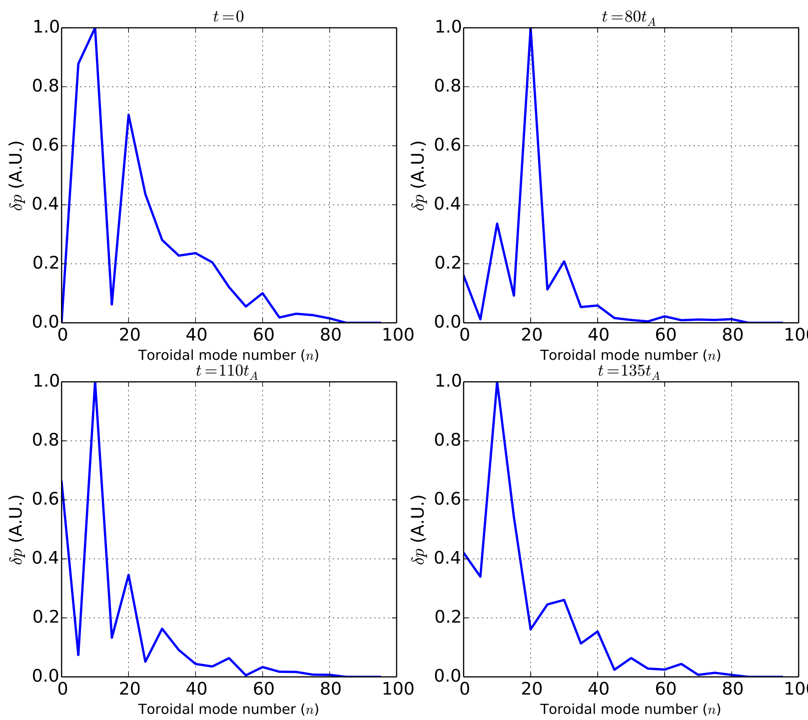

Figure 5.6: The toroidal spectrum of the P-B instability during the ELM crash process.

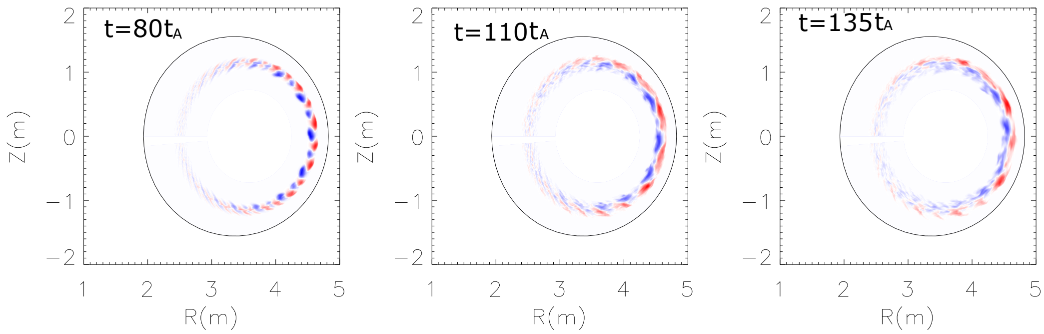

Figure 5.7: The poloidal cross-section view of the pressure perturbation (δp) at different time during ELM crash. The red color represents positive value while the blue represents the negative value.

5.3 The scaling law between ELM size and the edge collisionality

As type-I ELMs have been the crucial factor to the H-mode confinement, it is worthwhile to understand their direct dependences in the pedestal region from the machine perspective, in addition to the studies on the nature. Loarte *et al*[45] gave one of the most important scaling law: the inverse correlation between ELM size and the edge collisionality, which includes experimental data from almost all the major Tokamaks in the world and extrapolate to ITER H-mode scenario. However, the physics beneath the beautiful scaling law remain unclear. As the computing capabilities grow exponentially in the past decade, simulations may be a viable way to dig into the deep darkness, and the very first step is to exactly reproduce the scaling law.

5.3.1 The equilibria

The edge collisionality generally depends on the density and temperature profile:

$$\nu = \frac{4\pi \sum_i n_i Z_i e^4 ln\Lambda}{(4\pi\epsilon_0)^2 m_e^2 v_{Te}^3} \tag{5.7}$$

Therefore, the collisionality is proportional to $n/T^{3/2}$. In order to generate a sequence of equilibria with different edge collisionality while not changing the P-B stability itself, we keep the pressure profile the same and alter the density and temperature profile at the same time as in figure (5.8). The density and temperature profiles in the seven cases follow the equation:

$$n_0(\Psi) = N_0 \left(\frac{P_0(\Psi)}{P_0(0)}\right)^{0.3}, T_0(\Psi) = P_0(\Psi)/(2n_0(\Psi)) \tag{5.8}$$

where $N_0 = 1, 3, 5, 7, 9, 12, 15, 20 \times 10^{19} m^{-3}$. $P_0(0)$ is the pressure at the top of the pedestal. Table 5.1 shows the edge collisionality at the peak pressure gradient radial position for different cases. These eight equilibria are generated based on the shifted-circular equilibria, cbm18_dens6, which is similar to cbm18_dens8, but is closer to the marginal P-B instability threshold with $\beta = 1.45 \times 10^{-2}$ and $W_{ped}/a = 0.0518$. In order to make all the profiles consistent in one equilibrium, we run EFIT code every time we alter the density profile. Therefore, the current density profiles, which is calculated using Sauter bootstrap current model[60], show a decreasing trend as the density and collisionality increases.

$N_0(10^{19}m^{-3})$	1.0	3.0	5.0	7.0	9.0	12.0	15.0	20.0
ν	1.91×10^{-3}	4.03×10^{-2}	0.159	0.381	0.72	1.606	2.908	6.197

Table 5.1: The edge collisionality calculated by Eq. 5.7 at the peak pressure gradient radial position for eight cases with different density profiles.

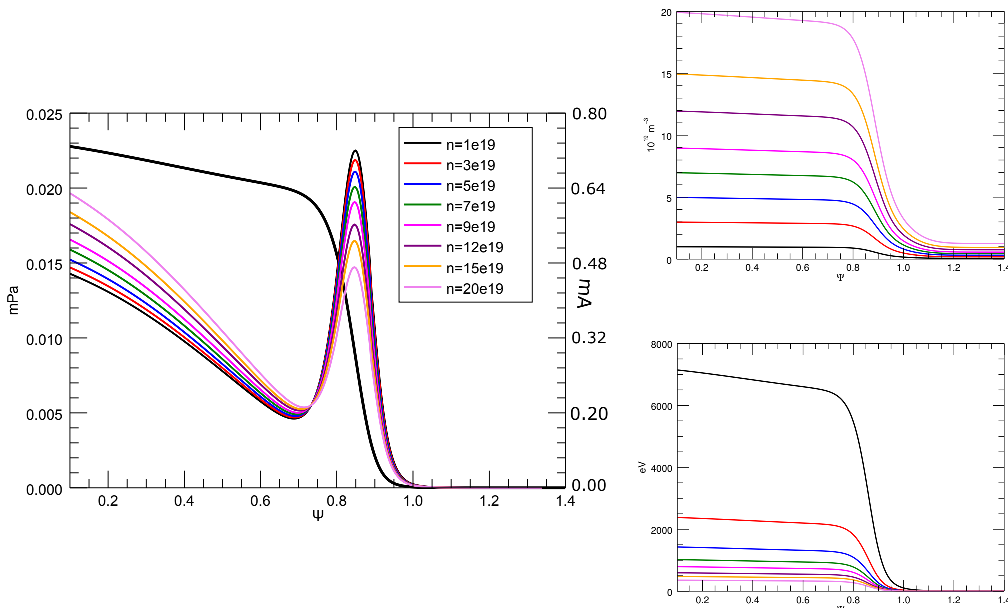

Figure 5.8: *Left figure*: The pressure and current density profiles for different pedestal density cases. The pressure profile is the same as the shifted-circular equilibrium cbm18_dens6. *Right figures*: The density profiles (top) and the temperature profiles (bottom).

5.3.2 The Linear growth rate of P-B modes

The linear growth rate of the P-B modes is shown in figure (5.9). Very interestingly, we find that as the pedestal density increases, i.e. the edge collisionality increases, the low-n modes get stabilized and the stabilization effects on high-n modes disappear. The explanation lies in two aspects: the ion diamagnetic effect and the bootstrap current. As the edge collisionality increases, the edge current decreases and the peeling mode, which is driven by the current, get stabilized. Meanwhile, the ion diamagnetic stabilization effects, which is proportional to $1/n$, become weaker as the density increases. Hence, the stabilization on the high-n modes gets weaker and even nearly disappears for $N_0 = 20 \times 10^{19} m^{-3}$ case.

5.3.3 The scaling law between ELM size and edge collisionality

The time evolution of the relative ELM energy loss is shown in the left figure of figure (5.10). There are two things that need to be noticed in the figure. Firstly, as the fluid model (reduced MHD) we are using to simulate ELM bursts lacks the necessary energy flow from the core region, which is considered to be very important for the rebuild of the pedestal between ELM cycles, the ELM size theoretically will keep increasing in the spreading phase, until the perturbations reach the inner boundary. After that, the ELM size will dramatically increase due to numerical mechanism, like the red and blue lines in the figure. In order to make the correct measurements of the relative ELM energy loss, we draw an imaginary line (the dashed lines) to extrapolate

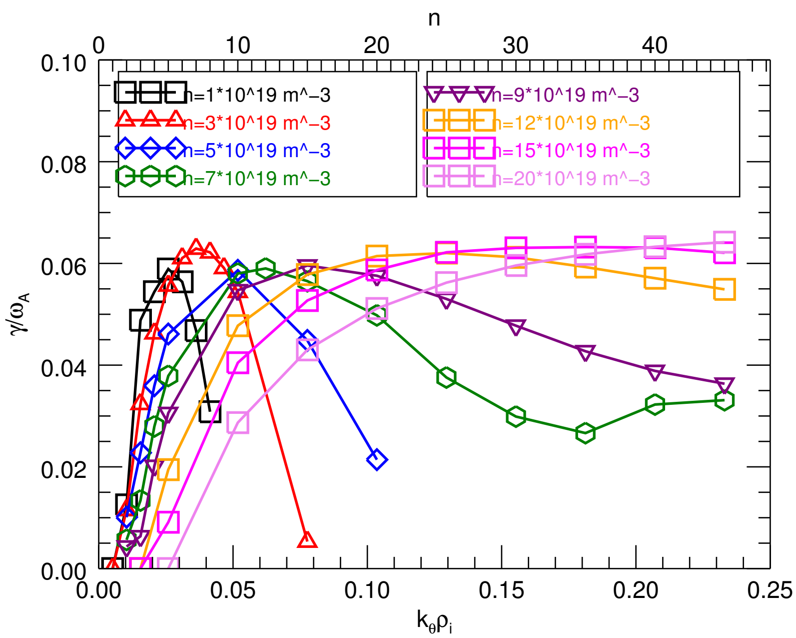

Figure 5.9: The linear growth rate of the P-B modes as a function of toroidal mode numbers (n) and corresponding poloidal wavenumber ($k_\theta \rho_i$) for all the eight cases. Ion diamagnetic drift terms are retained and resistivity is set to be $\eta/\omega_A R^2 \mu_0 = 1 \times 10^{-8}$.

the ELM size as if the perturbations never reach the boundary. Another thing is that we set $t = 4300t_A$ as the measurement time for ELM size, which is represented by the vertical dashed line in the figure. The reason is that it is the typical time interval for an entire ELM burst in the tokamak, for example, DIII-D. The results are shown in the right figure as red dots, overlaid with the multi-tokamak experimental data in Loarte *et al*[45]. The comparison shows very good agreement with the scaling law. The continuing study on the explanation of this scaling law using flux-driven model in BOUT++ is currently underway and will be seen in the future publications.

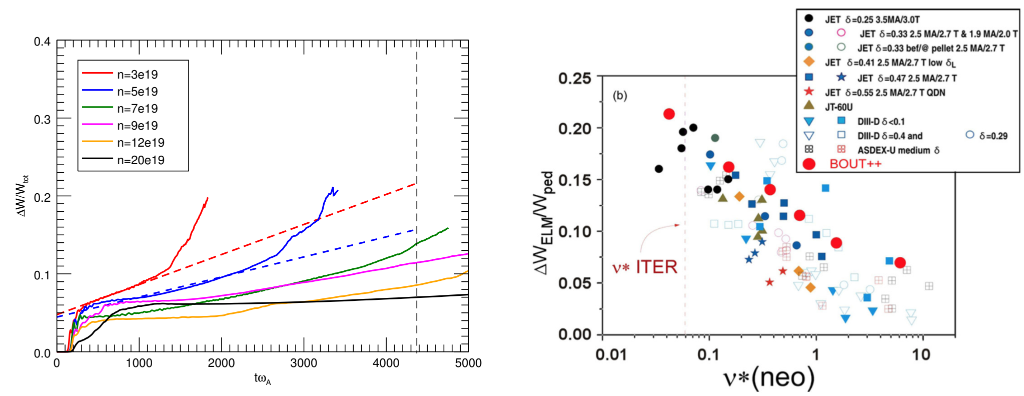

Figure 5.10: *Left figure*: The time evolution of the ELM size for $N_0 = 3, 5, 7, 9, 12 \times 10^{19} m^{-3}$ cases. The vertical black dashed line shows the time when we take the ELM size measurements. *Right figure*: The relative ELM energy loss scaling vs. collisionality with multi-tokamak experimental data[45] overlaid with BOUT++ simulation results (red bullet).

5.4 Linear simulations of P-B modes in STD and SF-plus divertor geometry

In this section, we will show another important studies on the P-B modes in the pedestal region: the impact of the snowflake configuration on the linear behavior of the P-B modes.

5.4.1 Equilibrium

The standard (STD) lower single-null equilibrium is taken from experimental measurements in DIII-D ELMing H-mode[18] (shot number 149394, $t = 2241$ ms) and generated by the kinetic EFIT code[41]. The snowflake (SF) plus equilibria are generated by reconstruction code CORSICA[69] based on STD equilibria and match the EFIT plasma boundary except near the lower null point. Reconstructing SF-plus geometry using CORSICA is described in detail in [70]. The distance between two null points in SF-plus geometry is 25cm. A 2-D orthogonal (Ψ, θ) equilibrium grid for simulation is then generated by part of BOUT++ code. Figure 5.11(a) and (b) show the shape of equilibrium grid in STD (a) and SF-plus (b) divertor geometry with a few grid lines. Figure5.11(c) and (d) shows the enlarged part around the null point. According to the theory[57], the flux around the null point is more expanded in the SF-plus divertor configuration, which aims to redistribute streaming particles to two additional legs, thereby reduce heat flux on divertor plates. Through Figure 5.11, it is clear that this important geometric feature is retained in this study, in spite of the fact that the second null point is not included in our simulation domain due to technical limitations. The major radius of DIII-D is $R \approx 1.6m$ and the aspect ratio R/a is approximately 4.5. The radial simulation domain extends from $\Psi_{nor} = 0.9$ to $\Psi_{nor} = 1.1$, where $\Psi_{nor} = (\Psi - \Psi_{axis})/(\Psi_{sep} - \Psi_{axis})$ is normalized flux coordinate. $\Psi_{nor} = 1$ represents the separatrix, while $\Psi_{nor} < 1$ and $\Psi_{nor} > 1$ represent edge region and the scrape-off layer (SOL). One notable feature about the equilibrium grid is that the private flux region is included in the simulation domain. Therefore, poloidal indices start from the inner divertor plate and increase clockwise to the outer divertor plate.

The pedestal pressure P_0 and edge parallel current $J_{\|0}$ are taken directly from experimental measurements. To investigate only the influence of the divertor geometry on the P-B modes, P_0 and $J_{\|0}$ are set to be identical for STD and SF-plus divertor cases. However, other equilibrium profiles such as poloidal magnetic field (B_p) and safety factor (q) vary among these two geometries. This is due to the different current density in poloidal field (PF) and central solenoid (CS) coils, which need to be adjusted carefully to implement SF-plus divertor. Figure 5.12 (a) shows the uniform pressure profile and different safety factor profile as a function of normalized magnetic flux. The safety factor profiles are almost the same inside the separatrix and show discrepancy for $\Psi_{nor} \sim 1.0$. Figure 5.12 (b) shows the edge current density and poloidal magnetic field profile at outer midplane. As the edge current density in this discharge is quite large ($J_{\|max} \approx 0.9MA/m^2$),the poloidal magnetic field increases in radial direction in the pedestal region in STD and SF-plus

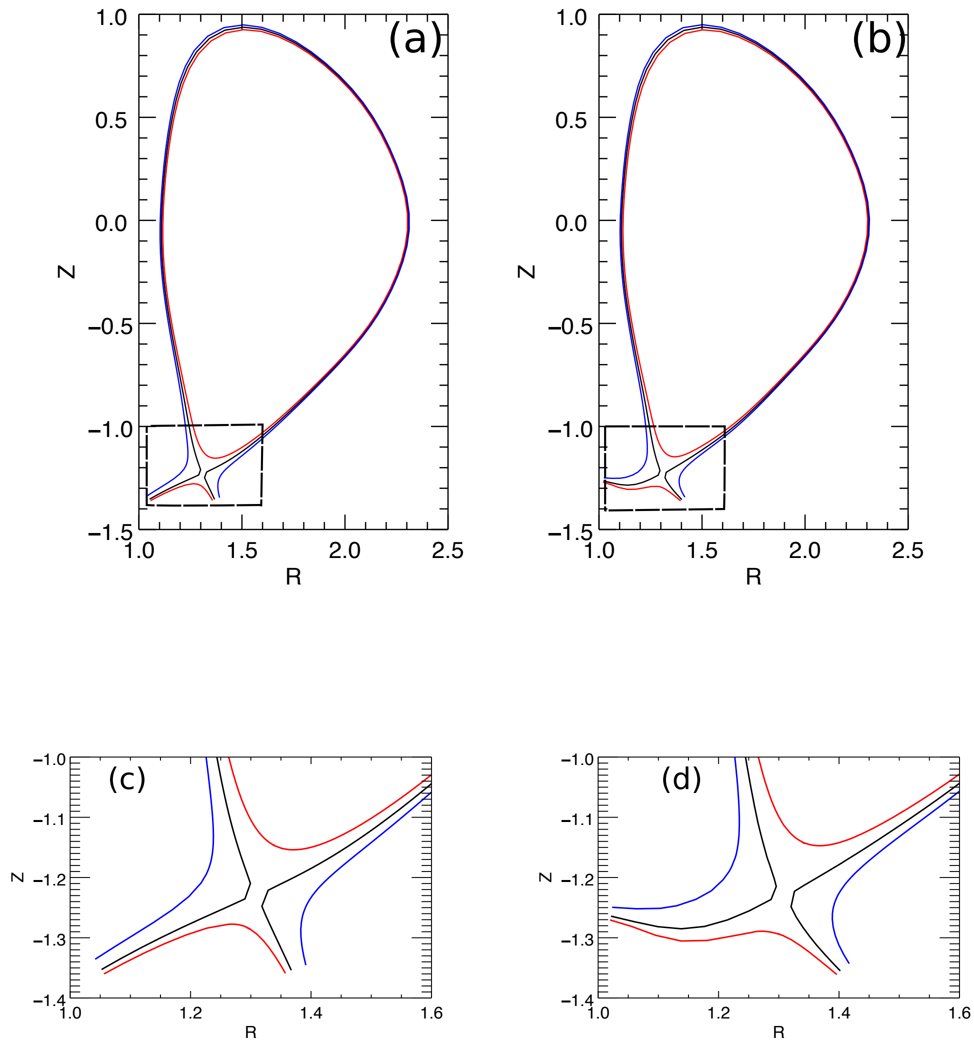

Figure 5.11: Figure (a) and (b) shows the entire equlibrium grid for STD and SF-plus geometry, while figure (c) and (d) shows enlarged area in dashed rectangle. In all figures, red, black and blue lines represent magnetic surfaces with $\Psi_{nor} = 0.985, 1, 1.013$.

geometry. Moreover, the normalized pedestal height $\beta_0 = 2.3\times10^{-2}$ and width $L_{ped}/a = 0.046$ exceeds the P-B instability threshold[64], as expected for H-mode experimental equilibria. The peak pressure radial gradient $dP_0/d\Psi$ is located at $\Psi_{nor} = 0.972$. Without loss of generality, density profiles are held radially constant, $n_{i0} = n_{e0} \approx 2.5\times10^{19}m^{-3}$, where subscripts i and e stands for ion and electron. Accordingly, the temperature profiles $T_{i0} = T_{e0} = (P_0/n_0)/2$ are kept the same for ions and electrons. The pedestal temperature T_{ped} defined as the temperature at $\Psi_{nor} = 0.90$ is $T_{i,ped} = T_{e,ped} = 2.46$KeV. The toroidal magnetic field in the pedestal region is $B_{t0} = 1.5T$ and the poloidal magnetic field is approximately $0.4T$ at outer midplane.

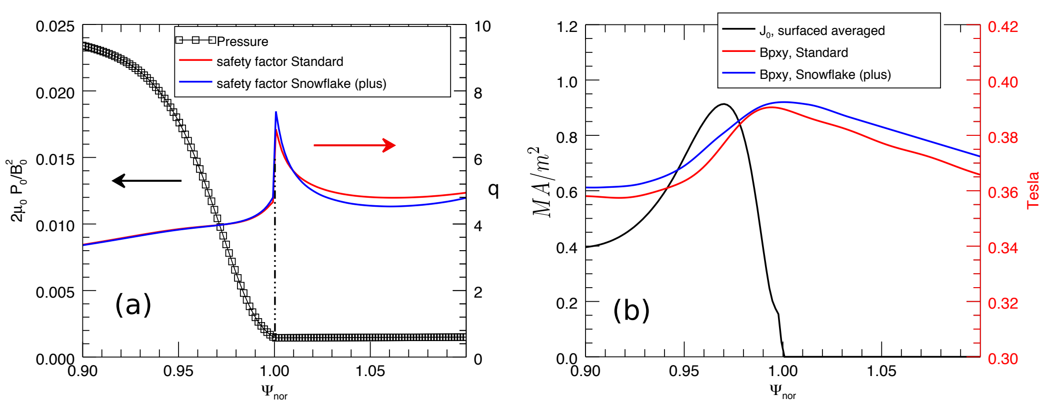

Figure 5.12: *Figure (a)*: Normalized pedestal pressure and safety factor in STD (red) and SF-plus (blue) geometry. Radial position of separatrix is marked by vertical black dashed line. *Figure (b)*: Surface averaged edge current ($< J_0 >_{sur} = (\int J_0 dl/B)/(\int dl/B)$, where dl is infinitesimal segment along field line) and poloidal magnetic field at outer midplane.

5.4.2 Linear simulation results

In this section, the linear growth rate and mode structure of ideal P-B modes are investigated in STD and SF-plus divertor geometry. The simulations are conducted for different toroidal mode numbers from $n = 1$ to $n = 45$. Diamagnetic effects and background $\boldsymbol{E} \times \boldsymbol{B}$ drift are not included unless otherwise stated. The number of grid points in each directions are $n_x = 132$, $n_y = 64$ and $n_z = 17$. The simulation domain in radial and poloidal direction is $0.9 < \Psi_{nor} < 1.1$ and $0 < \theta < 2\pi$. In toroidal direction, only $1/n$ torus is simulated for each toroidal mode number n and the toroidal resolution $nz = 17$ represents a complete sinusoidal period in this piece of torus. In this way, the high toroidal mode numbers could be treated correctly and efficiently.

5.4.2.1 Growth rate

Linear simulations of the P-B modes using BOUT++ have shown good agreement in growth rate and mode structure with GATO and ELITE in shifted circular geometry[88]. Therefore, it is reasonable to use it for simulations in divertor tokamak geometry, but careful benchmarks are under way and will be given in future publications. 5.13 shows growth rate of ideal P-B mode, resistive P-B mode and P-B mode with ion diamagnetic effects, versus toroidal mode number n and normalized wave vector $k_\zeta \rho_i = (n/R)(\sqrt{T_i M_i}/eB)$. The growth rate is calculated using formula $\gamma = (1/P_{rms})(dP_{rms}/dt)$, where P_{rms} is the root-mean-square average of the pressure perturbation at outer midplane and peak pressure gradient radial position ($\Psi_{nor} = 0.972, ny = 38$). Consistent with normalization used in equation (5.1) to (5.5), the growth rate γ is normalized by the Alfven frequency $\omega_A = (1/R)(B/\sqrt{\mu_0 M_i n_0}) \approx 4.21 \times 10^6 s^{-1}$. It is found that the growth rate of the ideal P-B mode in both configurations increases for low n and almost stays constant for high n, which is due to the shear Alfven stablization effects on high n ballooning modes. Ion diamagnetic effects stabilize P-B mode in a manner consistent with theoretical expectations[54]. Resistivity and hyper-resistivity destabilize P-B mode for $S = 10^8$ and $S_H = 10^{12}$ and lead to resistive ballooning mode, where $S = \omega_A R^2 \mu_0/\eta$ and $S_H = \omega_A R^2 \mu_0/\eta_H$. Most of all, SF-plus geometry destabilizes P-B mode in both ideal (red lines) and more realistic cases (blue, green lines). Besides, the destabilizing impact on P-B mode appears more evident for moderate and high n, which will be explained in the following section.

In our linear simulations, the poloidal $\boldsymbol{E} \times \boldsymbol{B}$ drift is set to be equal to the diamagnetic drift for simplicity when nonideal effects are included. However, this might be different from the $\boldsymbol{E} \times \boldsymbol{B}$ profiles observed in many tokamak experiments, especially at the separatrix, where transition from negative to positive electric field usually appears[56] and a large shear flow is induced. Reference [83] has analyzed the impact of the background $\boldsymbol{E} \times \boldsymbol{B}$ shear flow on the ballooning mode, demonstrating that the shear flow locally stabilizes the high n mode and constraints the radial mode extents. In our case, as shown later in 5.15, the mode structure mainly localizes inside the separatrix, making the impact of large shear at the separatrix on the growth rate less important.

A sensitivity study of parallel viscosity ($\mu_{i,\parallel}$) and radial grid size is described in 5.14. As stated earlier, a parallel viscosity term is added to vorticity equation for numerical purposes. From 5.14 (a), we found that $\mu_{\parallel} = 0.1$ has less than 10% influence on results yet yields much faster numerical convergence. Besides, as the influence on simulation for both configurations is similar, this will not affect this comparative study. 5.14 (b) shows that the resolution of simulation grid we use ($nx = 132, ny = 64$) is high enough for both efficient and accurate simulations.

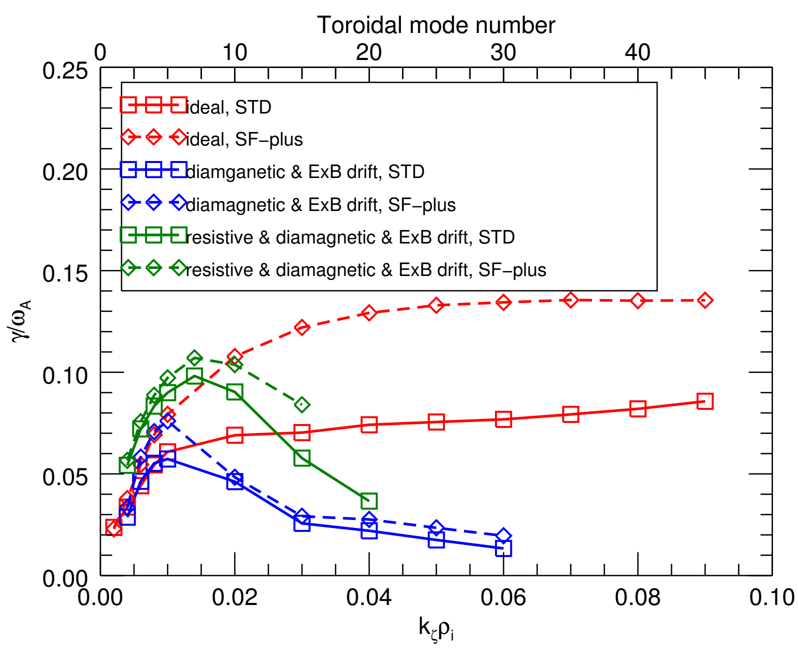

Figure 5.13: Growth rate of ideal P-B mode (red), resistive P-B mode (green) and P-B mode with ion diamagnetic effects (blue) in STD (solid square) and SF-plus (dash diamond) divertor geometry versus toroidal mode number n and normalized toroidal wave vector ($k_\zeta \rho_i$).

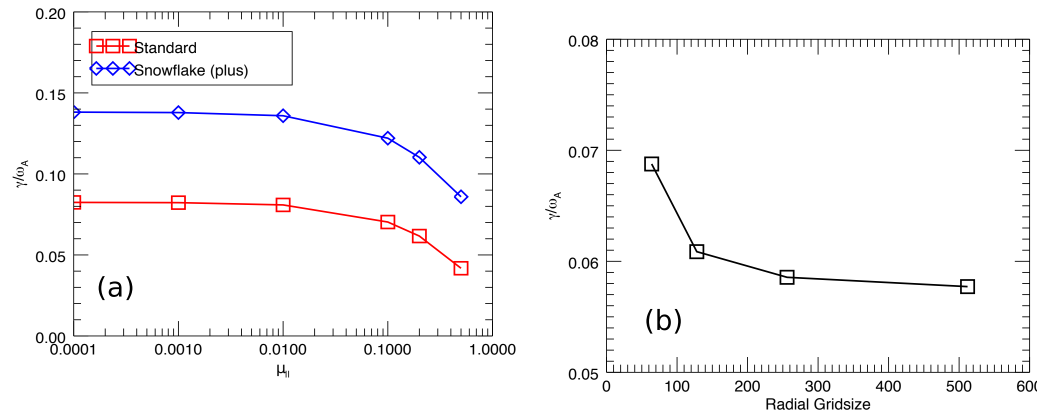

Figure 5.14: *Figure (a)*: Growth rate versus parallel viscosity $\mu_{\parallel}$ in STD (red) and SF-plus (blue) divertor geometry. *figure(b)*: Growth rate versus radial grid size, $nx = 68, 132, 260, 516$. Poloidal grid size is $ny = 64$. Toroidal mode number is fixed as $n = 15$ for both figures.

5.4.2.2 Mode structure

Pressure perturbations in tokamak geometry are generally expressed as superpositions of the eigenfunctions $\tilde{p}(\Psi, \theta, \zeta) = \sum_{m,n} p_{m,n}(\Psi) \exp(-im\theta - in\zeta)$, where θ and ζ are poloidal and toroidal angles. Given the fixed toroidal mode number n, the linear mode structure depends on the composition of poloidal harmonics. Each poloidal harmonic corresponds to a particular poloidal mode number m and localizes at rational surface $q = m/n$ in radial direction. These poloidal modes radially couple with each other due to toroidicity and form the global radial mode structure. In our simulations, a gaussian function is used for the initial pressure perturbations in both radial and poloidal directions. As time evolves, the mode structure gradually shifts to outer mid-plane where the so called 'bad curvature' localizes it and give it a ballooning structure. Root-mean-square averaged pressure perturbation $P_{rms}(\Psi, \theta, t)$ is used to demonstrate the mode structure in STD and SF-plus divertor geometry. The global radial mode structure is shown in 5.15(a). One obvious conclusion is that the radial mode structure becomes narrower as the toroidal mode number increases in both configurations, which is due to denser rational surfaces around the position of peak pressure gradient. Moreover, the comparison between STD and SF-plus geometry indicates that the P-B modes in SF-plus geometry has a larger radial spread for high toroidal mode number, e.g. $n = 35$, but slight differences for low mode number. This is of particular interest, because the width of radial mode structure is commonly found to be positively correlated with ELM size in the nonlinear stage. Although careful nonlinear simulations are ongoing and will be presented in future publications, this still provides us original motivation to seek explanation even in linear regime, which will be presented in this paper. One aspect that deserves extra attention is that the amplitude of all poloidal harmonics outside separatrix ($\Psi_{nor} > 1$) are zero, as there is no instability drive in the SOL in the equilibrium model ($dP_0/d\Psi = 0$ and $J_{\|0} = 0$) in linear stage. Nevertheless, in nonlinear stage pressure filaments propagate to SOL region and generate ELM, as described in figure 12 of reference [88].

While the P-B mode structure is broader in radial direction, it is found to be less extended in the poloidal direction as shown in 5.15(b). Before getting into the results, it is necessary to explain the relation between poloidal position and indices we use. As stated previously, the poloidal angle starts from

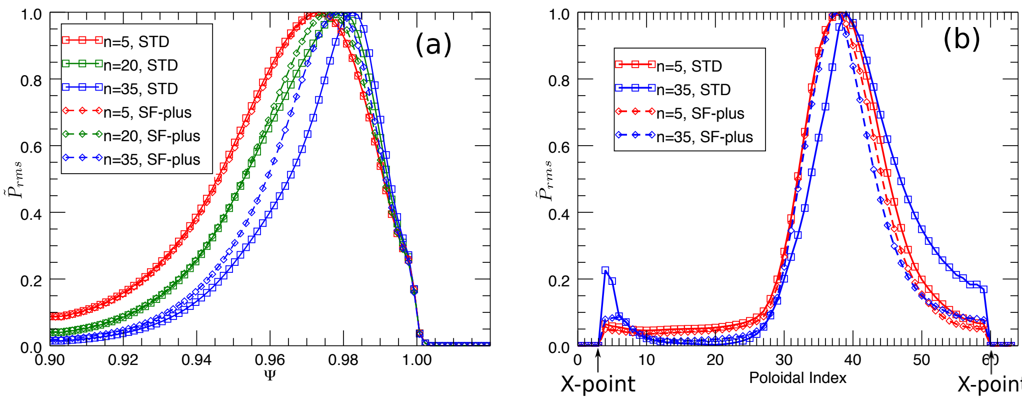

Figure 5.15: *Figure (a)*: The global radial mode structure is shown for $n = 5$ (red), $n = 20$ (green) and $n = 35$ (blue) in STD (solid square) and SF-plus (dash diamond) divertor geometry. This mode structure is the envelope of the mode structure of individual poloidal harmonics. Poloidal index is fixed at outer midplane ($ny = 38$).*Figure (b)*: Poloidal mode structure is shown for $n = 5$ (red), $n = 35$ (blue) in STD (solid square) and SF-plus (dash diamond) divertor geometry. Radial position is fixed at pressure peak gradient position ($\Psi_{nor} = 0.972$). Position of X-point is marked. normalized pressure perturbation $\tilde{P_{rms}} = P_{rms}/max(P_{rms})$ is used for both figures.

inner divertor target and increases clockwise to the outer target in equilibrium. Therefore, index $ny = 0$ and $ny = 63$ stands for poloidal position at inner and outer divertor plates in our simulation. As we use four grid point on each divertor leg, the indices $ny = 4$ and $ny = 59$ represent the same grid point nearest to the null point on certain magnetic surface, as marked on 5.15(b). In addition, index $ny = 38$ represents outer midplane. It is shown in 5.15(b) that poloidal spread in SF-plus divertor geometry is larger for $n = 5$ and $n = 35$. In particular, the P-B instability around the null point is found to be suppressed by the SF-plus geometry, especially for high toroidal mode number ($n = 35$). This is consistent with the results obtained from resistive ballooning mode in reference [58]. The reason of this will be detailed in the next section. 5.16 gives a more straightforward picture of poloidal mode structure.

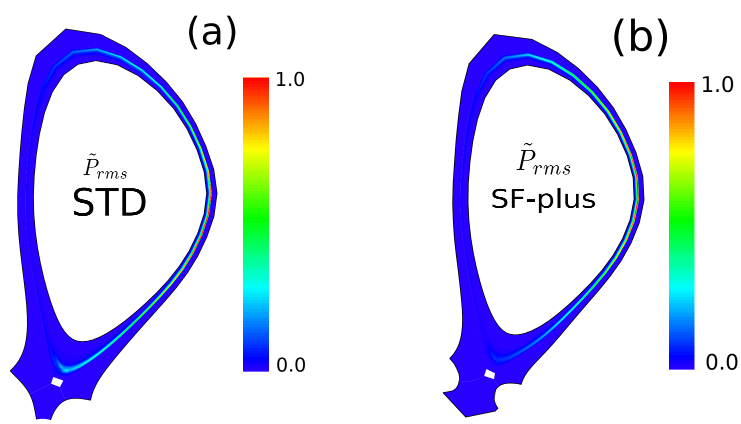

Figure 5.16: Poloidal slice contour of normalized pressure rms perturbation $\tilde{P}_{rms}$ in STD (a) and SF-plus (b) divertor geometry. The P-B mode localizes at outer midplane in both geometries while extends further to divertor region in STD configuration.

5.4.3 Explanation and discussion

From linear simulation results, we find that the growth rate of peeling-ballooning modes in SF-plus divertor configuration is larger than in STD. The mode structure is more radially extended yet less poloidally extended in SF-plus divertor geometry. More importantly, the different characteristics of P-B modes in these two configurations are more evident for high n mode than low n. Having shown these interesting results, we need to investigate the reasons carefully. Considerable efforts have been dedicated to explaining linear behavior of P-B mode and certain parameters have been held responsible, such as pedestal height and gradient (β_p, α_p), edge current (J_0), curvature (κ_0), magnetic shear (s) and so on. Given the identical pressure and current profile in STD and SF-plus geometry, we can exclude these quantities. Magnetic shear and curvature are very likely the reason for the different linear behavior, as from 5.12(b), we can see that the poloidal magnetic field at the outer midplane is different in the pedestal region. Although the direct difference is small, operators such as inverse and derivative required to calculate the magnetic shear and curvature may produce bigger discrepancies. After some analysis of the equilibrium profiles, we found that the local magnetic shear is the dominant factor.

The stabilization mechanism of magnetic shear on ballooning mode has been explored rather throughly in the literature[7]. The conventional formula for global magnetic shear is $S = (r/q)(dq/dr)$, which is a manifest of poloidal averaged separation between magnetic surfaces (showing in 5.17(d)). As useful

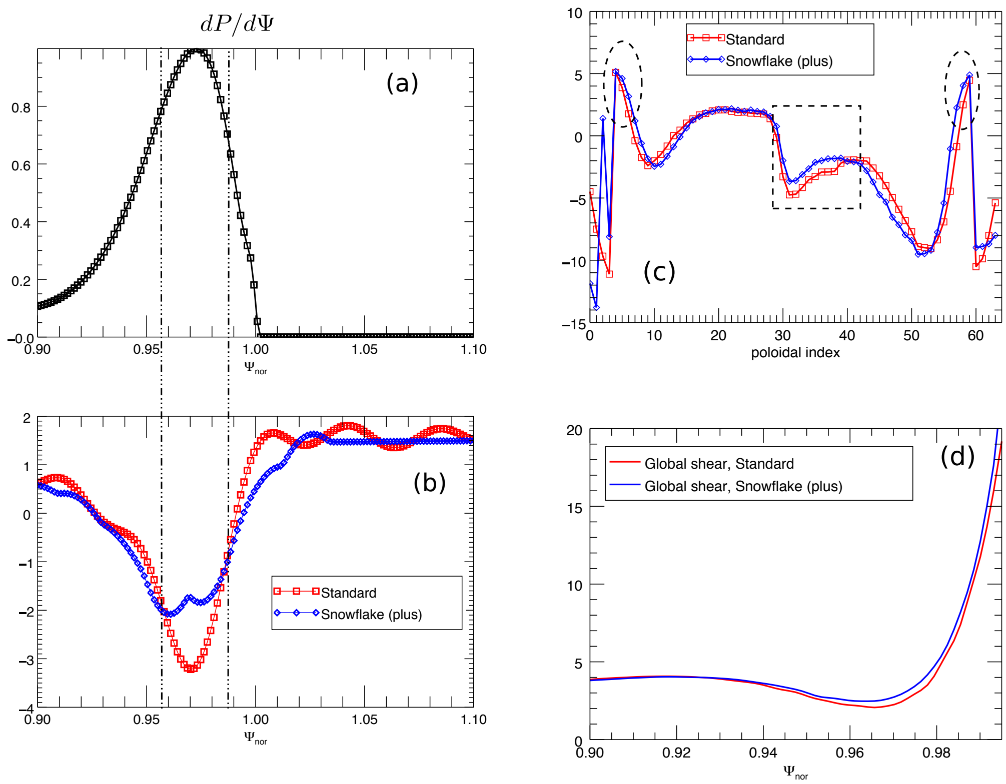

Figure 5.17: *(a)*: Pressure gradient profile $dP/d\Psi$. *(b)*: local magnetic shear (s) in STD (red) and SF-plus (blue) divertor geometry in radial direction. $ny = 38$. *(c)*: local magnetic shear in poloidal direction. $\Psi_{nor} = 0.972$. *(d)*: Global magnetic shear ($S = (r/q)(dq/dr)$) in radial direction.

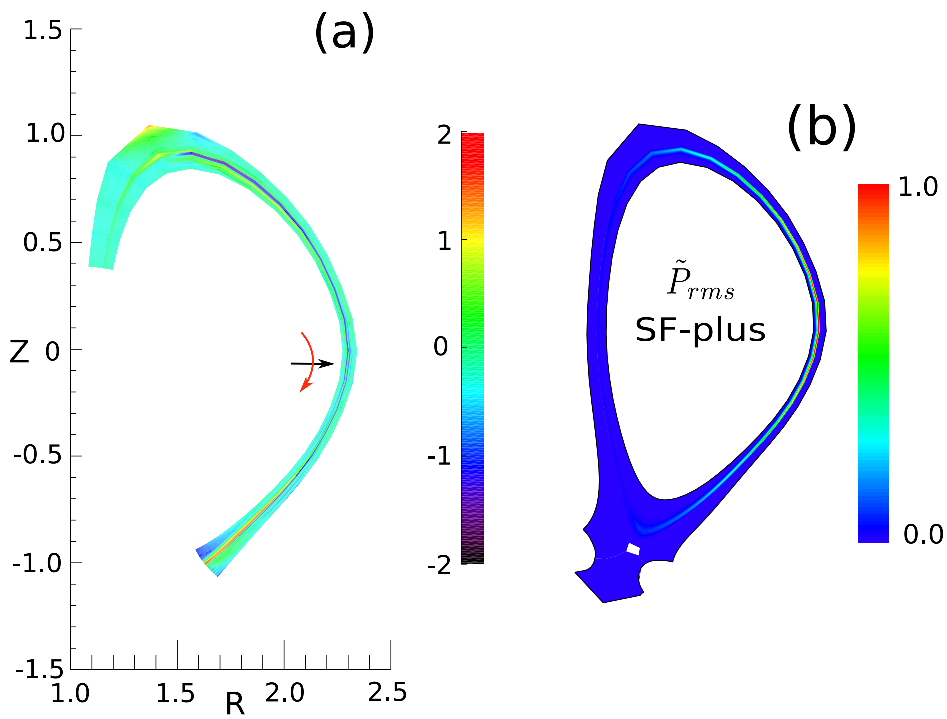

Figure 5.18: *(a)*: Contour plot of the difference of local magnetic shear $|s_{sf}| - |s_{sd}|$ in two dimension (Ψ, θ) domain. $|s_{sf}|$ and $|s_{sd}|$ stands for absolute value of the local magnetic shear in SF-plus and STD configuration. Black and red arrow represents radial and poloidal direction as in 5.17. *(b)*: P-B mode structure contour in SF-plus divertor configuration for reference. The same as 5.16(b).

as it is in many circumstances, we found global magnetic shear is far from adequate to explain the distinctive radial and global mode structures of P-B mode in different divertor configurations. The reason is that it takes into account the magnetic shear around the null point, which is theoretically much larger than the magnetic shear at other poloidal positions and dominates the global magnetic shear. However, as the P-B modes in our simulation are localized at outer midplane, the magnetic shear around that particular position should be more essential. Therefore, we instead define two-dimensional local magnetic shear ($s(\Psi, \theta)$):

$$s = \frac{r}{\nu}\frac{\partial \nu}{\partial r}, \nu = \frac{rB_t}{RB_p} \tag{5.9}$$

where $\nu(\Psi, \theta)$ is local pitch and its flux surface average yields safety factor $q(\Psi) =< \nu >_{sur}$. The comparison of the local magnetic shear in STD and SF-plus divertor geometry is shown in 5.17. 5.17 (b) indicates the difference of local magnetic shear in radial direction at outer midplane. One observation is that local magnetic shear in both geometries is negative in the pedestal region ($0.9 < \Psi_{nor} < 1.0$). This is not surprising because the poloidal magnetic field has been shown to be increasing in the pedestal region in 5.12 (b) due to the large edge current, and a magnetic shear reversal shall happen. Nevertheless, based on the stabilization mechanism, only the absolute value of magnetic shear matters. Therefore, 'local magnetic shear' means the absolute value of the local magnetic shear in the following text, unless otherwise stated. 5.17(a) shows the pedestal pressure gradient profile. Together with 5.17(b), it shows that the local magnetic shear in SF-plus divertor geometry is smaller than in STD in the region around pressure peak gradient position, which is the region between two black dashed lines. As the ballooning modes are driven by the pressure gradient, the mode structure is mainly localized in this region. This can also be illustrated from poloidal direction as shown in 5.17(c), where dashed rectangle roughly represents the outer midplane region. Combining these two figures, we find that in the two dimensional domain ($0.96 < \Psi_{nor} < 0.99, 30 < ny < 43$) where the P-B mode is mainly localized, the local magnetic shear in SF-plus geometry is smaller than that in STD. This explains larger growth rate and broader radial structure of ideal P-B mode in SF-plus configuration as in 5.13 and 5.15(a). More clearly, the difference of local magnetic shear ($|s_{sf}| - |s_{sd}|$) in two dimensional view is shown in 5.18(a). 5.18(b) shows the ideal P-B mode structure in SF-plus divertor geometry for reference.

In addition, area circled by dashed oval in 5.17(c) indicates that the magnetic shear near the null point is indeed larger in SF-plus divertor geometry. One of the most distinctive characteristic of the snowflake divertor is that the poloidal magnetic field has a second-order null around the null point instead of first-order as in standard single-null divertor. According to equation 5.17, we easily obtain the following scaling law:

$$STD\ divertor: \quad B_p \sim \Delta r, s \sim (\Delta r)^{-2} \tag{5.10}$$

$$SF-plus\ divertor: \quad B_p \sim (\Delta r)^2, s \sim (\Delta r)^{-3} \tag{5.11}$$

where Δr is the distance from the null point. Although this scaling law is only rigorously correct for the perfect snowflake geometry, the comparative results that it gives are still valid for snowflake-like geometries. If we assume that the poloidal magnetic field close to the null-point is scaled as $B_p \sim (\Delta r)^k$, then $k = 1$ represents the standard single-null case, in which distance (d) between two null points is infinity, and $k = 2$ represents perfect snowflake case, in which $d = 0$. Therefore, for a snowflake-like geometry where d is finite ($d = 25$cm in our case), $1 < k < 2$ and the local magnetic shear around the null point is still larger than standard divertor geometry. This property of SF-plus divertor explains why the P-B instability is suppressed in divertor region as in 5.15(b).

We have shown that local magnetic shear plays an important role in governing the linear behavior of the P-B mode in our simulations. However, we still need to solve the question of why the difference between STD and SF-plus divertor becomes more obvious as the toroidal mode number is increased. It is known that the peeling-ballooning mode has two drive mechanism, pedestal pressure gradient (ballooning) and edge current (peeling), among which dominate drive term may vary for different n. As the magnetic shear mainly stablizes the pressure gradient drive mode, i.e. the ballooning mode, dominant drive mechanism needs to be determined for different toroidal mode numbers. In equation(5.1), pressure gradient drive and edge current-gradient drive terms (also known as the kink term) are represented by $2\boldsymbol{b_0} \times \kappa_0 \cdot \nabla \tilde{p}$ and $B_0 \tilde{\boldsymbol{b}} \cdot \nabla J_{\|0}$ respectively. Without involving other complexities and focusing only on solving this problem, we simply turn off the kink term and compute growth rate

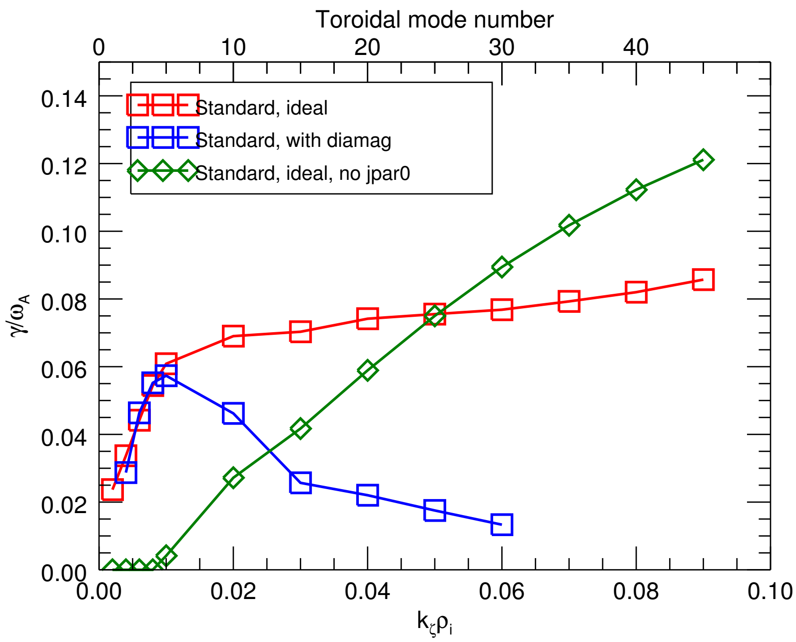

Figure 5.19: *(a)*: The growth rate of ideal peeling-ballooning mode (red), peeling-ballooning mode with ion diamagnetic effects (blue) and ideal ballooning mode (green) in standard divertor configuration.

in STD divertor geometry. The results are shown in 5.19. It is found that current-gradient drive dominates low n mode, especially for $n < 5$, while ballooning mode become more and more pronounced for $n > 25$. This conclusion appears to explain the evident difference of linear behavior of the P-B mode between STD and SF-plus divertor configurations for higher toroidal mode number. Besides, the ion diamagnetic effects have been shown to stabilize the P-B mode for $n > 5$, but yield no differences for $n < 5$ in both geometries in 5.13. Because stabilization effects of ion diamagnetic drifts work mainly for the ballooning mode, these two conclusions are consistent. Moreover, as ELM bursts are often triggered by P-B mode at intermediate n $(3 < n < 20)$, dominant peeling mode at this range explains the large ELM size $(72kJ)$ measured in reference [18].

5.4.4 Conclusion

In this section, we have presented the linear simulation results of the coupled peeling-ballooning mode in the pedestal region of standard single-null and snowflake plus divertor configurations. A two-fluid, three-field MHD model has been used in BOUT++ simulations. We have found that in an SF-plus divertor configuration, the growth rate of the P-B modes are higher and the radial mode structures are broader. Besides, the peeling-ballooning instability is stabilized around the null point in the SF-plus divertor geometry. Further studies have indicated that the distinctive linear behavior of the P-B modes in these two configurations are primarily governed by the local magnetic shear, instead of global magnetic shear. We have found that the larger magnetic shear around the null point in SF-plus divertor suppresses the P-B modes in divertor region, while the smaller magnetic shear at outer midplane causes higher growth rate and broader radial mode structure. As the pressure gradient drive dominates the P-B modes with high n, the difference of linear behavior between these two geometries become more evident for high n.

Although our studies are conducted on a particular snowflake geometry, the impact of the local magnetic shear that we found on the linear behavior of the P-B modes provides some interesting and promising insights for the engineering design of snowflake divertor and other advanced divertors. First of all, we found that the snowflake geometry suppresses the P-B instability around null point due to the large magnetic shear in the divertor region. Secondly, the different linear growth rates and radial mode structures are due to the distinct local magnetic shear at the outer midplane. Unlike the larger magnetic shear around the null point, smaller magnetic shear at the outer midplane is not the inevitable consequence of implementation of snowflake divertor geometry. Instead, it is likely due to the constraints we set for PF and CS coils when generating snowflake equilibrium using reconstruction algorithm. The different current density in PF and CS coils may change magnetic shear by directly altering magnetic field at the outer midplane, like in our case, or by affecting geometric properties, such as triangularity, elongation and so on.

Nevertheless, multiple sets of PF and CS coils may exist for the similar snowflake divertor configurations and their influences on the magnetic topology at the outer midplane of tokamak may be diverse. Therefore, one may ideally assume that , with a particular constraint of PF and CS coils, the snowflake divertor geometry can be implemented such that the stabilization of the P-B modes and the scenario of the ELM bursts are not affected while the benefits of reducing heat load on divertor plates are retained. We have made considerable efforts to modify the PF and CS coils in our case, aiming to achieve this goal. However, we found that it is difficult to eliminate the small changes of the local magnetic shear around the outer midplane. Fortunately, in contrast to the case in this paper, these changes could also be beneficial to the stabilization of the P-B modes with specified constraints. Our studies choose a typical case to demonstrate the sensitivity of the linear behaviors of P-B modes on the small changes of the local magnetic shear at the outer midplane. This is of great importance to the design of advanced divertors on the tokamak, for various experiments have shown that ELM size increases on TCV, but decreases on DIII-D after implementing advanced divertor geometry, which could imply the opposite behaviors of the P-B modes in the linear stage. The local magnetic shear can be used as a useful criteria to predict the linear behavior of P-B mode and the following ELM bursts, even in standard singe-null divertor geometry.

Chapter 6

The micro-instabilities in the pedestal region: The Drift-Alfven modes

6.1 Theoretical analysis of the Drift-Alfven instability

Pressure gradient driven drift waves with the presence of the inhomogeneous magnetic field have attracted attentions for decades. In this section, We start from the density gradient driven electromagnetic drift-Alfven model based on the famous Hasegawa-Wakatani model, and then extend to the pressure gradient driven model with temperature variations. Theoretical dispersion relations are derived and the numerical results calculated by Mathematica. The main purpose of this study is to find theoretical basis for the simulation results using BOUT++ later and to make qualitative benchmark with these results.

6.1.1 Density gradient driven drift-Alfven model

Having shown in Hasagawa-Wakatani model, the drift waves can be driven unstable with the presence of the parallel electron dissipation (collision), we now couple the electrostatic drift waves equations with the parallel vector potential equations, switching to the electromagnetic model. The equation set is:

$$\frac{m_i n_i}{B^2}\frac{d}{dt}\nabla_\perp^2\phi - \nabla_\parallel J_\parallel = 0 \tag{6.1}$$

$$\frac{\partial n}{\partial t} + \frac{\boldsymbol{b}\times\nabla\phi}{B}\cdot\nabla n - \frac{\nabla_\parallel J_\parallel}{e} = 0 \tag{6.2}$$

$$\frac{\partial A_\parallel}{\partial t} + \nabla_\parallel\phi - \frac{T_{e0}}{en}\nabla_\parallel n + \frac{m_e\nu_e}{e^2 n}J_\parallel = 0 \tag{6.3}$$

in which, $J_\parallel = -env_{e\parallel}$ and $J_\parallel = -\nabla_\perp^2 A_\parallel/\mu_0$. The coulomb collision expression is $\nu_e = \frac{4\pi n Z_i e^4 ln\Lambda}{(4\pi\epsilon_0)^2 m_e^2 v_{Te}^3}$Besides, the quasi-neutrality assumption is also retained in this model. In this electromagnetic model, the magnetic perturbation has the expression $\tilde{\boldsymbol{b}} = (\nabla A_\parallel \times \boldsymbol{b_0})/B$. Therefore, the equations can be written in Hamiltonian format (Poisson Brackets).

$$\frac{\partial}{\partial t}\nabla_\perp^2\phi + \left[\phi, \nabla_\perp^2\phi\right]/B - \frac{B^2}{m_i n_i}[(\boldsymbol{b_0}\cdot\nabla)J_\parallel + [J_\parallel, A_\parallel]/B] = 0 \tag{6.4}$$

$$\frac{\partial n}{\partial t} + [\phi, n]/B - [(\boldsymbol{b_0}\cdot\nabla)J_\parallel + [J_\parallel, A_\parallel]/B]/e = 0 \tag{6.5}$$

$$\frac{\partial A_\parallel}{\partial t} + (\boldsymbol{b_0}\cdot\nabla)\phi + [\phi, A_\parallel]/B - \frac{T_{e0}}{en}((\boldsymbol{b_0}\cdot\nabla)n + [n, A_\parallel]/B) + \frac{m_e\nu_e}{e^2 n}J_\parallel = 0 \tag{6.6}$$

normalization:

$$\tilde{t} = t\omega_{ci}, \tilde{l} = l/\rho_s, \rho_s = c_s/\omega_{ci}, \tilde{\phi} = e\phi/T_{e0}, \tau_e = \frac{\nu_e m_e}{\omega_{ci} m_i}, L_n = -n_0/(dn_0/dx) \tag{6.7}$$

Linearize the equations

$$n = n_0 + \tilde{n}, \phi = \tilde{\phi}, J_\parallel = \tilde{J}_\parallel = -\nabla_\perp^2/\mu_0 \tag{6.8}$$

assuming $\{\tilde{n}, \tilde{\phi}, \tilde{A}_\parallel\} \sim \exp(-\boldsymbol{i}\omega t - \boldsymbol{i}\boldsymbol{k}\cdot\boldsymbol{r})$, we can get the dispersion relation for the local modes:

$$\frac{c_s^2}{v_A^2}\frac{\omega^3}{k_\parallel^2} + \boldsymbol{i}\tau_e\frac{k_\perp^2}{k_\parallel^2}\omega^2 - (1 + k_\perp^2)\omega + \frac{k_y}{L_n} = 0 \tag{6.9}$$

From the dispersion relation:

- if we only focus on the parallel motion and let $k_\perp = 0$, the dispersion relation is thus degenerated to the famous shear Alfven wave dispersion relation(SAW): $\omega^2 = k_\parallel^2 v_A^2$

- if the parallel collision is very small or even zero ($\tau_e << 1$), the dispersion relation becomes:

$$\frac{c_s^2}{v_A^2}\frac{\omega^3}{k_\parallel^2} - (1 + k_\perp^2)\omega + \frac{k_y}{L_n} = 0 \tag{6.10}$$

  where the drift waves are excited by the shear Alfven waves and are the electromagnetic branch.

- if the parallel collision is very large ($\tau_e >> 1$), then the cubic term becomes less important and the dispersion relation becomes:

$$k_\perp^2\omega^2 + (\boldsymbol{i}/\tau_e)k_\parallel^2(\omega(1 + k_\perp^2) - \frac{k_y}{L_n}) = 0 \tag{6.11}$$

  which is the classic Hasegawa-Wakatani electrostatic drift wave dispersion relation.

- if the value of the parallel collision falls between the previous two cases, then the dispersion relation will contain both the electrostatic and electromagnetic branches simultaneously.

Without the loss of generality, we set the following parameters according to the pedestal region of the Tokamak:

$$\frac{c_s^2}{v_A^2} = 0.01, L_n \sim \rho_s, k_\perp^2 \approx 36 k_\parallel^2 \tag{6.12}$$

First, we let $\tau_e = 0$ and focus on the electromagnetic branch of the Drift-Alfven waves. As shown in figure (6.1), there are three modes corresponding to the cubic dispersion relation function. The first mode has no growth rate and the real frequency is proportional to the wave number. Thus, the first mode is the shear Alfven wave, propagating along magnetic field lines (parallel direction). The other two modes, have almost the same real frequency, which is also proportional to the wave number, but the opposite growth rate. These two modes are the electromagnetic branches of the Drift-Alfven modes. The real frequency of these two modes is approximately half of the shear Alfven frequency. Having shown the characteristics of the Drift-Alfven with the absence of parallel dissipation, we now retain the full dispersion relation equation and vary the parallel collisionality (τ_e). The results with $\tau_e = 0.01, 0.1, 1.0$ are shown in figure (6.2). There are several important features that we can find in this figure:

- When the parallel collisionality becomes finite but very small ($\tau_e = 0.01$), the SAW branch becomes decaying mode, with almost the same real frequency as collisionless case. The other two drift wave branches also begin to shift in both real frequency and growth rate.

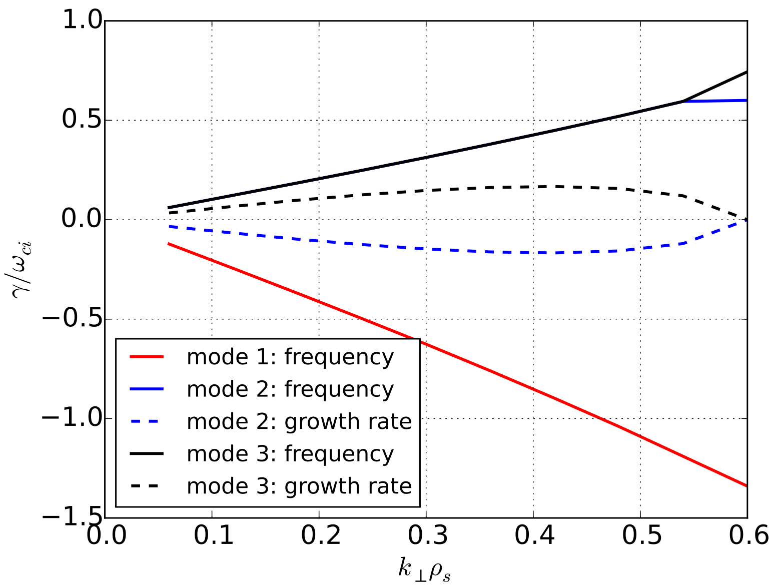

Figure 6.1: The dispersion relation of the electromagnetic branch of the Drift-Alfven wave, $\frac{c_s^2}{v_A^2} = 0.01, L_n \sim \rho_s, k_\perp^2 \approx 36 k_\parallel^2$

.

- When the parallel collisionality becomes large enough ($\tau_e = 1.0$), a rapidly decaying branch with no real frequency appears, which is likely the MHD mode. Besides, another two branches shows mirror-like characteristics in both real frequency and growth rate. In addition, the real frequency is proportional to the perpendicular wave numbers. These are the main characteristics of the electrostatic drift waves. However, with the impact of shear Alfven waves, the mode will saturate at very high mode numbers ($k_\perp \rho_s \approx 1.8$)

- The branches show the transient features for the intermediate parallel collisionality ($\tau_e = 0.1$).

Figure (6.3) shows the real frequency and growth rate of the Drift-Alfven waves versus the parallel collisionality. When the background density gradient is large enough ($L_n = 1.0$, unstable for $\nu_e = 0$), we can find that both the real frequency and the growth rate of the growing branch decreases monotonically as the parallel collisonality increases. However, when the density gradient is mild ($L_n = 5.0$, stable for $\nu_e = 0$), the real frequency still monotonically decreases but the growth rate first increases then decreases as the parallel collisionality increases. The latter case is consistent with the electrostatic Hasegawa-Wakatani model. Figure (6.4) shows that the growth rate of the growing mode increases as the background density gradient increases, and the critical scale length for this particular case is around $L_{nc} = 1.6$.

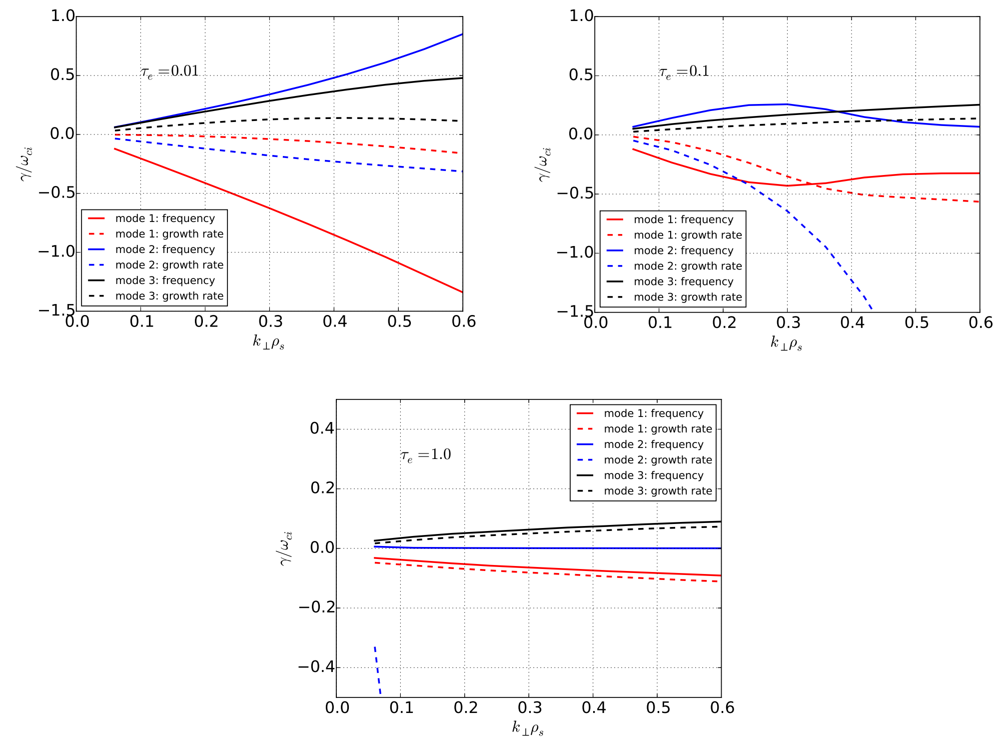

Figure 6.2: The dispersion relation of the Drift-Alfven modes for different parallel collisionality (τ_e), the other parameters are the same as in figure 6.1

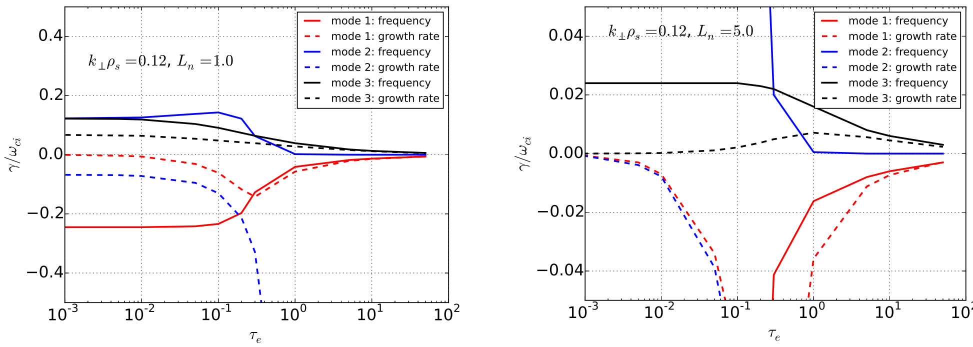

Figure 6.3: The growth rates and real frequencies of the three branches for different parallel collisonality (τ_e). The perpendicular wave number is fixed as $k_\perp \rho_s = 0.12$. The density scale length is set to be 1.0 and 5.0 in left and right figure respectively. The other parameters are the same as in figure 6.1.

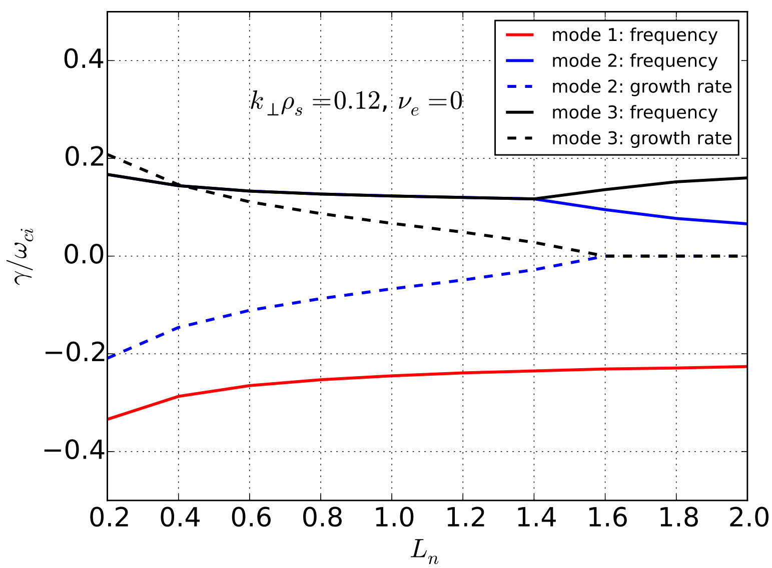

Figure 6.4: The growth rate and real frequency of the three branches for different background density scale length. The parallel dissipation is set to be $\nu_e = 0$ and the perpendicular wave number is $k_\perp \rho_s = 0.12$. Other parameters are the same as in figure 6.1

.

6.1.2 Pressure gradient driven drift-Alfven model

The previous model utilizes the minimum set of the equations to demonstrate that the drift waves can be destabilized by the shear Alfven waves in uniform background magnetic field. Therefore, we set electron temperature to be constant and only focused on the density gradient effects. However, in the pedestal region of a H-mode discharge, usually the scale length of the electron temperature profile is one order of magnitude smaller than that of the electron density profile. It is essential to add the temperature gradient terms in the previous equations:

$$\frac{\partial \tilde{T}_e}{\partial t} + \frac{\boldsymbol{b} \times \nabla \tilde{\phi}}{B_0} \cdot \nabla T_{e0} - \frac{2}{3} \frac{T_{e0}}{e n_0} \nabla_\parallel \tilde{J}_\parallel = 0 \tag{6.13}$$

and the Ohm's Law equation will be changed to:

$$\frac{\partial \tilde{A}_\parallel}{\partial t} + \nabla_\parallel \tilde{\phi} - \frac{T_{e0}}{e n_0} \nabla_\parallel \tilde{n} - \frac{1}{e} \nabla_\parallel \tilde{T}_e + \frac{m_e \nu_e}{e^2 n_0} \tilde{J}_\parallel = 0 \tag{6.14}$$

The vorticity and electron density equations will be

$$\frac{m_i n_0}{B_0^2} \frac{\partial}{\partial t} \nabla_\perp^2 \tilde{\phi} - \nabla_\parallel \tilde{J}_\parallel = 0 \tag{6.15}$$

$$\frac{\partial \tilde{n}}{\partial t} + \frac{\boldsymbol{b} \times \nabla \tilde{\phi}}{B_0} \cdot \nabla n_0 - \frac{\nabla_\parallel \tilde{J}_\parallel}{e} = 0 \tag{6.16}$$

The similar linear local analysis gives the dispersion relation:

$$\frac{c_s^2}{v_A^2} \frac{\omega^3}{k_\parallel^2} + \boldsymbol{i} \tau_e \frac{k_\perp^2}{k_\parallel^2} \omega^2 - (1 + \frac{5}{3} k_\perp^2) \omega + k_y \left(\frac{1}{L_n} + \frac{1}{L_{Te}} \right) = 0 \tag{6.17}$$

as $\frac{1}{L_n} + \frac{1}{L_{Te}} = \frac{1}{L_{Pe}}$, we can see that this dispersion relation equation differs from equation 6.9 only by the coefficient of $k_\perp^2$ in the third term and the scale length in the last term. Therefore, the drift-Alfven modes are driven by both electron density and temperature gradient. One thing that need to be noticed is that the ion temperature equation

$$\frac{\partial \tilde{T}_i}{\partial t} + \frac{\boldsymbol{b} \times \nabla \tilde{\phi}}{B_0} \cdot \nabla T_{i0} = 0 \tag{6.18}$$

will be passive to the four equations (6.13, 6.14, 6.15, 6.16) and the ion temperature gradient will not have direct impact on the drift-Alfven modes.

6.2 The simulations of the Drift-Alfven modes in the pedestal region of the Tokamak

In this section, the pressure scan equilibria generated by the 'VARYPED' tool, which are used in BOUT++ simulations, are presented in details. Then the linear peeling-ballooning threshold is calculated using the reduced-MHD three-field model in BOUT++ as before. After that, the modified five-field landau-fluid model are employed to study the linear characteristics of the drift-Alfven modes and the qualitative comparisons to the theoretical results are made. Finally, the heat transports induced by the drift-Alfven turbulence in the pedestal are presented using BOUT++ nonlinear simulation results.

6.2.1 The pressure scan equilibria

The pressure scan equilibria we used in this paper are based on DIII-D H-mode discharge 132016, which has plasma current of 1.5 MA, toroidal field of 2.13 T and an average triangularity of 0.55. The experimental equilibrium represents the 75-99% portion of the ELM cycle and is the state of the stable plasma with the marginal conditions of the ELM onset. Based on this equilibrium, we vary the pedestal pressure from below to above the measured profile using the VARYPED tool, which allows for a series of EFITs to be produced with variation in the pedestal characteristics. In this case, the highest and lowest variation of the pressure profile are 250% and 50% of the original one, corresponding to $\beta = 2.5\%$ and $\beta = 0.5\%$. The cross-sectional shape, total stored energy and the total plasma current are kept the same for all the variations. In addition, the width of the pressure profiles stays the same, while the height and offset varies. The definition of height, width and offset of the profiles in the pedestal region comes from [27]. As a result, the parameter $\eta_i = L_{n_i}/L_{T_i}$ is the same for all equilibria ($\eta_i = 2.68$ at peak gradient radial position). Figure (6.5) shows some of the radial pedestal profiles ($0.9 < \Psi_{nor} < 1.05$) at the outboard midplane of the equilibria, including pressure, edge current density, density, temperature, safety factor and collisionality. As the differences between electron and ion temperature profiles are small, without loss of generality, we set both to be equal to the electron temperature for simplicity. The similar treatments are also done to the density profiles. Also, although the edge current density at the outboard midplane increases as the pedestal pressure gradient increases, the total edge current density keeps the same for different equilibria. The peak pressure gradient radial position is approximately at $\Psi_{nor} = 0.962$.

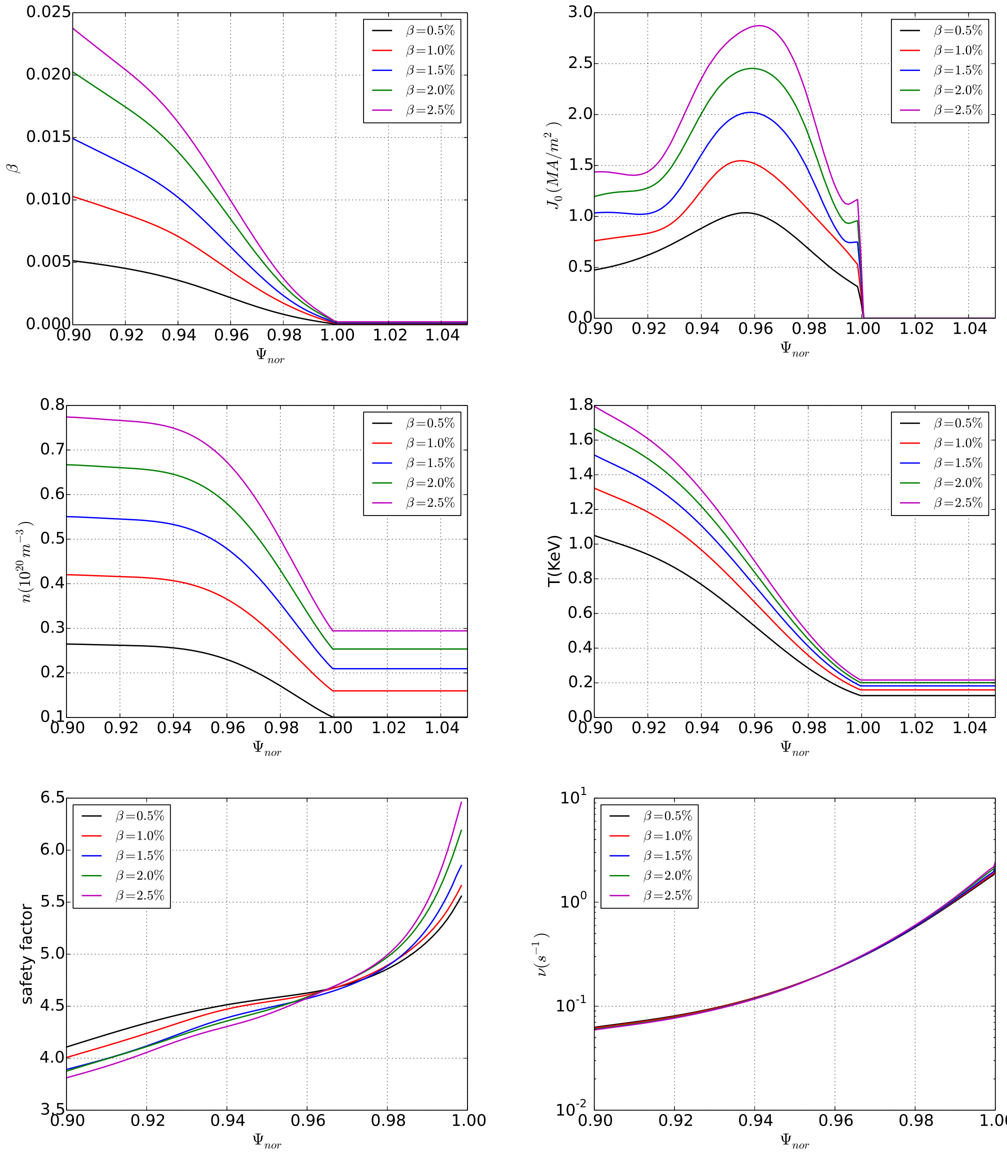

Figure 6.5: The profiles of the 'Varyped' global self-consistent equilibria: Pressure ($\beta = 2\mu_0 P/B^2$) profile at the top left; Edge current density profile at the top right; Ion and electron density profiles at the middle left; Ion and electron temperature profiles at the middle right; The safety factor profile at the bottom left; The edge collisionality at the bottom right.The red line in all figures represent the profiles from the original discharge.

6.2.2 The peeling-ballooning threshold

Before going into the micro-instabilities analysis, we first use reduced-MHD three-field[19] model to study the characteristics of the peeling-ballooning modes in the 'VARYPED' equilibria , which can be used as a reference later. The radial boundary conditions are set as $\tilde{\varpi} = 0, \nabla_\perp^2 \tilde{A}_\parallel = 0, \partial\tilde{p}/\partial\psi = 0$ and $\partial\tilde{\phi}/\partial\psi = 0$ on the inner radial boundary ($\Psi_{nor} = 0.9$), and $\tilde{\varpi} = 0, \nabla_\perp^2 \tilde{A}_\parallel = 0, \tilde{p} = 0$ and $\tilde{\phi} = 0$ on outer radial boundary ($\Psi_{nor} = 1.05$). Besides, the domain is periodic in the parallel coordinate y with a twisted-shift condition to simulate the continuous field lines. As FFT is used in z direction, periodic boundary condition is also applied on this direction. Moreover, we set Dirichlet boundary condition for all variables on the divertor plates, i.e. we assume no fluctuations there.

The linear simulation results of the peeling-ballooning modes are shown in figure (6.6). The left top figure shows the growth rate of the peeling-ballooning modes with respect to the toroidal number n. We can see that there are no unstable peeling-ballooning modes when the pedestal height $\beta < 2.0\%$. This is consistent with the experimental measurements that the original experimental profile with $\beta = 1.0\%$ is measured right before the ELM crash, i.e., the stage when the plasmas are stable. Besides, the growth rate roughly saturates at $n > 40$. The left bottom figure shows the growth rate of the peeling-ballooning modes at $n = 100$ versus the pedestal height. It is clear that the growth rate of the peeling-ballooning modes increase while the pedestal height increases, until the maximum growth rate is reached at $\beta \approx 2.1\%$. Then a decreasing trend of the growth rate appears as the pedestal height keep increasing. Therefore, the threshold of the peeling-ballooning modes in this case is roughly $\beta = 1.5\%$ for $n = 100$. Moreover, the sensitivity studies demonstrate that the current resolution $n_x = 260$ and $n_y = 64$ is good enough for the linear analysis. These results are consistent with the BALOO infinite-n ballooning modes calculations. The right figures shows the typical ballooning structure, with the mode localized at the outboard midplane of the tokamak.

6.2.3 The linear behaviors of the Drift-Alfven modes

The linear simulations are mainly conducted on the Edison Cray X30 supercomputer at National Energy Research Scientific Center (NERSC). We use a non-orthogonal field-aligned coordinate system with shifted radial derivatives, where (x, y, z) labels magnetic surface, distance along magnetic field line and toroidal angle. Some of the computing grids in our simulations are shown in figure (6.7). For linear simulation, the computing domain is $0.9 < \Psi_{nor} < 1.05$ in radial direction, $0 < \theta < 2\pi$ in poloidal direction and $1/n$ the whole torus, where n is the toroidal mode number. The resolution in this three directions are set as: $n_x = 132, n_y = 64, n_z = 17$. Particularly, in order to include the divertor region in the simulation, we add the private flux region to the computing grid, the detail of which can be found in [89].

The spatial discretization schemes are finite differencing in x and y directions, and Fast-Fourier Transformation (FFT) in the z direction. For the partial differential equations, the fourth order central differencing method is adopted for

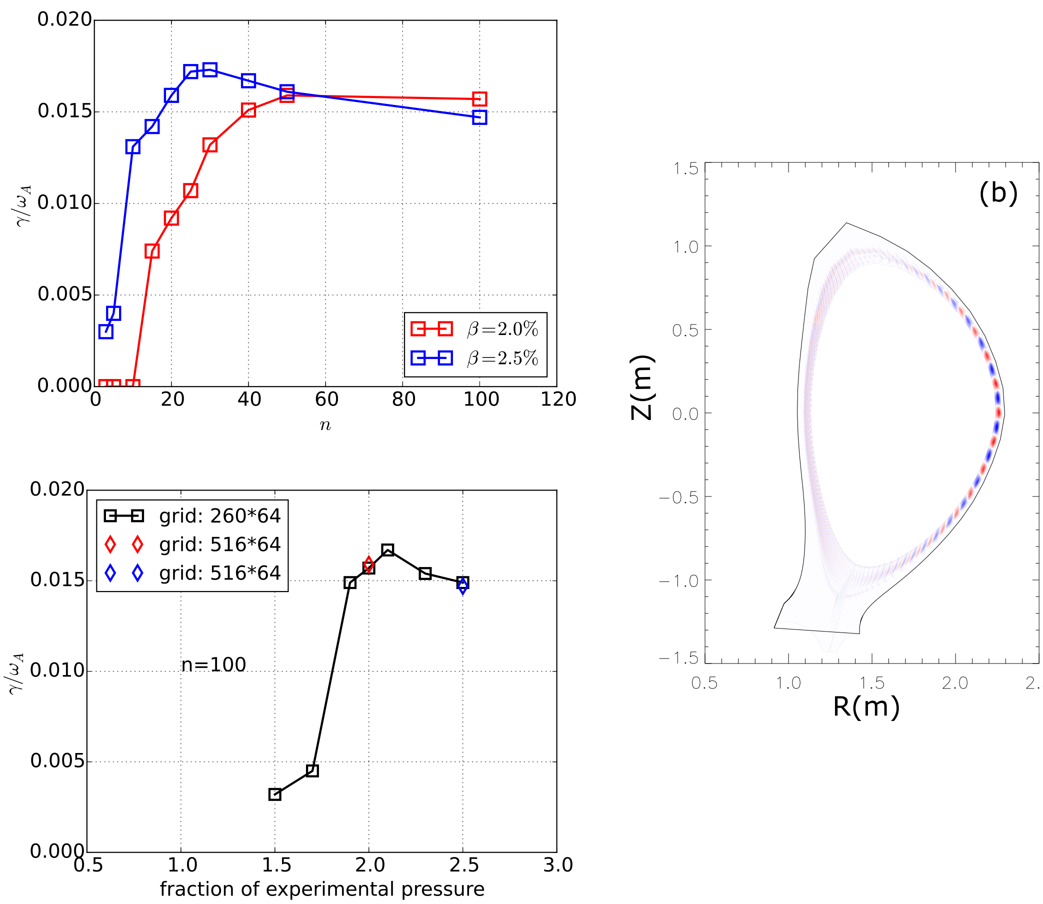

Figure 6.6: The linear simulation results of the peeling-ballooning modes in the pedestal region using ideal reduced-MHD model. The left two figures show the spectrum of the peeling-ballooning modes versus toroidal mode number (left top) and the pedestal height (left bottom). The right figure shows the poloidal section plot of the peeling-ballooning mode with $\beta = 2.0\%, n = 20, t = 200t_A$.

the first and second order derivatives, while the WENO method is used for the convective terms. For the temporal evolution, a fully implicit Newton-Krylov solver PVODE is used with the self-adaptive time-step.

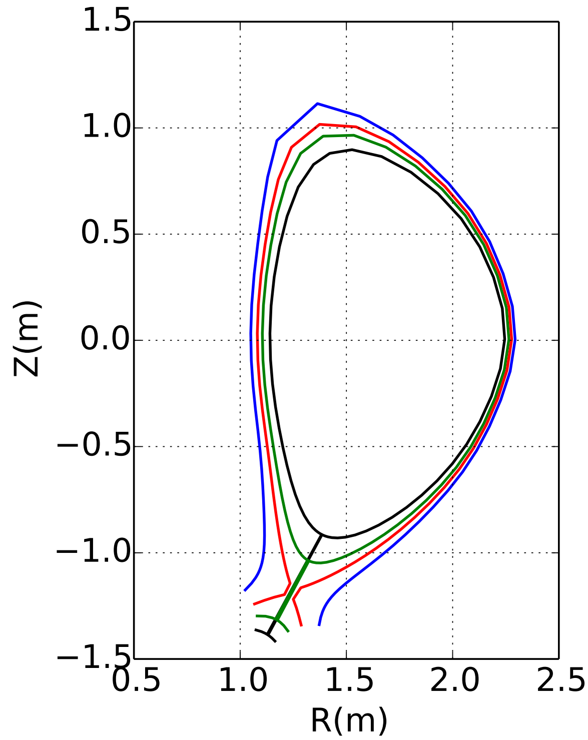

Figure 6.7: Some of the simulation grids are shown: Ψ_{nor} = 0.9 (Black), Ψ_{nor}=0.96 (Green), Ψ_{nor} = 1.00 (Red) and Ψ_{nor} = 1.05 (Blue).

6.2.3.1 The six-fields Landau-fluid model

The six-field Landau-fluid model is based on the original six-fields two-fluid model[84] and modified by adding a parallel Landau closure to the temperature equations. The six fields that evolve with time are vorticity (ϖ), ion density (n_i), ion parallel velocity ($V_{\|i}$), parallel vector potential ($A_\|$), ion temperature (T_i) and electron temperature (T_e).

$$\begin{aligned}
\frac{\partial \varpi}{\partial t} =& -\left(\frac{\boldsymbol{b}\times\nabla_\perp\phi}{B_0}+V_{\|i\boldsymbol{b}}\right)\cdot\nabla\varpi + B^2\nabla_\|\left(\frac{J_\|}{B}\right)+2\boldsymbol{b}\times\boldsymbol{\kappa}\cdot\nabla P \\
&-\frac{1}{2\Omega_i}\left[\frac{\boldsymbol{b}\times\nabla P_i}{B}\cdot\nabla(\nabla_\perp^2\phi)-Z_ieB\boldsymbol{b}\times\nabla n_i\cdot\nabla\left(\frac{\nabla_\perp^2\phi}{B}\right)^2\right] \\
&+\frac{1}{2\Omega_i}\left[\frac{\boldsymbol{b}\times\nabla\phi}{B}\cdot\nabla(\nabla_\perp^2 P_i)-\nabla_\perp^2\left(\frac{\boldsymbol{b}\times\nabla\phi}{B}\cdot\nabla P_i\right)\right]+\mu_{\|i}\nabla_{\|0}^2\varpi
\end{aligned} \tag{6.19}$$

$$\begin{aligned}
\frac{\partial n_i}{\partial t} =& -\left(\frac{\boldsymbol{b}\times\nabla_\perp\phi}{B_0}+V_{\|i}\boldsymbol{b}\right)\cdot\nabla n_i-\frac{2n_i\boldsymbol{b}\times\boldsymbol{\kappa}}{B}\cdot\nabla\phi-\frac{2\boldsymbol{b}\times\boldsymbol{\kappa}}{Z_ieB}\cdot\nabla P \\
&-n_iB\nabla_\|\left(\frac{V_{\|i}}{B}\right)
\end{aligned} \tag{6.20}$$

$$\frac{\partial V_{\|i}}{\partial t} = -\frac{\boldsymbol{b}\times\nabla_\perp\phi}{B_0}\cdot\nabla n_i-\frac{\boldsymbol{b}\cdot\nabla P}{m_in_i} \tag{6.21}$$

$$\frac{\partial A_\|}{\partial t} = -\nabla_\|\phi+\frac{\nabla_\| P_e}{en_e}+\frac{\eta}{\mu_0}\nabla_\perp^2 A_\|-\frac{\eta_H}{\mu_0}\nabla_\perp^4 A_\| \tag{6.22}$$

$$\begin{aligned}
\frac{\partial T_i}{\partial t} =& -\frac{2}{3}T_i\left[\frac{2\boldsymbol{b}\times\boldsymbol{\kappa}}{B}\cdot\left(\nabla\phi+\frac{\nabla P_i}{Z_ien_i}+\frac{5k_B\nabla T_i}{2Z_ie}\right)+B\nabla_\|\left(\frac{V_{\|i}}{B}\right)\right] \\
&-\left(\frac{\boldsymbol{b}\times\nabla_\perp\phi}{B_0}+V_{\|i}\boldsymbol{b}\right)\cdot\nabla T_i-\frac{2\nabla_\| q_i}{3n_ik_B}+\frac{2m_eZ_i}{m_i\tau_e}(T_e-T_i)
\end{aligned} \tag{6.23}$$

$$\frac{\partial T_e}{\partial t} = -\frac{2}{3}T_e\left[\frac{2\boldsymbol{b}\times\boldsymbol{\kappa}}{B}\cdot\left(\nabla\phi + \frac{\nabla P_e}{Z_i e n_i} + \frac{5k_B\nabla T_e}{2Z_i e}\right) + B\nabla_\parallel\left(\frac{V_{\parallel e}}{B}\right)\right]$$
$$-\left(\frac{\boldsymbol{b}\times\nabla_\perp\phi}{B_0} + V_{\parallel e}\boldsymbol{b}\right)\cdot\nabla T_i - \frac{2\nabla_\parallel q_e}{3n_i k_B} + \frac{2m_e Z_i}{m_i \tau_e}(T_e - T_i)$$
$$+\frac{2\eta_\parallel J_\parallel^2}{3n_e k_B} \tag{6.24}$$

The notations are quite similar to the reduced-MHD model, with the exceptions below:

$$\varpi = \frac{n_0 M_i}{B_0}\left(\nabla_\perp^2\tilde{\phi} + \frac{1}{n_{i0}}\nabla_\perp\phi\cdot\nabla_\perp n_{i0} + \frac{1}{n_0 Z_i e}\nabla_\perp^2\tilde{p}_i\right) \tag{6.25}$$

$$V_{\parallel e} = V_{\parallel i} + \frac{1}{\mu_0 Z_i e n_i}\nabla_\perp^2 A_\parallel \tag{6.26}$$

The parallel Landau closure enters the set of equations from ion and electron heat flux in equations (6.23) and (6.24). We use the collisionless formula from Ott and Sudan (1969)[51] and Hammett and Perkins (1990)[30].

$$q_{\parallel i} = -n_0\sqrt{\frac{8}{\pi}}v_{T_{\parallel i}}\frac{ik_\parallel k_B T_i}{|k_\parallel|} \tag{6.27}$$
$$q_{\parallel e} = -n_0\sqrt{\frac{8}{\pi}}v_{T_{\parallel e}}\frac{ik_\parallel k_B T_e}{|k_\parallel|} \tag{6.28}$$

One thing that needs to be noticed is that a new Non-Fourier algorithm has been developed and implemented in BOUT++ framework[11]. The Non-Fourier method keeps the accuracy and efficiency as the traditional Fourier ones, but yields much stronger capability in handling the spatial non-uniformity.

Besides the Landau closure, the lowest-order Finite Larmor Radius (FLR) effects are also retained in the vorticity equation (6.19) as ion diamagnetic drift and gyro-viscosity. The electron toroidal resonance, which is also believed to be an important kinetic effect besides the Landau damping and the FLR, is currently not included in the equation set due to technical issues.

In the drift-Alfven mode simulations, the parallel ion velocity ($V_{\parallel i}$) equation (6.21) is turned off and the curvature terms ($\boldsymbol{b} \times \boldsymbol{\kappa}$) are also turned off to prevent the mixing of the curvature driven interchange-type modes. Therefore, the model we use is actually the modified five-field Landau-fluid model, evolving vorticity (ϖ), ion density (n_i), parallel vector potential ($A_{\parallel}$), ion temperature (T_i) and electron temperature (T_e). We can see that after modifications, the equations that we use for BOUT++ simulations are almost the same as that we used for theoretical studies (Eqs 6.13, 6.14, 6.15, 6.16 and 6.18). Therefore, qualitative comparisons are possible for verification purposes.

6.2.3.2 The growth rate and real frequency

The growth rate and real frequency of the drift-Alfven modes for the experimental profile ($\beta = 1.0\%$) is shown in figure (6.8). We found that the growth rate and real frequency increases with the toroidal mode number for $n < 50$. The drift-Alfven modes propagate in the electron diamagnetic direction and the real frequency is approximately linearly scaled with the toroidal mode number, which is consistent with the analytical results (figure 6.1) of the drift-Alfven modes. Moreover, the drift-Alfven modes with larger resistivity ($S = 1 \times 10^6$) have the smaller growth rate and real frequency. This result can also be demonstrated directly in the resistivity scan study (figure 6.9), where the normalized resistivity is varied by five orders of magnitude (from 1×10^{-10} to 1×10^{-5}). A comprehensive sensitivity study of the radial resolution is also conducted and the results are shown in figure (6.9). The study includes both the equilibrium grid with ($0.9 < \Psi_{nor} < 1.05$) and without ($0.9 < \Psi_{nor} < 0.999$) the separatrix, with the radial resolution variation from $n_x = 128$ to $n_x = 516$. The right figure in figure (6.8) shows that the maximum relative deviation between these cases is less than 10%.

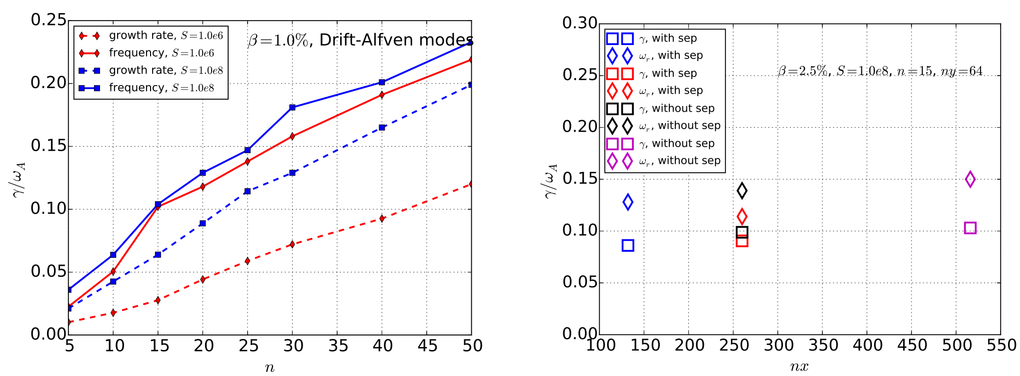

Figure 6.8: *Left figure*: The growth rate and real frequency versus the toroidal mode number, with normalized lundquist number $S = 1 \times 10^6$ and $S = 1 \times 10^8$. $\beta = 1.0\%$; *Right figure*: The sensitivity scan of the radial grid resolution, the poloidal resolution is $n_y = 64$. $n = 15$.

The impact of the pedestal height on the drift-Alfven modes is shown in figure (6.10). The growth rate strictly increases as the pedestal height increases self-consistently, while the real frequency shows a small dip at $\beta = 2.0\%$ along with the increasing trend. As both the ion and electron temperature

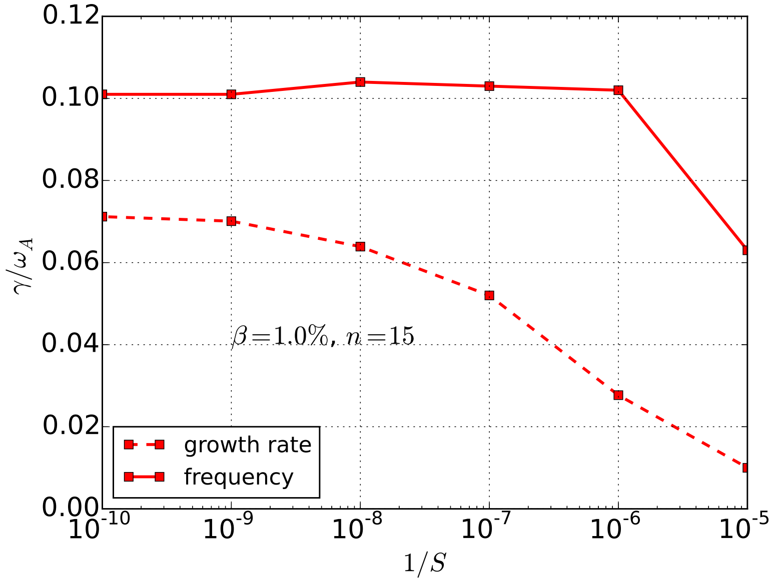

Figure 6.9: The growth rate and real frequency versus the normalized resistivity. $\beta = 1.0\%$, $n = 15$.

gradient increases as the pedestal height increases, it is crucial to figure out the primary free energy source of the drift-Alfven modes. In order to do that, we decrease the ion and electron temperature gradient separately by multiplying the original profiles by the gradient coefficient, which ranges from 0.1 to 1.0. The results are shown in the right figure of figure (6.10). The growth rate dramatically decreases as the electron temperature gradient is decreases and drops to zero when the electron gradient becomes 40% of the original one. In contrast, only 10% reduction appears when the ion temperature gradient is decreased to 20%. Therefore, we can determine that the free energy for the drift-Alfven instability comes from the electron temperature gradient in the pedestal region. As the previous analytical study shows that the drift-Alfven instability is determined by the inverse of the electron pressure solely (figure 6.4, Eq 6.17), we have obtained qualitatively consistent results from theoretical and numerical studies.

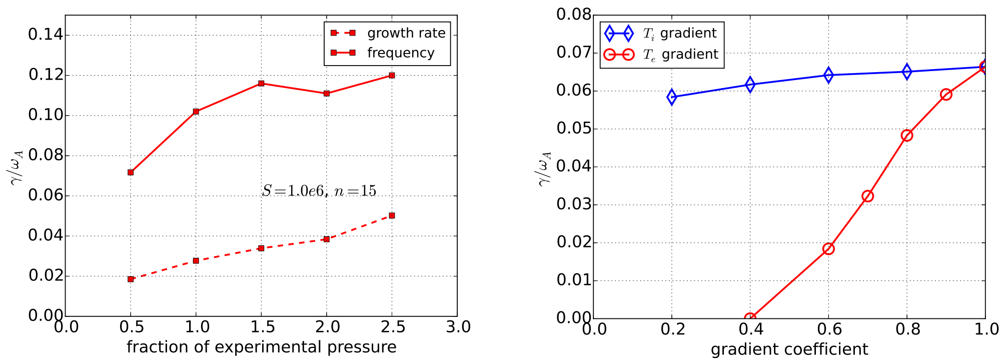

Figure 6.10: *Left figure*: The growth rate and real frequency of the drift-Alfven modes versus the pedestal height. Lindquist number: $S = 1 \times 10^6$, toroidal mode number: $n = 15$; *Right figure*: The growth rate of the drift-Alfven modes versus the ion and electron temperature gradient variations. $\beta = 2.0\%$, $n = 15$.

6.2.3.3 The linear mode structure

Having shown the characteristics of the growth rate and real frequency of the drift-Alfven modes, we will present the results of the linear mode structure in this section, which is very crucial for the nonlinear turbulence transport study in the next step. The radial mode structure is shown in figure (6.11). The bottom figure shows the electron temperature perturbation (δT_e) contour in the radial and toroidal plane at the outboard midplane, while the top figure shows the inverse of the electron pressure scale length ($1/L_{pe}$). The pedestal height is $\beta = 2.5\%$ and the toroidal mode number is $n = 15$. As we only simulate $1/n$ torus for given toroidal mode number n in the linear simulation for resolution purposes, we can only see one wave period in this region. Through the comparison, it is very clear that the radial peak position of the perturbations coincides the peak of the inverse electron pressure scale length profile in the linear stage. This is within the expectation, given the primary free energy source from the electron pressure gradient. Besides, the poloidal mode structure of the dirft-Alfven mode with $\beta = 2.5\%$ and $n = 15$ is shown in figure (6.12). In contrast to the curvature-driven ballooning mode, which localizes at the outboard midplane, the drift-Alfven modes have the poloidal peak at the top and near the X-point in this case. This unique feature of the poloidal mode structure of the pedestal micro-instability was also found in another DIII-D equilibrium with shot number 131997 using the GTC codes[23]. Although this micro-instability is later identified as collisionless trapped-electron mode (CTEM), it has various linear characteristics that are similar to drift-Alfven modes in our work, including the dispersion relation and the poloidal mode structure. Although many other numerical studies of the pedestal micro-instability [76, 77, 31] have discovered the 'unusual' poloidal mode structure, where the mode localizes somewhere else instead of the outboard midplane, the reasons remain still unclear. Two theoretical attempts have been made to explain this poloidal structure: Novakovskii et al.[50] used ballooning analysis with drift resistive effects and found that a new branch localizing at $\pm\pi/2$ ballooning angle appears in addition to the conventional ballooning mode branch. Xie et al.[85] conducted a comprehensive numerical studies on the trapped-electron mode (TEM) in the pedestal region using GTC codes and found that when the profile gradient is sharp enough, the most unstable TEM will not be the ground state, which appears at the outboard midplane, but rather be the higher states with nearly random poloidal structure or multi-peaks. In our study, the trapped electron effects are not included in the simulation model. However, the parallel electron dissipations can still serve as a simplified 'trap' mechanism.

6.2.4 The nonlinear simulations of the drift-Alfven turbulence

As the linear characteristics of the drift-Alfven modes have been shown in the previous section, now we begin to explore the features of the heat transport induced by the drift-Alfven turbulence in the pedestal region, using nonlinear simulations. One of the advantages of the BOUT++ codes in studying the heat transport in the pedestal region is the capability to extend the simulation domain outside the separatrix, i.e. to the Scrape-off layer (SOL). As the ELM-crash phenomena have been well elaborated using the three-field reduce MHD model, we now study the heat transport induced by the micro-instability using the modified five-field Landau fluid model.

6.2.4.1 The saturation of the linear perturbation

In the first example of the nonlinear simulations, the experimental equilibria with $\beta = 1.0\%$ are used. In order to retain more toroidal modes,

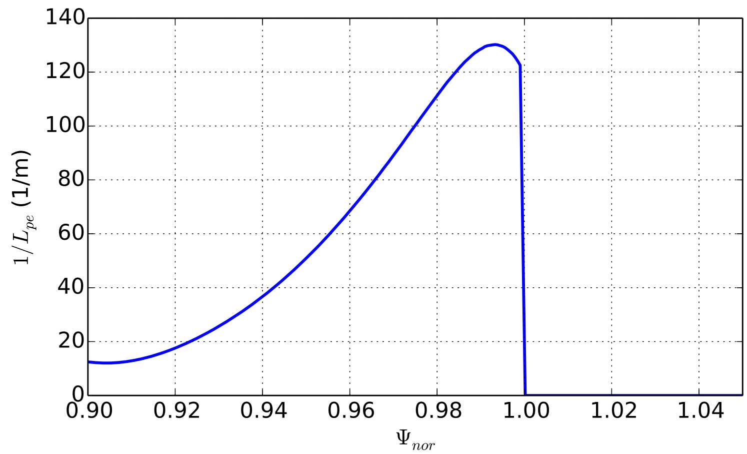

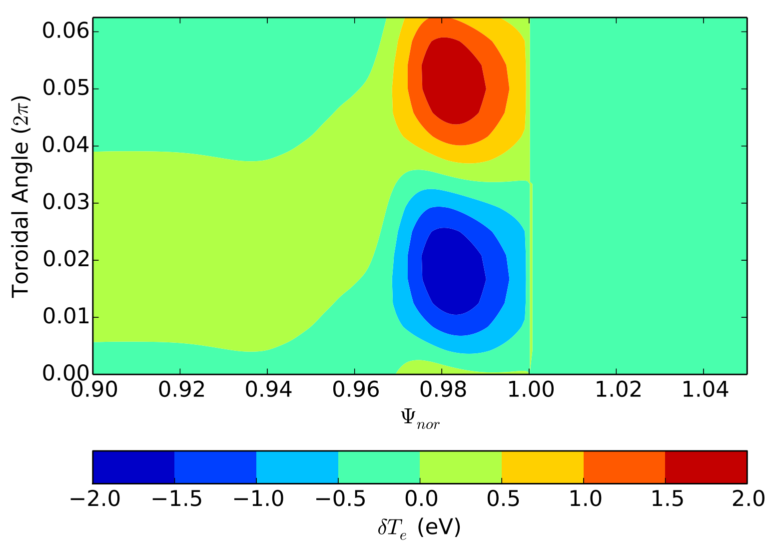

Figure 6.11: *Top figure*: The inverse of the scale length of the electron pressure profile $((dT_{e0}/dr)/T_{e0})$. $\beta = 2.5\%$; *Bottom figure*: The contour of the electron temperature perturbation in the radial and toroidal plane. The poloidal position is the outboard midplane. $\beta = 2.5\%$, $t = 110t_A$, $n = 15$, $S = 1 \times 10^8$.

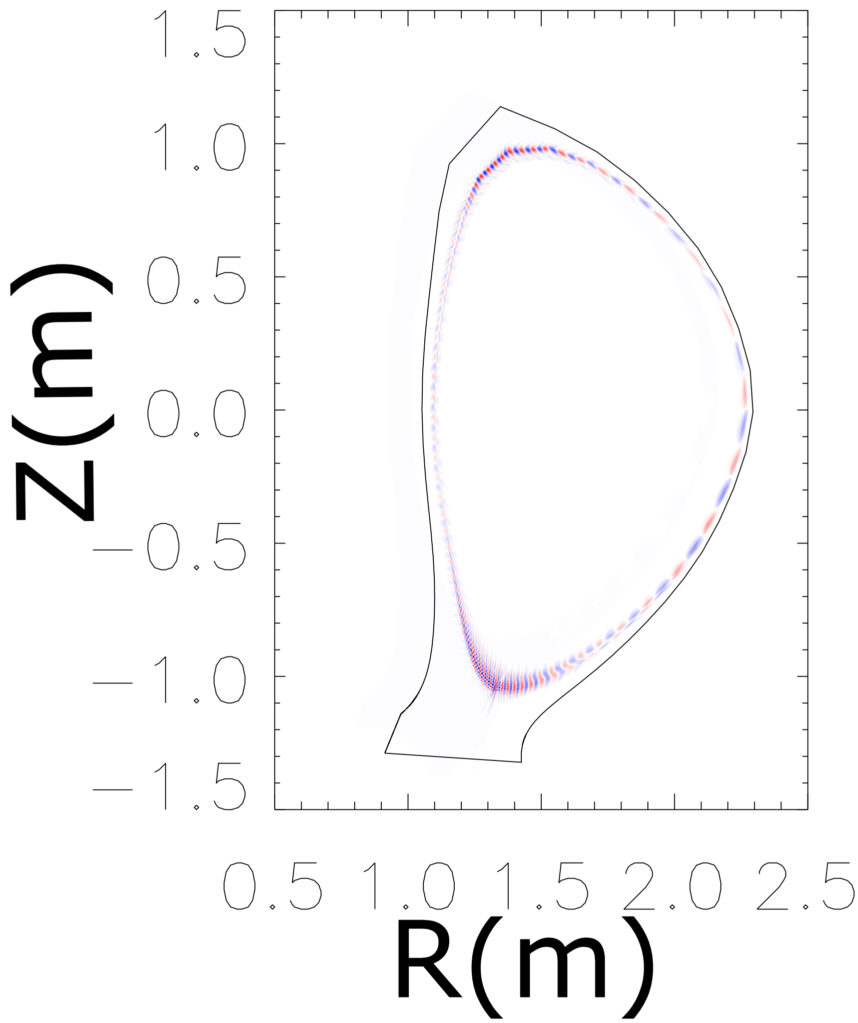

Figure 6.12: The poloidal cross-section contour of the linear drift-Alfven mode structure for $\beta = 2.0\%$, $n = 15$ and $S = 1 \times 10^8$.

the toroidal resolution is increased to $n_z = 64$, which covers 1/5 the whole torus. The initial condition is set to be the superposition of multiply toroidal modes with random amplitude.The time evolution of the amplitude of the electron temperature perturbation is shown in figure (6.13). It is clear that the linear stage where the perturbation grows exponentially and the nonlinear stage where the perturbation almost saturates is divided at the transient moment, $t \approx 100t_A$. Recall that the background electron temperature is about $T_{e0} \approx 1$KeV, then the relative saturation level is at $\delta T_e/T_{e0} \approx 12\%$.

The toroidal mode spectra of the electron temperature fluctuation at the

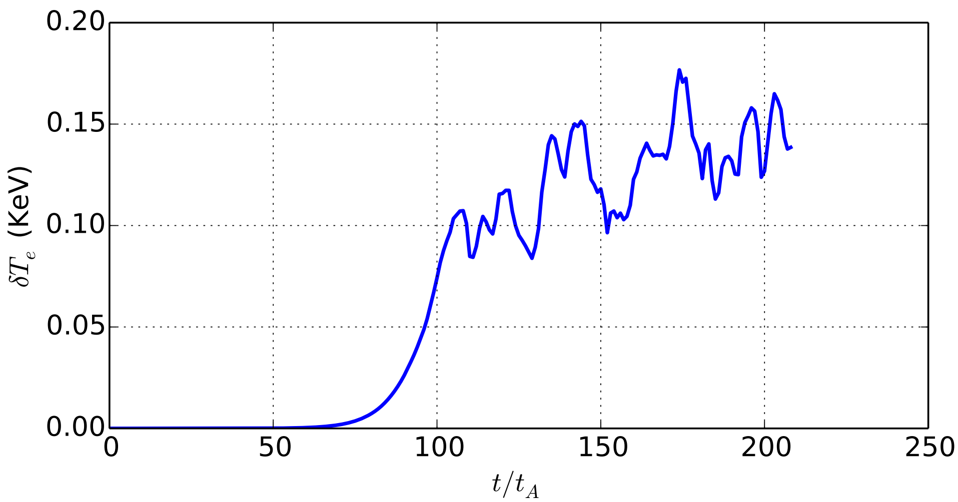

Figure 6.13: The time evolution of the root-mean-square(rms) amplitude of the electron temperature perturbation at the outboard midplane. $\beta = 1.0\%$.

outboard midplane and peak pressure gradient radial position are shown in figure (6.14) at $t = 0, 50t_A, 100t_A, 150t_A$. In the linear phase ($t < 100t_A$), the drift-Alfven with higher toroidal mode numbers grow faster and the spectra peak at high toroidal mode number ($n = 60$). Then strong nonlinear coupling saturates the high-n modes and produces inverse cascades after $t > 100t_A$. One thing that needs to be noticed is that the zonal flow components ($n = 0$) are not included in the nonlinear simulations. This inverse cascades have some analogy with the electron temperature gradient driven drift-modes([]) and the edge-localized modes (ELMs), where the dominant mode in nonlinear stage just before ELM crash is about ($n = 1$). The visualization of the drift-Alfven turbulence in the poloidal cross-section view at different time is shown in figure (6.15), where the electron temperature fluctuations (δT_e) are used to qualitatively demonstrate the turbulence characteristics. Compared to the instability in the linear phase ($t = 10t_A$, top left), the drift-Alfven turbulence in the nonlinear stage ($t = 150t_A$, top right; $t = 200t_A$, bottom) shows some distinct features. Firstly, it is clearly shown that the radial extent is much larger in the nonlinear phase due to the anomalous radial transport. Secondly, the eddy size becomes bigger due to the inverse cascade, especially at the outboard midplane. Meanwhile, the small fine structures are also developed along with the major eddies. This is consistent with existence of the high-n modes, despite that the low-n modes dominate.

6.2.4.2 The heat transport induced by the drift-Alfven turbulence

Although we can qualitatively observe the radial heat transport in figure (6.15), it is very important to quantitatively study the characteristics of the heat transport induced by the drift-Alfven turbulence. The most cru-

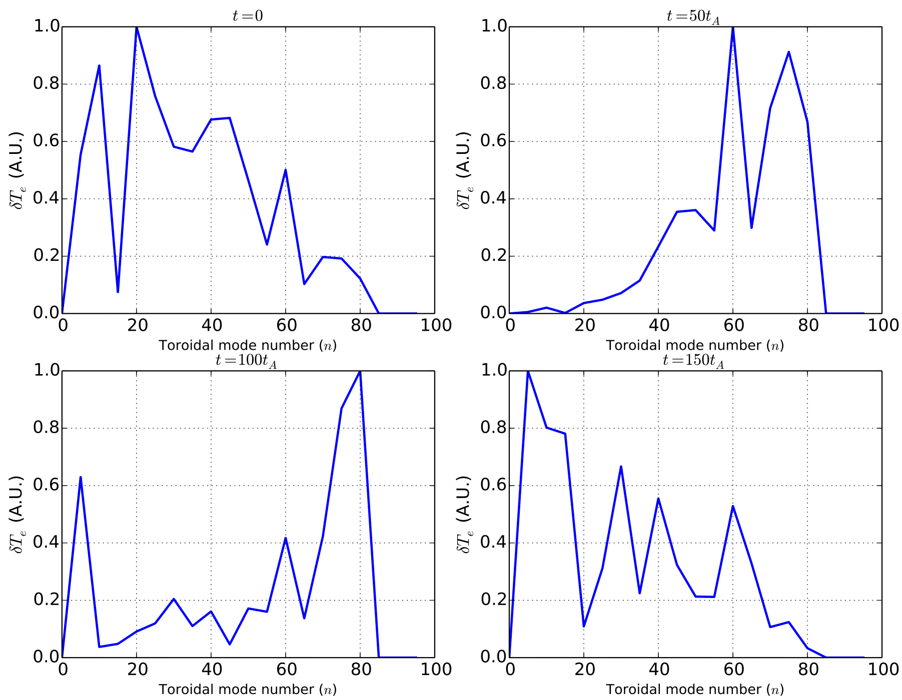

Figure 6.14: The electron temperature fluctuation spectrum at outboard midplane and peak pressure gradient radial position. The initial condition with random multiple modes is shown in the left top figure. All the amplitudes at different moment are normalized to the maximum values.

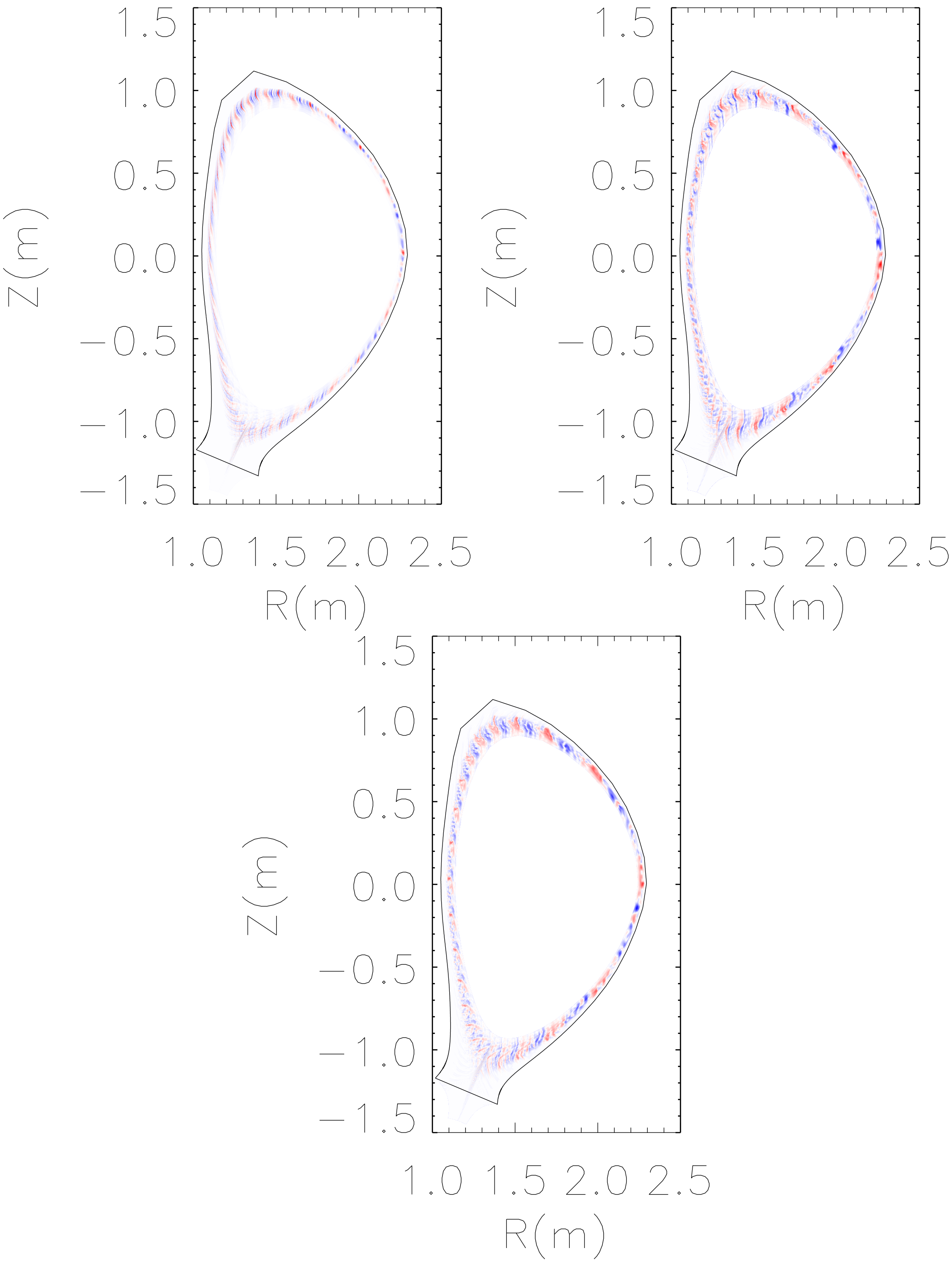

Figure 6.15: The electron temperature fluctuation of Drift-Alfven turbulence in poloidal cross-section view at $t = 10t_A$ (top left), $t = 150t_A$ (top right) and $t = 200t_A$ (bottom).

cial physics phenomena in the edge region are the L-H and H-L (type-I ELM bursts) transition, along with the periodic build and crash of the pedestal itself, which largely depends on the transport level in the edge region. Therefore, an accurate and complete understanding of the heat transport induced by turbulences is the key to explain these phenomena. A few notations need to be introduced before the simulation results are presented. The heat flux for electrons and ions is defined as:

$$\mathbf{\Gamma}_{\boldsymbol{e},\boldsymbol{i}} =< \delta T_{e,i} \boldsymbol{v}_{\boldsymbol{E}\times\boldsymbol{B}} >_\zeta \tag{6.29}$$

where the subscripts represent different spices and the pointy parentheses stand for the average over toroidal angle. Besides, $\boldsymbol{v}_{\boldsymbol{E}\times\boldsymbol{B}}$ is the $\boldsymbol{E} \times \boldsymbol{B}$ drift velocity and δT means the perturbed temperature. Therefore, the heat flux $\mathbf{\Gamma}$ is a vector function of time (t), radial position (Ψ_{nor}) and poloidal angle (θ). To avoid the confusion, we use the following notation for specific heat flux:

- $\mathbf{\Gamma}^{\boldsymbol{\Psi}}_{\boldsymbol{e},\boldsymbol{i}}$: Radial heat flux for electron (ion).
- $\mathbf{\Gamma}^{\boldsymbol{\theta}}_{\boldsymbol{e},\boldsymbol{i}}$: Poloidal heat flux for electron (ion).

Similarly, the radial transport diffusivity for electron and ion can also be calculated using:

$$\chi_{e,i} = \mathbf{\Gamma}^{\boldsymbol{\Psi}}_{\boldsymbol{e},\boldsymbol{i}} / \boldsymbol{\nabla}_\Psi T_{e0,i0} \tag{6.30}$$

Firstly, the radial transport diffusivities for electron and ion are calculated and shown in figure (6.16). The radial heat flux is averaged over the poloidal angle to take into account the cross-section shape. We can see that the radial transport diffusivity of the electrons is about 30% larger than that of the ions in the nonlinear stage. This is the expected results, for the drift-Alfven instability is driven by the electron pressure gradient. However, compared to the trapped electron mode, where the difference between electron and ion radial heat flux could be two to three times[8], the ion still plays an important role in the drift-Alfven turbulence. Despite the fact that the poloidal averaged radial heat flux gives a general picture of transport characteristics, we should also study the radial heat flux at different poloidal angle, for the unconventional linear mode structure localizes at the top and near the X-point. The results are shown in figure (6.17) and the average values represented by the dashed lines are listed below: There are two noticeable conclusions that can be made

$\mathbf{\Gamma^{\Psi}}$(KeV*m/s)	top	X-point	outboard midplane
electron	4.6	12.8	26.0
ion	2.6	7.5	29.8

Table 6.1: The average values of the electron and ion radial heat flux at different poloidal positions.

from figure (6.17) and table 6.1. The first one is that although the difference of the poloidal averaged radial heat flux between electron and ion is only 30% as stated previously, this difference increases to almost 200% at the top and X-point, where the linear drift-Alfven modes peak. The second one is that the maximum radial heat flux for both ion and electron comes from the outboard midplane, not the top and X-point where the linear modes peak. In order to understand these results, we need to consider not only the anomalous radial transport, but also the poloidal transport. In the top figure of figure (6.18), we

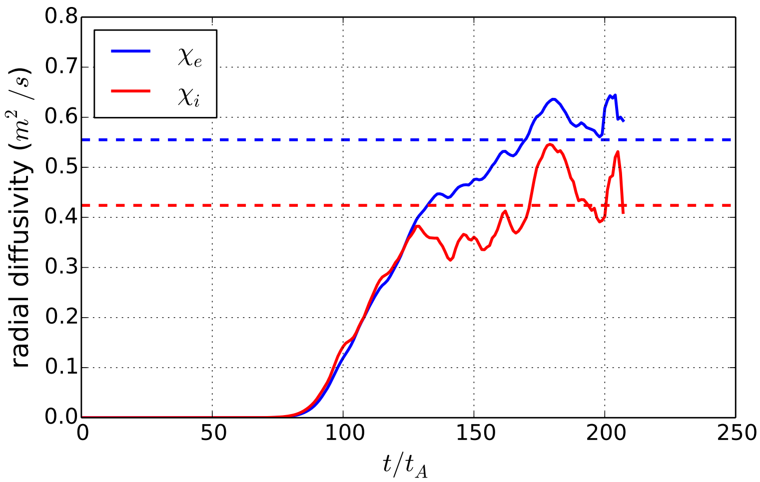

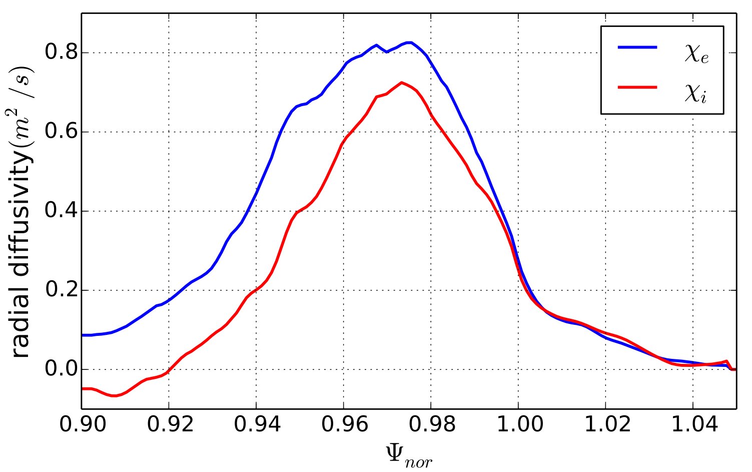

Figure 6.16: *top figure*: The time evolution of the radial diffusivity of electron (blue) and ion (red) at peak pressure gradient radial position ($\Psi_{nor} = 0.962$). The dashed lines represent the average value in the nonlinear stage ($140t_A < t < 200 < t_A$): $\chi_e^{ave} \approx 0.555m^2/s$, $\chi_i^{ave} \approx 0.424m^2/s$; *bottom figure*: The radial profile of the radial diffusivity of electron and ion at $t = 200t_A$.

can see that there are two peaks of the radial heat flux around the outboard midplane. Meanwhile, the poloidal heat flux at the top and X-point have the opposite sign. In other words, the electron poloidal heat flux from both top and X-point both head to the outboard midplane. Moreover, the bottom figure shows that the poloidal heat flux at the outboard midplane is much smaller. Therefore, a possible explanation for figure (6.17) is as followed: In addition to the anomalous radial heat transport at the top and X-point, where drift-Alfven modes peak in the linear stage, strong poloidal heat transport appears, which transfer a large amount of energy to the outboard midplane. These energy is then transferred through radial transport at the outboard midplane. This results may inspire more further numerical and theoretical studies on the heat transport features of the drift turbulences, which have unconventional poloidal mode structures in the linear phase, like the trapped electron modes ([85]). As more and more results have shown the drift-instabilities with unconventional poloidal mode structure, our study could be a start of a comprehensive research on the energy transport induced by the pedestal turbulences.

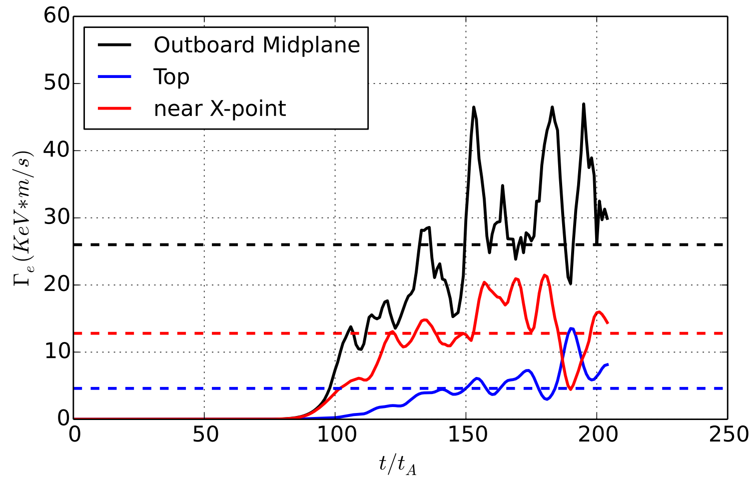

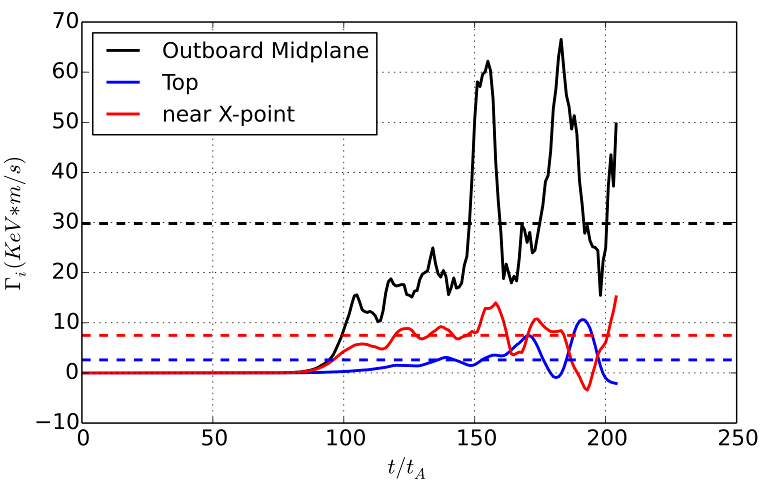

Figure 6.17: *Left figure*: The time evolution of the electron radial heat flux at top (blue), outboard midplane (black) and X-point (red). The dashed lines represent the average values in nonlinear stage ($140t_A < t < 200t_A$); *Right figure*: The same as left figure, ion radial heat flux.

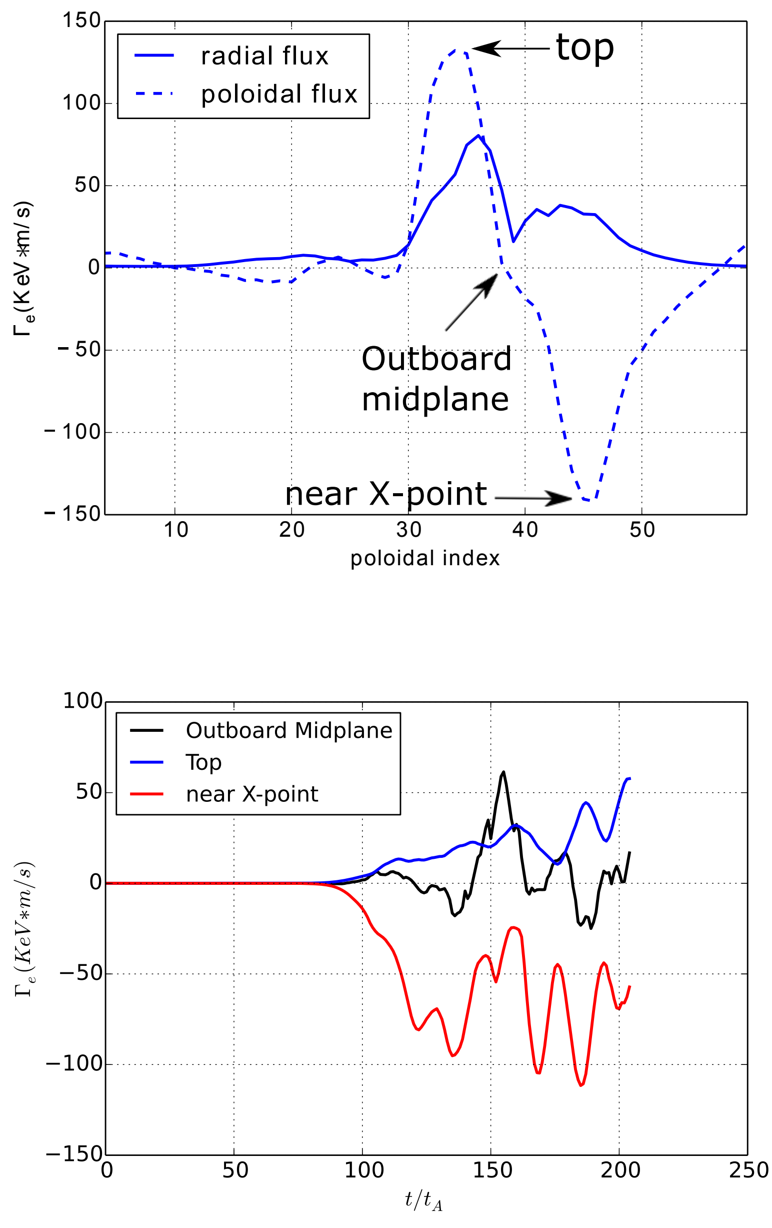

Figure 6.18: *Top figure*: The electron radial (solid) and poloidal (dashed) heat flux versus the poloidal index at $t = 200t_A$. The indices that represent the top, outboard midplane and X-point position are marked; *Bottom figure*: The time evolution of the electron poloidal heat flux at the top, outboard midplane and X-point position.

Chapter 7

Summary

In this thesis, we explore the characteristics of the linear behaviors and transport features of the macro- and micro-instability in the pedestal region of the Tokamak, using theoretical and numerical tools. As the typical examples, the peeling-ballooning mode and the drift-Alfven mode are studied in both limiter and divertor tokamak geometry. In particular, the edge-localized modes (ELMs), which appears to be repetitive energy burst in the edge region, are studied and the results are compared with the experiment data. Moreover, BOUT++ codes are used for the linear and nonlinear global simulations. The transport features of the high-Z/intermediate-Z impurities are studied in both tokamak and stellarator geometry using theoretical fluid analysis.

After an introduction and review of the previous studies on the related topics, the primary numerical tool, the BOUT++ codes are verified using the well-defined two-dimensional diffusion equation in both planar and cylindrical geometry in chapter 2. In the first part of chapter 3, the BOUT++ codes are verified with a complicated model, the double-adiabatic MHD model, which is used to study the firehose and mirror instability. Excellent agreements are obtained between the analytical and simulation results. Besides, the firehose instability is also studied using the kinetic theory with anisotropic Maxwellian distribution equilibria in the second part of chapter 3.

In chapter 4, the impurity transport induced by the density gradient driven drift-wave turbulence is studied theoretically and the transport diffusivity is estimated for slab, tokamak and stellarator geometry. Based on the famous Hasegawa-Wakatani drift-wave model, one more equation is added for the dynamics of the impurity density. The linear results are qualitatively consistent with the gyrokinetic results.

The fundamental characteristics of the peeling-ballooning modes and the ELM burst are described using simulations results in chapter 5. Two important topics are studied using BOUT++ codes. One is the scaling law between the relative energy loss of ELMs and the edge collisionality, which is first discovered by observing the multi-tokamak data. We use the shifted-circular, i.e. limiter tokamak geometry, to reproduce the scaling property, which is the first step of the comprehensive research to disclose the nature of this scaling law. Another is the study of the difference linear behaviors of the P-B modes in standard and snowflake divertor geometry. We found that the change of the local magnetic shear at the outboard midplane due to the modification of the poloidal coils when switching from standard to snowflake geometry is the key to explain the difference. We found that the stability of the P-B modes in the pedestal is very sensitive to the local magnetic topology at the outboard midplane.

In chapter 6, we present the theoretical and numerical study results of one of the micro-instability in the pedestal region, the drift-Alfven instability. The simulation of the drift-Alfven instability is conducted using a sequence of equilibria with different pedestal height. These equilibria is generated by the 'VARYPED' tool based on the DIII-D H-mode discharge. The linear dispersion relation obtained from simulation results are qualitatively consistent with the theoretical results. The transport induced by the drift-Alfven turbulence is also studied using the global nonlinear model and the transport diffusivity is estimated for both ions and elections.

Appendices

Appendix A

Bessel Function

Bessel functions are the canonical solution $y(x)$ of the differential function:

$$x^2\frac{d^2y}{dx^2} + x\frac{dy}{dx} + (x^2 - \alpha^2)y = 0 \tag{A.1}$$

Depending on the boundary conditions, the solution will be a combination of Bessel function of the first kind $(J_\alpha(x))$[1] and Bessel function of the second kind $(Y_\alpha(x))$. As the Bessel functions of the second kind have a singularity at origin $(x = 0)$, We will only focus on the Bessel functions of the first kind.

Bessel function of the first kind $(J_\alpha(x))$ is the solution with finite value at $x = 0$ and can be defined by Gamma function:

$$J_\alpha(x) = \sum_{m=0}^{\infty} \frac{(-1)^m}{m!\Gamma(m+\alpha+1)}\left(\frac{x}{2}\right)^{2m+\alpha} \tag{A.2}$$

Bessel function of the first kind has the following property:

$$\int_0^a \rho J_\alpha(k\rho)J_\alpha(k'\rho)d\rho = \frac{a[k'J_\alpha(ka)J'_\alpha(k'a) - kJ_\alpha(k'a)J'_\alpha(ka)]}{k^2 - k'^2} \tag{A.3}$$

This property indicates the orthogonality of the Bessel function of the first kind. In fact, there are two sets of orthogonal functions based on $J_\alpha(x)$ in region $[0, \rho_0]$:

[1]Although α could be any positive numbers, we assume it to be only integers in the following context.

- $J_\alpha(A_{\alpha,k}\frac{\rho}{\rho_0})$, $k = 1, 2, 3, ...$, where $A_{\alpha,k}$ is the k_{th} zero of function $J_\alpha(\rho)$. The normalization of this set of functions is:

$$I^A_{\alpha,k} = \int_0^{\rho_0} [\rho J_\alpha(A_{\alpha,k}\frac{\rho}{\rho_0})]^2 d\rho = \frac{\rho_0^2}{2}[J_{\alpha+1}(A_{\alpha,k})]^2 \tag{A.4}$$

Therefore, the coefficients can be calculated:

$$C_{\alpha,k} = \frac{1}{I^A_{\alpha,k}} \int_0^{\rho_0} f(\rho) J_\alpha(A_{\alpha,k}\frac{\rho}{\rho_0})\rho d\rho \tag{A.5}$$

where $f(\rho)$ is an arbitrary function in region $[0, \rho_0]$,

$$f(\rho) = \sum_{k=1}^{\infty} C_{\alpha,k} J_\alpha(A_{\alpha,k}\frac{\rho}{\rho_0}) \tag{A.6}$$

- $J_\alpha(B_{\alpha,k}\frac{\rho}{\rho_0})$, $k = 1, 2, 3, ...$, where $B_{\alpha,k}$ is the k_{th} zero of the function $J'_\alpha(\rho)$. The normalization of this set of function is:

$$I^B_{\alpha,k} = \int_0^{\rho_0} [\rho J_\alpha(B_{\alpha,k}\frac{\rho}{\rho_0})]^2 d\rho = -\frac{\rho_0^2}{2} J_\alpha(B_{\alpha,k}) J''_\alpha(B_{\alpha,k}) \tag{A.7}$$

Therefore, the coefficients can be calculated:

$$C_{\alpha,k} = \frac{1}{I^B_{\alpha,k}} \int_0^{\rho_0} f(\rho) J_\alpha(B_{\alpha,k}\frac{\rho}{\rho_0})\rho d\rho \tag{A.8}$$

where $f(\rho)$ is an arbitrary function in region $[0, \rho_0]$,

$$f(\rho) = \sum_{k=1}^{\infty} C_{\alpha,k} J_\alpha(B_{\alpha,k}\frac{\rho}{\rho_0}) \tag{A.9}$$

Appendix B

Double-Adiabatic MHD

B.1 pressure equation derivation

Fluid equations can be derived Recall Vlasov equation, by assuming maxwellian-like distribution and averaging over velocity space. Recall vlasov equation:

$$\frac{\partial f}{\partial t} + \boldsymbol{v} \cdot \nabla f + q\frac{\boldsymbol{E} + \boldsymbol{v} \times \boldsymbol{B}}{m} \cdot \nabla_{\boldsymbol{v}} f = 0 \tag{B.1}$$

, or in tensor form

$$\frac{\partial f}{\partial t} + v_i \frac{\partial f}{\partial x_i} + q\frac{E_i + \varepsilon_{ijk} v_j B_k}{m} \frac{\partial f}{\partial v_i} = 0 \tag{B.2}$$

As macroscopic pressure is described as:

$$p_{mn} = m \int w_i w_j f d^3 v, w_i = v_i - u_i \tag{B.3}$$

where $\boldsymbol{u}(\boldsymbol{x}, t)$ is macroscopic fluid velocity. Pressure equation in components can be derived by multiplying equation (B.2) by $w_i w_j$ and integrate over velocity space.

$$\frac{dp_{mn}}{dt} + \frac{\partial}{\partial x_j} S_{mnj} + p_{mn}\frac{\partial u_i}{\partial x_i} + p_{nj}\frac{\partial u_m}{\partial x_j} + p_{mj}\frac{\partial u_n}{\partial x_j} - q\varepsilon_{mkl} p_{nk} B_l - q\varepsilon_{nkl} p_{mk} B_l = 0 \tag{B.4}$$

where $S_{mnj} = m \int w_m w_n w_j d^3v$. For isotropic pressure tensor, $p_{mn} = p\delta_{mn}$,

$$\frac{dp}{dt} + \nabla \cdot \boldsymbol{S} + \frac{5}{3}p(\nabla \cdot \boldsymbol{u}) = 0 \tag{B.5}$$

$\boldsymbol{S}$ in this equation describes energy flux, and can be eliminated by adiabatic assumption. Similarly, for anisotropic pressure tensor $p_{mn} = p_\parallel b_m b_n + p_\perp(\delta_{mn} - b_m b_n)$, if let $m = n = 3$, then $p_{mn} = p_\parallel$,this equation becomes:

$$\frac{dp_\parallel}{dt} + \nabla \cdot \boldsymbol{S}_\parallel + p_\parallel \nabla \cdot \boldsymbol{u} + 2p_\parallel \boldsymbol{b} \cdot (\boldsymbol{b} \cdot \nabla)\boldsymbol{u} = 0 \tag{B.6}$$

if let $m = n = 1$, then $p_{mn} = p_\perp$:

$$\frac{dp_\perp}{dt} + \nabla \cdot \boldsymbol{S}_\perp + 2p_\perp \nabla \cdot \boldsymbol{u} - p_\perp \boldsymbol{b} \cdot (\boldsymbol{b} \cdot \nabla)\boldsymbol{u} = 0 \tag{B.7}$$

in which $\boldsymbol{S}_\parallel$ and $\boldsymbol{S}_\perp$ are energy flux in parallel and perpendicular direction. Assumption of double adiabatic condition eliminates both terms, and gives equation (3.10) and (3.11).

B.2 Dispersion relation

After we obtain linearized equations (3.18) to (3.22), several intermediate steps are required before getting to dispersion relation (3.24).First, conduct dot product with $\boldsymbol{b}_0$ on both sides of equation (3.22):

$$\boldsymbol{b}_0 \cdot \frac{\partial^2 \boldsymbol{\xi}}{\partial t^2} = p_{\perp 0}(\boldsymbol{b}_0 \cdot \nabla)(\nabla \cdot \boldsymbol{\xi}) + (3p_{\parallel 0} - p_{\perp 0})\boldsymbol{b}_0 \cdot ((\boldsymbol{b}_0 \cdot \nabla)^2 \boldsymbol{\xi}) \tag{B.8}$$

Taking the divergence of both sides of equation (3.22), differentiating twice with respect to time, expressing $(\boldsymbol{b}_0 \cdot \frac{\partial^2 \boldsymbol{\xi}}{\partial t^2}$ by means of equation (B.8)), and apply relation $\nabla \cdot \boldsymbol{\xi} = -\rho_1/\rho_0$, we obtain

$$\begin{aligned}
&\frac{\partial^4 \rho_1}{\partial t^4} - \left(2\frac{p_{\perp 0}}{\rho_0} + v_A^2\right)\nabla^2 \frac{\partial^2 \rho_1}{\partial t^2} - \left(2\frac{p_{\parallel 0}}{\rho_0} - \frac{p_{\perp 0}}{\rho_0}\right)(\boldsymbol{b}_0 \cdot \nabla)^2 \frac{\partial^2 \rho_1}{\partial t^2} \\
&- \left[\frac{p_{\perp 0}^2}{\rho_0^2} - 3\frac{p_{\parallel 0}}{\rho_0}\left(2\frac{p_{\perp 0}}{\rho_0} + v_A^2\right)\right]\nabla^2 (\boldsymbol{b}_0 \cdot \nabla)^2 \rho_1 \\
&+ \left[3\frac{p_{\parallel 0}^2}{\rho_0^2} + \frac{p_{\perp 0}}{\rho_0}\left(3\frac{p_{\parallel 0}}{\rho_0} - \frac{p_{\perp 0}}{\rho_0}\right)\right](\boldsymbol{b}_0 \cdot \nabla)^4 \rho_1 = 0.
\end{aligned}$$

Finally, we obtain this linear partial differential equations of density fluctuation ρ_1. Assuming that $\rho_1(\boldsymbol{x}, t) \propto \exp(i\boldsymbol{k} \cdot \boldsymbol{r} - i\omega t)$, and taking advantage of relations (3.23), we can get dispersion relation (3.24).

B.3 Quadratic equation

In quadratic equation (3.25), let:

$$\frac{p_{\perp 0}}{\rho_0} = a,\ \frac{p_{\parallel 0}}{\rho_0} = b,\ v_A^2 = c \tag{B.9}$$

then,

$$\begin{aligned}
\Delta \quad &= (a + 2b + c)^2 k_\parallel^4 + 12b(b - c - a)k_\parallel^4 \\
&= (a^2 + 16b^2 + c^2 - 8bc - 8ab + 2ac)k_\parallel^4 \\
&= (a - 4b + c)^2 k_\parallel^4 \geq 0
\end{aligned}$$

Bibliography

[1] S.L. Allen, T.H. Osborne, E. Kolemen, J. Boedo, N. Brooks, M. Fenstermacher, R. Groebner, D.N. Hill, A. Hyatt, C. Lasnier, et al. Initial snowflake divertor physics studies on diii-d. *Proc. 24th IAEA FEC-IAEA CN-197, San Diego*, pages 8–13, 2012.

[2] P Andersson and J Weiland. A fully toroidal fluid analysis of the magnetohydrodynamic ballooning mode branch in tokamaks. *Physics of Fluids (1958-1988)*, 31(2):359–365, 1988.

[3] C. Angioni, F.J. Casson, C. Veth, and A.G. Peeters. Analytic formulae for centrifugal effects on turbulent transport of trace impurities in tokamak plasmas. *Physics of Plasmas (1994-present)*, 19(12):122311, 2012.

[4] HAB Bodin and AA Newton. Reversed-field-pinch research. *Nuclear fusion*, 20(10):1255, 1980.

[5] BJ Burke, SE Kruger, CC Hegna, P Zhu, PB Snyder, CR Sovinec, and EC Howell. Edge localized linear ideal magnetohydrodynamic instability studies in an extended-magnetohydrodynamic code. *Physics of Plasmas (1994-present)*, 17(3):032103, 2010.

[6] S.A. Cohen, J.L. Cecchi, and E.S. Marmar. Impurity transport in a quiescent tokamak plasma. *Physical Review Letters*, 35(22):1507, 1975.

[7] J.W. Connor, R.J. Hastie, H.R. Wilson, and R.L. Miller. Magnetohydrodynamic stability of tokamak edge plasmas. *Physics of Plasmas*, 5(7):2687–2700, 1998.

[8] Tilman Dannert and Frank Jenko. Gyrokinetic simulation of collisionless trapped-electron mode turbulence. *Physics of Plasmas (1994-present)*, 12(7):072309, 2005.

[9] RN Dexter, DW Kerst, TW Lovell, SC Prager, and JC Sprott. The madison symmetric torus. *Fusion Science and Technology*, 19(1):131–139, 1991.

[10] A Diallo, JW Hughes, M Greenwald, B LaBombard, E Davis, SG Baek, C Theiler, P Snyder, J Canik, J Walk, et al. Observation of edge instability limiting the pedestal growth in tokamak plasmas. *Physical review letters*, 112(11):115001, 2014.

[11] AM Dimits, I Joseph, and MV Umansky. A fast non-fourier method for landau-fluid operator. *Physics of Plasmas (1994-present)*, 21(5):055907, 2014.

[12] JQ Dong, L Chen, F Zonca, and GD Jian. Study of kinetic shear alfven instability in tokamak plasmas. *Physics of Plasmas (1994-present)*, 11(3):997–1005, 2004.

[13] W. Dröge, P. Meyer, P. Evenson, and D. Moses. Electron acceleration in solar flares. *Solar Physics*, 121(1):95–103, 1989.

[14] N. Dubuit, X. Garbet, T. Parisot, R. Guirlet, and C. Bourdelle. Fluid simulations of turbulent impurity transport. *Physics of Plasmas (1994-present)*, 14(4):042301, 2007.

[15] B.D. Dudson, M.V. Umansky, X.Q. Xu, P.B. Snyder, and H.R. Wilson. Bout++: A framework for parallel plasma fluid simulations. *Computer Physics Communications*, 180(9):1467–1480, 2009.

[16] T.E. Evans, R.A. Moyer, K.H. Burrell, M.E. Fenstermacher, I. Joseph, A.W. Leonard, T.H. Osborne, G.D. Porter, M.J. Schaffer, P.B. Snyder, et al. Edge stability and transport control with resonant magnetic perturbations in collisionless tokamak plasmas. *nature physics*, 2(6):419–423, 2006.

[17] G. Federici, P. Andrew, P. Barabaschi, J. Brooks, R. Doerner, A. Geier, A. Herrmann, G. Janeschitz, K. Krieger, A. Kukushkin, et al. Key iter plasma edge and plasma–material interaction issues. *Journal of nuclear materials*, 313:11–22, 2003.

[18] M.E. Fenstermacher, X.Q. Xu, I. Joseph, M.J. Lanctot, C.J. Lasnier, W.H. Meyer, B. Tobias, L. Zeng, A.W. Leonard, and T.H. Osborne. Fast pedestal, sol and divertor measurements from diii-d to validate bout++ nonlinear elm simulations. *Journal of Nuclear Materials*, 438:S346–S350, 2013.

[19] ME Fenstermacher, XQ Xu, I Joseph, MJ Lanctot, CJ Lasnier, WH Meyer, B Tobias, L Zeng, AW Leonard, and TH Osborne. Fast pedestal, sol and

divertor measurements from diii-d to validate bout++ nonlinear elm simulations. *Journal of Nuclear Materials*, 438:S346–S350, 2013.

[20] S. Ferrando-Margalet, H. Sugama, and T.H. Watanabe. Zonal flows and ion temperature gradient instabilities in multiple-helicity magnetic fields. *Physics of Plasmas (1994-present)*, 14(12):122505, 2007.

[21] X.R. FU, W. HORTON, I.O. BESPAMYATNOV, W.L. ROWAN, S. BENKADDA, C.L. FIORE, S. FUTATANI, and K.T. LIAO. Turbulent impurity transport modeling for alcator c-mod. *Journal of Plasma Physics*, 79:837–846, 10 2013.

[22] X.Y. Fu, J.Q. Dong, W. Horton, C.T. Ying, and G.J. Liu. Turbulent particle transport in tokamak plasmas with impurities. *Physics of Plasmas (1994-present)*, 4(3):588–597, 1997.

[23] D.P. Fulton, Z. Lin, I. Holod, and Y. Xiao. Microturbulence in diii-d tokamak pedestal. i. electrostatic instabilities. *Physics of Plasmas (1994-present)*, 21(4):042110, 2014.

[24] S. Futatani, D. del Castillo-Negrete, X. Garbet, S. Benkadda, and N. Dubuit. Self-consistent dynamics of impurities in magnetically confined plasmas: Turbulence intermittency and nondiffusive transport. *Physical review letters*, 109(18):185005, 2012.

[25] S. Futatani, X. Garbet, S. Benkadda, and N. Dubuit. Impurity dynamics in the presence of transport barriers in tokamaks. *Physics of Plasmas*

(1994-present), 17(10):102501, 2010.

[26] S. Futatani, W. Horton, S. Benkadda, I.O. Bespamyatnov, and W.L. Rowan. Fluid models of impurity transport via drift wave turbulence. *Physics of Plasmas (1994-present)*, 17(7):072512, 2010.

[27] RJ Groebner and TN Carlstrom. Critical edge parameters for h-mode transition in diii-d. *Plasma physics and controlled fusion*, 40(5):673, 1998.

[28] RJ Groebner, CS Chang, JW Hughes, R Maingi, PB Snyder, XQ Xu, JA Boedo, DP Boyle, JD Callen, JM Canik, et al. Improved understanding of physics processes in pedestal structure, leading to improved predictive capability for iter. *Nuclear Fusion*, 53(9):093024, 2013.

[29] O Gruber, A Kallenbach, M Kaufmann, K Lackner, V Mertens, J Neuhauser, F Ryter, H Zohm, M Bessenrodt-Weberpals, K Büchl, et al. Observation of continuous divertor detachment in h-mode discharges in asdex upgrade. *Physical review letters*, 74(21):4217, 1995.

[30] Gregory W. Hammett and Francis W. Perkins. Fluid moment models for landau damping with application to the ion-temperature-gradient instability. *Phys. Rev. Lett.*, 64:3019–3022, Jun 1990.

[31] D.R. Hatch, F. Jenko, M.J. Pueschel, D. Told, H. Doerk, M.G. Dunne, E. Wolfrum, E. Viezzer, and The ASDEX Upgrade Team. Gyrokinetic study of asdex upgrade inter-elm pedestal profile evolution. (submitted to Phys. Plasmas), 2015.

[32] Bong-Guen Hong, W Horton, and Duk-In Choi. Drift-alfvén kinetic stability theory in the ballooning mode approximation. *Physics of Fluids B Plasma Physics*, 1(8):1589, 1989.

[33] W. Horton. *Turbulent Transport in Magnetized Plasmas*. World Scientific, 2012.

[34] W. Horton and W. Rowan. Impurity transport studies in the texas experimental tokamak (text). *Physics of Plasmas (1994-present)*, 1(4):901–908, 1994.

[35] W Horton, JE Sedlak, Duk-In Choi, and BG Hong. Kinetic theory of the electromagnetic drift modes driven by pressure gradients. *Physics of Fluids (1958-1988)*, 28(10):3050–3060, 1985.

[36] A. Iiyoshi, M. Fujiwara, O. Motojima, N. Ohyabu, and K. Yamazaki. Design study for the large helical device. *Fusion Science and Technology*, 17(1):169–187, 1990.

[37] S. Ji and R.A. Wolf. Double-adiabatic mhd theory for motion of a thin magnetic filament and possible implications for bursty bulk flows. *Journal of geophysical research*, 108(A5):1191, 2003.

[38] Y. Koide, M. Kikuchi, M. Mori, S. Tsuji, S. Ishida, N. Asakura, Y. Kamada, T. Nishitani, Y. Kawano, T. Hatae, et al. Internal transport barrier on q= 3 surface and poloidal plasma spin up in jt-60u high-β p discharges. *Physical review letters*, 72(23):3662, 1994.

[39] M. Kotschenreuther, W. Dorland, M.A. Beer, and G.W. Hammett. Quantitative predictions of tokamak energy confinement from first-principles simulations with kinetic effects. *Physics of Plasmas (1994-present)*, 2(6):2381–2389, 1995.

[40] M. Kotschenreuther, P.M. Valanju, S.M. Mahajan, and J.C. Wiley. On heat loading, novel divertors, and fusion reactors. *Physics of Plasmas (1994-present)*, 14(7):072502, 2007.

[41] L.L. Lao, H.S. John, R.D. Stambaugh, A.G. Kellman, and W. Pfeiffer. Reconstruction of current profile parameters and plasma shapes in tokamaks. *Nuclear fusion*, 25(11):1611, 1985.

[42] Acad.M.A. Leontovich. *Reviews of Plasma Physics*, volume 4. Consultants Bureau, New York, 1966.

[43] S.F. Liu, S.C. Guo, C.L. Zhang, J.Q. Dong, L. Carraro, and Z.R. Wang. Impurity effects on the ion temperature gradient mode in reversed-field pinch plasmas. *Nuclear Fusion*, 51(8):083021, 2011.

[44] S.F. Liu, C.L. Zhang, W. Kong, S.C. Guo, J.Q. Dong, L.M. Liu, Q. Liu, and Z.Y. Liu. Gyrokinetic study of impurity mode in reversed-field pinch. *EPL (Europhysics Letters)*, 97(5):55004, 2012.

[45] A Loarte, G Saibene, R Sartori, D Campbell, M Becoulet, L Horton, T Eich, A Herrmann, G Matthews, N Asakura, et al. Characteristics

of type i elm energy and particle losses in existing devices and their extrapolation to iter. *Plasma Physics and Controlled Fusion*, 45(9):1549, 2003.

[46] CH Ma, XQ Xu, PW Xi, and TY Xia. Impact of relative phase shift on inward turbulent spreading. *Physics of Plasmas (1994-present)*, 22(1):010702, 2015.

[47] JF Ma, XQ Xu, and BD Dudson. Linear peeling–ballooning mode simulations in snowflake-like divertor configuration using bout++ code. *Nuclear Fusion*, 54(3):033011, 2014.

[48] S.Y. Medvedev, A.A. Ivanov, A.A. Martynov, Y. Poshekhonov, R. Behn, Y.R. Martin, J-M Moret, F. Piras, A. Pitzschke, A. Pochelon, et al. Edge stability and pedestal profile sensitivity of snowflake diverted equilibria in the tcv tokamak. *Contributions to Plasma Physics*, 50(3-5):324–330, 2010.

[49] Praveen Narayanan, Alice Koniges, Leonid Oliker, Robert Preissl, Samuel Williams, Nicholas J Wright, Maxim Umansky, Xueqiao Xu, Benjamin Dudson, Stephane Ethier, et al. Performance characterization for fusion co-design applications. *Proceedings of CUG*, 2011.

[50] S.V. Novakovskii, P.N. Guzdar, J.F. Drake, C.S. Liu, and F.L. Waelbroeck. New unstable branch of drift resistive ballooning modes in tokamaks. *Physics of Plasmas (1994-present)*, 2(3):781–791, 1995.

[51] E Ott and RN Sudan. Nonlinear theory of ion acoustic waves with landau damping. *Physics of Fluids (1958-1988)*, 12(11):2388–2394, 1969.

[52] G. Paesold and A.O. Benz. Electron firehose instability and acceleration of electrons in solar flares. *arXiv preprint astro-ph/0001262*, 2000.

[53] F. Piras, S. Coda, B.P. Duval, B. Labit, J. Marki, S. Y. Medvedev, J-M Moret, A. Pitzschke, O. Sauter, TCV Team, et al. ?snowflake? h mode in a tokamak plasma. *Physical review letters*, 105(15):155003, 2010.

[54] K.V. Roberts and J.B. Taylor. Magnetohydrodynamic equations for finite larmor radius. *Phys. Rev. Letters*, 8, 1962.

[55] W.L. Rowan, I.O. Bespamyatnov, and C.L. Fiore. Light impurity transport at an internal transport barrier in alcator c-mod. *Nuclear Fusion*, 48(10):105005, 2008.

[56] V. Rozhansky. Modelling of the edge plasma with account of self-consistent electric fields. *Contributions to Plasma Physics*, 46(7-9):575–585, 2006.

[57] D.D. Ryutov. Geometrical properties of a ?snowflake? divertor. *Physics of Plasmas (1994-present)*, 14(6):064502, 2007.

[58] D.D. Ryutov, R.H. Cohen, E. Kolemen, L. LoDestro, M. Makowski, J. Menard, T.D. Rognlien, V.A. Soukhanovskii, M.V. Umansky, and X.Q. Xu. Theory and simulations of elm control with a snowflake divertor. In *Proc. 24th Int. Conf. on Fusion Energy, pp. P*, pages 4–18, 2012.

[59] D.D. Ryutov, R.H. Cohen, T.D. Rognlien, and M.V. Umansky. The magnetic field structure of a snowflake divertor. *Physics of Plasmas (1994-present)*, 15(9):092501, 2008.

[60] Olivier Sauter, Clemente Angioni, and YR Lin-Liu. Neoclassical conductivity and bootstrap current formulas for general axisymmetric equilibria and arbitrary collisionality regime. *Physics of Plasmas (1994-present)*, 6(7):2834–2839, 1999.

[61] Bruce D Scott. Drift wave versus interchange turbulence in tokamak geometry: Linear versus nonlinear mode structure. *Physics of Plasmas (1994-present)*, 12(6):062314, 2005.

[62] P.B. Snyder, R.J. Groebner, J.W. Hughes, T.H. Osborne, M. Beurskens, A.W. Leonard, H.R. Wilson, and X.Q. Xu. A first-principles predictive model of the pedestal height and width: development, testing and iter optimization with the eped model. *Nuclear Fusion*, 51(10):103016, 2011.

[63] P.B. Snyder, R.J. Groebner, J.W. Hughes, T.H. Osborne, M. Beurskens, A.W. Leonard, H.R. Wilson, and X.Q. Xu. A first-principles predictive model of the pedestal height and width: development, testing and iter optimization with the eped model. *Nuclear Fusion*, 51(10):103016, 2011.

[64] P.B. Snyder, H.R. Wilson, T.H. Osborne, and A.W. Leonard. Characterization of peeling–ballooning stability limits on the pedestal. *Plasma physics and controlled fusion*, 46(5A):A131, 2004.

[65] P.B. Snyder, H.R. Wilson, and X.Q. Xu. Progress in the peeling-ballooning model of edge localized modes: Numerical studies of nonlinear dynamic). *Physics of Plasmas (1994-present)*, 12(5):056115, 2005.

[66] Philip Benjamin Snyder. *Gyrofluid theory and simulation of electromagnetic turbulence and transport in tokamak plasmas*. PhD thesis, Princeton University, 1999.

[67] V.A. Soukhanovskii, J.W. Ahn, R.E. Bell, D.A. Gates, S. Gerhardt, R. Kaita, E. Kolemen, H.W. Kugel, B.P. LeBlanc, R. Maingi, et al. ?snowflake? divertor configuration in nstx. *Journal of Nuclear Materials*, 415(1):S365–S368, 2011.

[68] D.J. Southwood and M.G. Kivelson. Mirror instability, 1, physical mechanism of linear instability. *JOURNAL OF GEOPHYSICAL RESEARCH-ALL SERIES*, 98:9181–9181, 1993.

[69] A. Tarditi, R.H. Cohen, G.G. Craddock, J.A. Crotinger, G.D. Porter, T.D. Rognlien, A.I. Shestakov, and G.R. Smith. Self-consistent core-edge nonlinear transport simulations with corsica 2. *Contributions to Plasma Physics*, 36(2-3):132–135, 1996.

[70] M.V. Umansky, R.H. Bulmer, R.H. Cohen, T.D. Rognlien, and D.D. Ryutov. Analysis of geometric variations in high-power tokamak divertors. *Nuclear Fusion*, 49(7):075005, 2009.

[71] M.V. Umansky, T.D. Rognlien, D.D. Ryutov, and P.B. Snyder. Edge plasma in snowflake divertor. *Contributions to Plasma Physics*, 50(3-5):350–355, 2010.

[72] P.M. Valanju, M. Kotschenreuther, S.M. Mahajan, and J. Canik. Super-x divertors and high power density fusion device. *Physics of Plasmas (1994-present)*, 16(5):056110, 2009.

[73] W. Vijvers, G. Canal, B. Labit, H. Reimerdes, S. Coda, B. Duval, F. Piras, T. Rognlien, D. Ryutov, B. Tal, et al. Reduction of peak wall power loads in l-and h-mode tokamak plasmas in tcv with the snowflake divertor. In *Proc. 24th Int. Conf. on Fusion Energy (San Diego, CA, 2012)*, 2012.

[74] F. Wagner, G. Becker, K. Behringer, D. Campbell, A. Eberhagen, W. Engelhardt, G. Fussmann, O. Gehre, J. Gernhardt, G. Gierke, et al. Regime of improved confinement and high beta in neutral-beam-heated divertor discharges of the asdex tokamak. *Physical Review Letters*, 49(19):1408, 1982.

[75] Weigang Wan, Scott E Parker, Yang Chen, Zheng Yan, Richard J Groebner, and Philip B Snyder. Global gyrokinetic simulation of tokamak edge pedestal instabilities. *Physical review letters*, 109(18):185004, 2012.

[76] W.G. Wan, S.E. Parker, Y. Chen, Z. Yan, R.J. Groebner, and P.B. Snyder. Global gyrokinetic simulation of tokamak edge pedestal instabilities. *Physical review letters*, 109(18):185004, 2012.

[77] E. Wang, X. Xu, J. Candy, R.J. Groebner, P.B. Snyder, Y. Chen, S.E. Parker, W. Wan, G.M. Lu, and J.Q. Dong. Linear gyrokinetic analysis of a diii-d h-mode pedestal near the ideal ballooning threshold. *Nuclear Fusion*, 52(10):103015, 2012.

[78] HQ Wang, GS Xu, HY Guo, BN Wan, Volker Naulin, SY Ding, Ning Yan, W Zhang, L Wang, SC Liu, et al. Observation of a new turbulence-driven limit-cycle state in h-modes with lower hybrid current drive and lithium-wall conditioning in the east superconducting tokamak. *Nuclear Fusion*, 52(12):123011, 2012.

[79] ZH Wang, XQ Xu, TY Xia, and TD Rognlien. 2d simulations of transport dynamics during tokamak fuelling by supersonic molecular beam injection. *Nuclear Fusion*, 54(4):043019, 2014.

[80] D.J. Ward and J.A. Wesson. Impurity influx model of fast tokamak disruptions. *Nuclear fusion*, 32(7):1117, 1992.

[81] T.H. Watanabe, H. Sugama, and S. Ferrando-Margalet. Gyrokinetic simulation of zonal flows and ion temperature gradient turbulence in helical systems. *Nuclear Fusion*, 47(9):1383, 2007.

[82] H.V. Wong, B.Y. Xu, W. Horton, J. Pratt, and J.W. Van Dam. Nonlinear evolution of the firehose instability in a magnetic dipole geotail geometry. *Physics of plasmas*, 12:056502, 2005.

[83] P.W. Xi, X.Q. Xu, X.G. Wang, and T.Y. Xia. Influence of equilibrium shear flow on peeling-ballooning instability and edge localized mode crash. *Physics of Plasmas (1994-present)*, 19(9):092503, 2012.

[84] TY Xia, XQ Xu, and PW Xi. Six-field two-fluid simulations of peeling–ballooning modes using bout++. *Nuclear Fusion*, 53(7):073009, 2013.

[85] H.S. Xie and Y. Xiao. Unconventional ballooning structures for toroidal drift waves. *arXiv preprint arXiv:1503.04440*, 2015.

[86] X.Q. XU. The bout project; validation and benchmark of bout code and experimental diagnostic tools for fusion boundary turbulence. *Plasma Science and Technology*, 3(5):959, 2001.

[87] XQ Xu, B Dudson, PB Snyder, MV Umansky, and H Wilson. Nonlinear simulations of peeling-ballooning modes with anomalous electron viscosity and their role in edge localized mode crashes. *Physical review letters*, 105(17):175005, 2010.

[88] X.Q. Xu, B.D. Dudson, P.B. Snyder, M.V. Umansky, H.R. Wilson, and T Casper. Nonlinear elm simulations based on a nonideal peeling–ballooning model using the bout++ code. *Nuclear Fusion*, 51(10):103040, 2011.

[89] XQ Xu, BD Dudson, PB Snyder, MV Umansky, HR Wilson, and T Casper. Nonlinear elm simulations based on a nonideal peeling–ballooning model using the bout++ code. *Nuclear Fusion*, 51(10):103040, 2011.

[90] XQ Xu, JF Ma, and GQ Li. Impact of the pedestal plasma density on dynamics of edge localized mode crashes and energy loss scaling. *Physics of Plasmas (1994-present)*, 21(12):120704, 2014.

[91] XQ Xu, PW Xi, A Dimits, I Joseph, MV Umansky, TY Xia, B Gui, SS Kim, GY Park, T Rhee, et al. Gyro-fluid and two-fluid theory and simulations of edge-localized-modesa). *Physics of Plasmas (1994-present)*, 20(5):056113, 2013.

[92] Z Yan, GR McKee, RJ Groebner, PB Snyder, TH Osborne, and KH Burrell. High-frequency coherent edge fluctuations in a high-pedestal-pressure quiescent h-mode plasma. *Physical review letters*, 107(5):055004, 2011.

[93] M. Yoshinuma, K. Ida, M. Yokoyama, M. Osakabe, K. Nagaoka, S. Morita, M. Goto, N. Tamura, C. Suzuki, S. Yoshimura, et al. Observation of an impurity hole in the large helical device. *Nuclear Fusion*, 49(6):062002, 2009.

[94] H Zohm. Edge localized modes (elms). *Plasma Physics and Controlled Fusion*, 38(2):105, 1996.

Vita

Jingfei Ma was born in Yuzhou, Henan, P.R.China in 1988, the son of Huaixin Ma and Xuanling Duan. He received the Bachelor of Science degree in applied physics in 2009 from the University of Science and Technology of China (USTC). He then attended the graduate school at The University of Houston and transferred to The University of Texas at Austin in 2010. He completed his Ph. D in plasma physics at the University of Texas at Austin in 2015.

Permanent address: 3607 Greystone Dr, Apt 613
Austin, Texas 78731

This dissertation was typeset with LaTeX[†] by the author.

[†]LaTeX is a document preparation system developed by Leslie Lamport as a special version of Donald Knuth's TeX Program.